MATHEMATICAL MODELING AND CONTROL OF A PIEZOELECTRIC CELLULAR ACTUATOR EXHIBITING QUANTIZATION AND FLEXIBILITY

A Thesis
Presented to
The Academic Faculty

by

Joshua Andrew Schultz

In Partial Fulfillment
of the Requirements for the Degree
Doctor of Philosophy in
Mechanical Engineering

George W. Woodruff School of Mechanical Engineering
Georgia Institute of Technology
December 2012

MATHEMATICAL MODELING AND CONTROL OF A PIEZOELECTRIC CELLULAR ACTUATOR EXHIBITING QUANTIZATION AND FLEXIBILITY

Approved by:

Dr. Jun Ueda, Advisor
George W. Woodruff School of Mechanical Engineering
Georgia Institute of Technology

Dr. Magnus Egerstedt
School of Electrical and Computer Engineering
Georgia Institute of Technology

Dr. William Singhose
George W. Woodruff School of Mechanical Engineering
Georgia Institute of Technology

Dr. Yang Wang
School of Civil and Environmental Engineering
Georgia Institute of Technology

Dr. Nazanin Bassiri-Gharb
George W. Woodruff School of Mechanical Engineering
Georgia Institute of Technology

Date Approved: 20 August 2012

To my daughter, Cora. You're the future, kid. Make the most of it.

ACKNOWLEDGEMENTS

From the most profound depths of my heart I am pleased to thank those who have helped to make this research possible.

I am deeply grateful to the LORD, creator and sustainer of the universe, who allowed me to see into a small part of the beautiful mystery of his creation.

To my advisor, Dr. Jun Ueda, thank you for instilling in me your passion for research and for teaching. I can only hope that I have inherited a portion of your creative energy and enthusiasm. The sheer amount of guidance and support you have provided during these few years would fill volumes. Thank you for all the time and energy you spent teaching me and shaping me professionally. It has been one of the greatest privileges of my life to have been your student.

My sincere thanks to my reading committee, Dr. Nazanin Bassiri-Gharb, Dr. Magnus Egerstedt, Dr. William Singhose, and Dr. Yang Wang. I truly appreciate all the helpful suggestions you have given, both with regard to this research, and for my career in general.

This research could not have come to fruition without the encouragement, suggestions, and tips from many Georgia Tech colleagues. In particular I would like to acknowledge Dr. Aaron Enes, Billy Gallagher, J.D. Huggins, David MacNair, Timothy McPherson, Dimitri Papageorgiou, Brian Post and Ryder Winck. Thank you for being excellent sounding boards and resources for me.

Many thanks to the dedicated Woodruff School staff for all you do. I am indebted to Louis Boulanger, Kyle French, John Graham, and Anh Nguyen for all your contributions to the experimental apparati described in this thesis. Thanks also to Antonette Benford for all her support of our research group's efforts.

I would like to thank the National Science Foundation (Award ECCS-0932208) and the Achievement Rewards for College Scientists Foundation for the financial support of this research.

No word of thanks would be complete without mentioning the various mentors and teachers I have been blessed to have from elementary school through graduate school. Thank you all.

To my parents and grandparents, who taught me the most foundational lessons of life, you deserve deep and enduring gratitude. You have always believed that I could accomplish what I set out to do and went to the greatest of lengths to give me a chance at that success. Thank you for supporting my decision to pursue this path and never failing to say "you can do it."

Finally, a unique debt of gratitude is owed to my beautiful and beloved wife Alicia. There are not words to describe the measure of love and support that you have always given. You supplied confidence when I lacked it, and your belief in me never wavered. This work never would have been completed without you. Thank you for walking every step of this road with me.

TABLE OF CONTENTS

LIST OF TABLES

LIST OF FIGURES

SUMMARY

This thesis presents a mathematical framework and methods for understanding, modeling, and deploying biologically inspired cellular actuators. Cellular actuators are so named because they are modular units that can be connected in series and parallel bundles to actuate a given degree of freedom, much like muscle cells in biological systems. Two important biological principles of these actuators are expounded upon in this work: compliance, and quantization in actuation effort. Methods for modeling and designing nested hierarchical strain amplifying mechanisms are presented. These mechanisms serve the dual purpose of introducing natural compliance and adapting the force-displacement operating characteristic of the active material to one more suitable for robotics applications. This thesis presents a systematic understanding and design method, whereas previous work in this area has resorted to ad hoc methods. Cellular actuator driven systems have a number of on-off inputs, similar to motor units in human muscle. Methods are presented in this thesis that selectively activate motor units in time to produce smooth motion despite an innate tendency toward oscillatory behavior. The effectiveness of the design and control methods presented are demonstrated on a biologically inspired camera positioning mechanism that is driven by a pair of cellular actuators in an antagonistic configuration.

CHAPTER I

INTRODUCTION

The subject of this thesis is to lay the groundwork for a mathematical understanding of biologically inspired actuators that posses quantization and flexibility. Biological systems routinely perform tasks that range from extremely challenging to impossible for even the most advanced robotic systems. For this reason, robotics researchers often look to biology for inspiration in solving problems. The key to biological systems' remarkable performance is their actuation. Two aspects inherent in biological actuators: quantized inputs and flexibility, are crucial to the simple elegance and remarkable capabilities of human muscle tissue. Figure 1 illustrates these elements of bio-inspired actuation as they will be expounded upon in this thesis. This thesis seeks to understand these concepts mathematically and lay a foundation for the systematic design and deployment of actuators of this type in robotic systems.

Although biological motion systems are extremely complicated from the point of view of cognitive and metabolic processes, from a motor system architecture perspective, they are elegant in their simplicity. Muscles consist of bundles of contractile fibers which are activated by a simple neural on-off input. Effects of each individual fiber are summed by the compliant tissue that connects them. This summation of on-off inputs can be viewed as a quantization of the control input. The compliance gives muscle tissue robustness of operation with regard to uncertain environments and off-axis deformations. The on-off nature of the control inputs make the neural circuitry robust to signal disruptions such as capacitive coupling. If some muscle fibers are damaged and become inactive, (which happens routinely), the high redundancy of the system means that the desired task can still be completed.

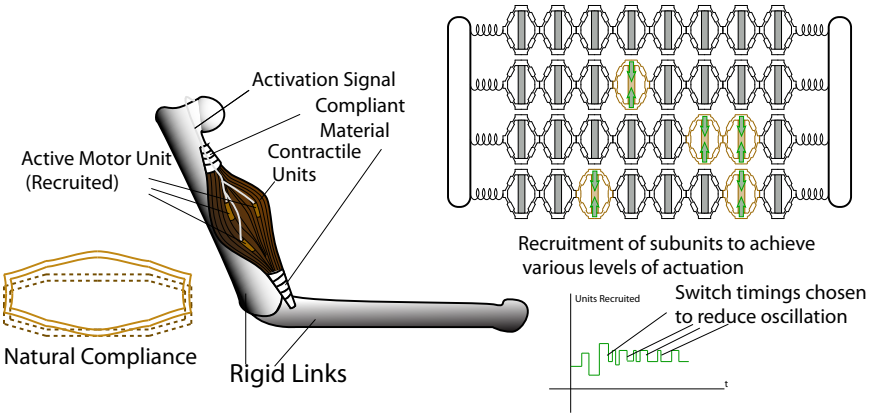

Figure 1: Biological actuation systems are made up of various on-off motor units, or collections of fibers innervated by a single motor neuron. Efforts of various motor units are coupled by elastic cytoskeletal tissue. Activation of motor units are coordinated in time to minimize oscillation and keep the motion smooth.

This biological actuation scheme represents a paradigm shift when applied to the robotics world, where a single analog actuator per degree of freedom is nearly universal. In most robotics contexts, "Redundancy in actuation" is understood to mean more degrees of freedom than are necessary to achieve a specific end effector position and orientation in the task space rather than *multiple actuators per degree of freedom* as in muscle systems. This biologically inspired actuation paradigm holds great promise for expanding the robustness and capability of robotic systems, but is lacking in mathematical tools that can be used to understand the static and dynamic performance of actuators of this type. This thesis seeks to provide a general mathematical framework that can *systematically* ensure that engineering specifications are met and serve as a foundation for further studies of flexible quantized systems.

1.1 Piezoelectric devices

Like human muscle, these actuators will require some sort of basic active unit that contracts in response to an electrical stimulus. Numerous active materials are available that contract under the application of an electric field. These materials are

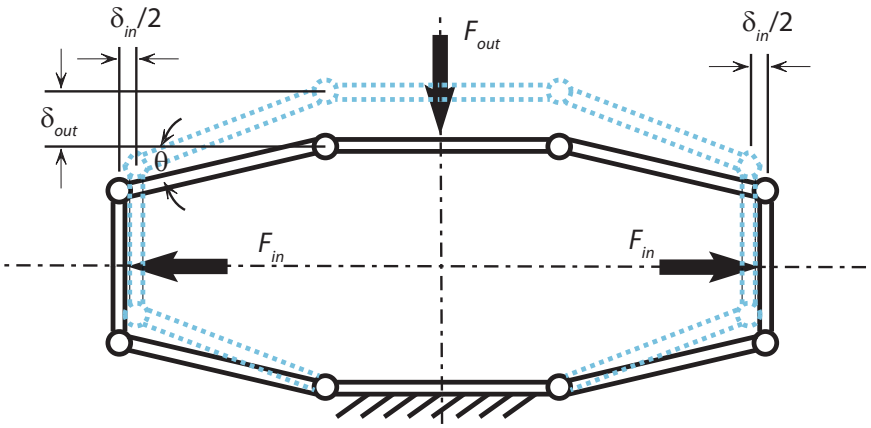

Figure 2: Rhomboidal strain amplification

inorganic, but still exemplify the biological principles mentioned in the previous section. The active material of choice in this thesis is piezoelectric ceramic[1]. It is widely available, does not require extremely large voltages or currents, and is somewhat compliant. Its force-displacement performance point, however, is not suitable for robotics. Several chapters of this thesis are devoted to the discovery of methods to shift the performance point to something more favorable, using rhomboidal strain amplification mechanisms. An added advantage of rhomboidal strain amplification methods is that because they are deformable, no additional parts are required simply to introduce the necessary compliance.

The principle of rhomboidal strain amplification mechanisms is illustrated in Figure 2. Due to the geometry of the rhomboid, when an active material elongates, expanding the major axis by a small amount, the minor axis will contract by a larger amount.

Any robotic mechanism will possess large numbers of these amplifying mechanisms, and often times they will be of small size. For these reasons, it is advantageous to avoid actual hinges and instead machine the mechanism from a single piece of stock. This results in compliant rhomboids, such as those shown in Figure 3. Figure

[1]This thesis uses a commonly available type called Lead Zirconate Titanate (PZT)

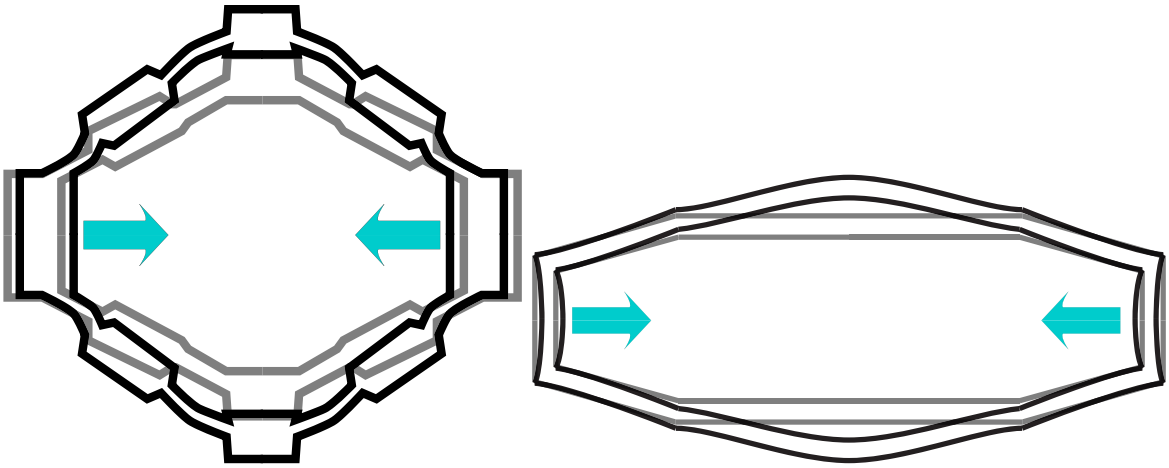

(a) Localized compliance **(b)** DistributedCompliance

Figure 3: Various types of compliant rhomboidal mechanisms. Deformation shown when a force is applied as shown by the arrows

3a shows a rhomboid with "flexure hinges" or zones of localized compliance, however, this is not strictly necessary; an alternative is shown in Figure 3b.

The compliant mechanisms shown in Figure 3 have an amplification property whose description is much more involved than that of the mechanism shown in Figure 2. This is complicated further when the amplification occurs in stages, as illustrated by the examples in Figure 4. This thesis presents a more adequate description.

The engineering goal of this investigation is to find methods of producing amplified piezoelectric actuators that are modular and can be connected together in series and parallel combinations to have muscle-like properties. For this reason, they are well suited to the *cellular actuator* paradigm.

1.2 Discretized actuation effort inspired by muscle fiber recruitment

It is evident from Figure 4 that each device of this type will contain numerous piezoelectric stacks. Piezoelectric material suffers from hysteresis, as shown in Figure 5. To avoid this effect, this thesis will exploit the ability to independently command each of the piezoelectric stack inputs and each stack will considered to be an on-off

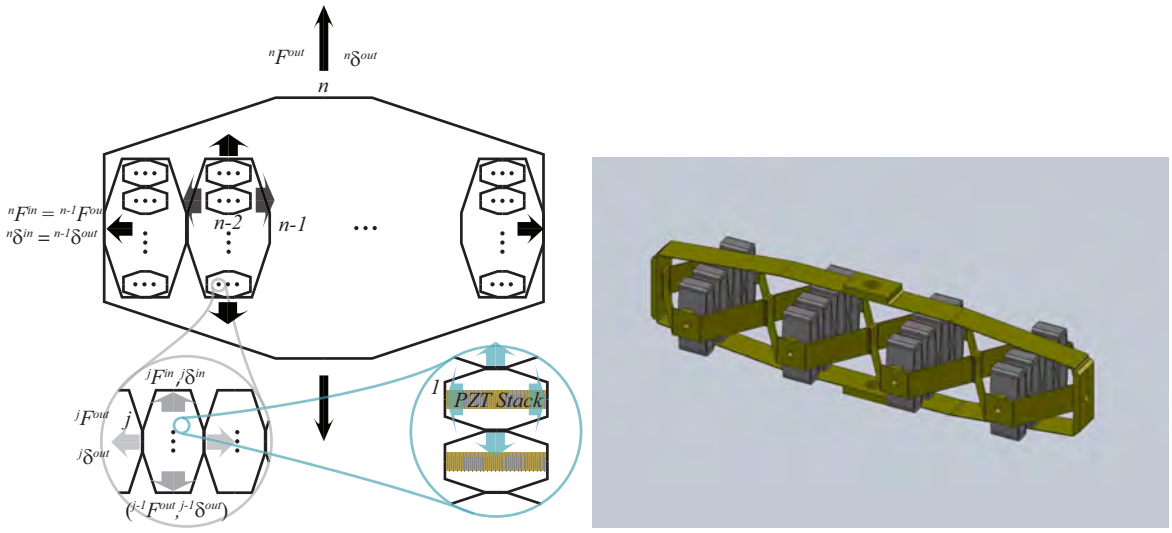

(a) Diagrammatical Illustration **(b)** CAD Model

Figure 4: Multi-stage rhomboidal amplification mechanism. The output of each stage is the input to the next. 4a shows the process diagrammatically and 4b shows a physical device of this type.

input only. In this way, the actuator will only operate at the extreme tips of the hysteresis loop, which are repeatable. This is analogous to the concept of motor units in human muscle tissue.

Muscle systems work using the idea of *recruitment*. Since each motor unit can be only completely on or completely off, the neuromuscular system modifies the number of motor units in the on or off state to increase or decrease actuator effort. This thesis will identify some fundamental recruitment strategies using principles of system dynamics and control theory, and demonstrate them on cellular actuators.

1.3 Experimental apparati

The methods, designs, and algorithms discovered in this work will be demonstrated on two hardware setups, shown in Figure 6, as appropriate to the situation. The first is a replica of the 6-input, two-layer actuator of Ueda, Secord, and Asada [1] in a single-ended configuration. The second is a single-degree-of-freedom camera positioning mechanism driven by an antagonistic pair of three-layer actuators. This

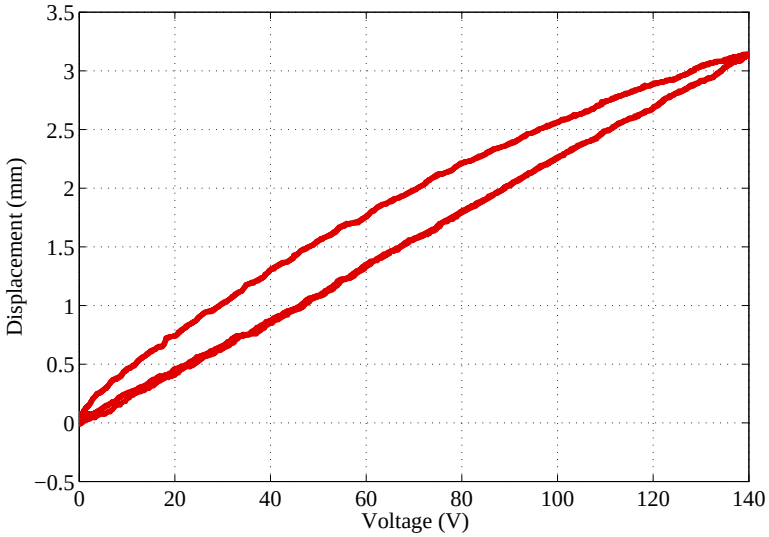

Figure 5: Hysteresis loop in a piezoelectric tweezer device. One path is for charging, the other for discharging. Plot courtesy of Timothy McPherson.

device has 16 inputs per side.

The design of the camera positioning mechanism puts the methods and principles discovered in this research into practice and demonstrates their use. The mechanism itself will also serve as a convenient test bed for future work beyond this thesis, such as validating hypotheses about the neural control of the ocularmotor system and studying co-contraction phenomena.

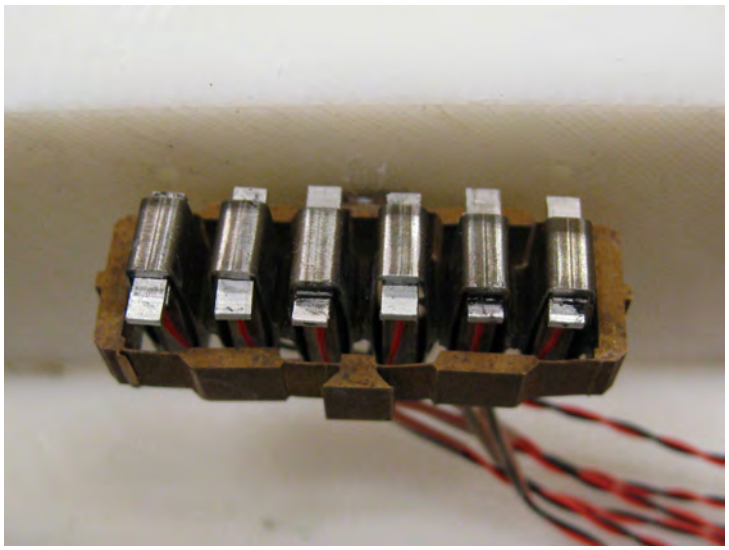

(a) Single-Ended 6 input actuator

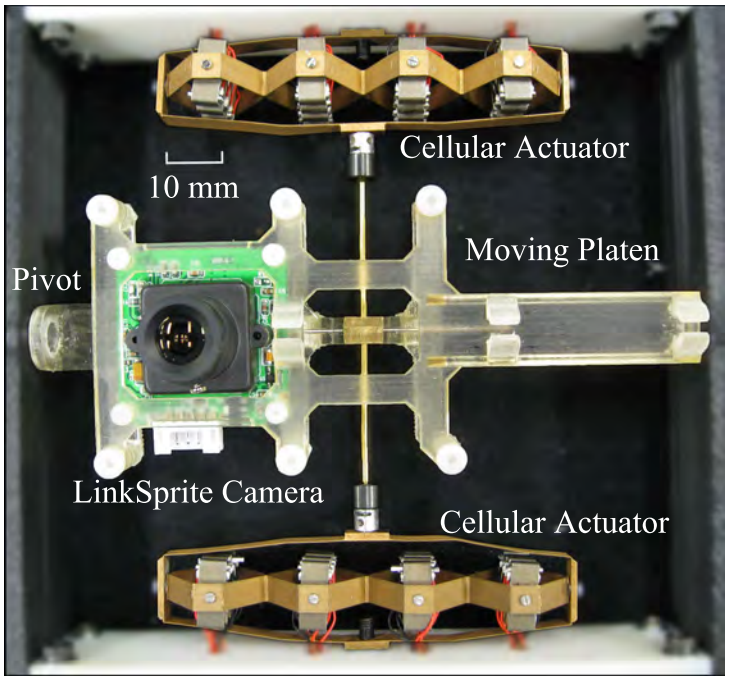

(b) Biologically inspired camera positioner

Figure 6: Devices for experimental validation

CHAPTER II

LITERATURE SURVEY

This chapter summarizes the contributions from various communities that set the context for and provide principles relevant to the work conducted in subsequent chapters. Because cellular actuators use compliant mechanisms to amplify the displacement of piezoelectric actuators, there are representatives from the smart structures literature. A review of non-traditional camera positioning mechanisms is conducted, with some background on the motion of the human eye. In addition, there are particular resources included from the system dynamics and control literature dealing with quantized systems and control of flexible manipulators

2.1 Strain amplified piezoelectric stacks

Lead Zirconate Titanate (PZT) piezoelectric stack actuators, although inorganic, are like biological muscle in that they exhibit a two-way interaction with the load. A piezoelectric ceramic generates a voltage in response to a mechanical stress (the direct piezoelectric effect) or a mechanical strain when an electric field is applied (the converse piezoelectric effect) [2]. Piezoelectric stacks by themselves are of little use in robotics applications due to their minuscule displacement. One method of mitigating this is to use a piezoelectric stack in combination with a stick-slip friction mechanism to move some other part, as in [3]. This technique has been used successfully in a number of mechatronic positioning devices, but "ratcheting mechanisms" of this type are not well suited to advanced robotic applications such as impedance control. A more promising technique is the use of *amplifying mechanisms* to increase the displacement. In this scheme, a piezoelectric stack actuator imposes a force-displacement boundary condition on a strategically chosen point (the input) of a linearly elastic

deformable body. The geometric properties of the deformable body are such that the displacement at another particular point (the output) is much larger than the displacement of the piezoelectric stack. The output point is connected to the load. Of course, some of the electrical energy supplied to piezoelectric stack is stored in the deformable body as strain energy, and in some sense this can be viewed as a parasitic effect.

A summary of various techniques for optimizing these PZT plus compliant mechanism devices can be found in [4]. In general, the design of a compliant mechanism has two distinct steps, a topology synthesis, followed by a dimensional synthesis [5]. One method is the "topological optimization" approach, whereby the designer begins with a "ground structure" [6, 7], usually a uniform truss with uniform members. The algorithm modifies, and in some cases removes these members, resulting in a topology. The thickness of various elements is refined during the dimensional synthesis phase, which does not change the path from active element to load. Grossard, et al. [8] use a variation on this approach using a component library of active and passive ground structures, called FlexIn. Their optimization routine also includes dynamic performance criteria, ensuring that all such modes are collocated. Although this "automatic" approach is appealing, it is computationally intensive, and the process does not apply engineering intuition in the intermediate stages of the process. A degenerate structure may be produced and the designer will not know until late in the process.

Several companies [9,10] produce commercial, modular versions of amplified piezoelectric stacks using a rhomboidal architecture. Most of the research on rhomboidal strain amplification methods focus on the design of regions of localized compliance, or "flexure hinges" and how closely they approximate ideal hinges [11–16]. These works present analytical and numerical evaluations that agree well with finite element analysis. It is also noteworthy that automatic topology synthesis methods searching for

an optimal configuration have converged to rhomboid-like devices [17].

Even with an impressive displacement amplification factor of 10-20, [18, 19], the displacement of these rhomboidal devices is still on the order of μm, still not large enough for most robotics applications. Ueda, Secord, and Asada [1, 20] amplify this displacement still further by placing several amplified stacks in series and amplifying the output of this series combination a second time, calling the strain amplifier of the commercial part the "first layer," and the rhomboidal mechanism that amplifies the output of the series combination the "second layer." This multi-stage amplification technique produces strains on the order of that of human muscle, approximately 22%. Since this actuator has a strain rate similar to that of human muscle, its displacement and force will scale with volume similarly to human muscle. Ueda, Secord, and Asada's actuator is a modular device, and the purpose is to use bundles of these units much like the cells in a muscle. In fact, this work draws connections with the Hill lumped parameter muscle model [21]. For this reason, actuators of this type are termed *cellular actuators*, because many of them can be connected in series and parallel combinations to achieve desired actuation characteristics, as human muscle cells are. Secord and Asada [22, 23] combine this mechanism with mechanical stops so that the resulting actuator will have a position-dependent stiffness as specific units in the chain are activated. While the Hill model is in itself a useful construct, the lumped parameters have no connection to the physical aspects of the design itself. This thesis will address this, forging a connection between the physical manifestation of the actuator and its performance.

A few additional works exist that present some sort of three-dimensional or multi-stage compliant amplification mechanism [24,25], but none of them provide any rationale for their nested design other than to say that a single amplification mechanism produced insufficient displacement. Nor do they provide a general mathematical description that describes the behavior of multi-layer nested structures across a wide

range of geometries and topologies. Structures such as these quickly become difficult to analyze using traditional methods, even when only considering small numbers of layers. As the number of layers becomes large, numerical techniques, such as finite element methods, can become unworkable due to the multiply connected topology and the difficulty meshing the structure arising from interfaces and differences in characteristic dimension between the layers. In addition, roboticists are primarily interested in input-output behavior, not internal forces and nodal displacements, meaning that a lot of computational power is wasted on calculating information that is not used.

2.2 Two-port networks to model two-way interactions

Traditional robotic mechanisms tend to be stiff when viewed from the environment. More advanced robotics behave more like biological systems in that they have a bicausal, or two-way interaction with the environment [26]. Karnopp, Margolis, and Rosenberg [27] treat this interaction using the notions of multiport capacitors and resistors. This thesis borrows a mathematically similar but conceptually different idea, that of the *two-port network* [28, 29].

The two-port network has proved useful in the areas of telemanipulation [30, 31]. Abdalla, et. al. [6] use it to model interactions between piezoelectric stacks, a compliant mechanism, and the load. Ueda, Secord, and Asada [1] use the two-port network model in conjunction with fictitious Hill muscle model lumped parameters. In this thesis, the two-port model is used to provide the necessary abstraction to explain the complex interaction of numerous hierarchically arranged strain amplification mechanisms in a tractable way. Two-port parameters are derived that have a direct connection to the physical structure.

2.3 Automatic camera positioners and the human eye

One motivation for the work conducted in this thesis is that due to their inherent flexibility and cellular structure, these actuators hold the potential to be used in a

camera positioning mechanism that more closely replicates the structure and motion of the human eye. Due to the quantized nature of the actuation, this mechanism may be useful in testing hypotheses about the neurological mechanisms that govern human eye movement. The eye can be reoriented with astounding performance by 6 lightweight recti muscles. They are compliant actuators that are activated in discrete steps by neural impulses. Actuators employed by existing camera positioning mechanisms, surveyed in this section, all bear some key dissimilarities with the human eye.

2.3.1 Automatic camera positioners using traditional actuators

Automatic camera positioning devices are nothing new; in fact, many such devices are commercially available [32]. The vast majority of such devices are motor-on-motor designs, which consist of a "pan" platform that moves relative to a fixed base, and a tilt platform, which is mounted on and moves relative to the pan platform, or vice versa. A third axis, the torsion (or rotation about the gaze axis) mechanism, may be included as well. Examples of motor-on-motor designs include [33] and [34]. There are drawbacks to this design. As a serial mechanism, each actuator has to be capable of driving the inertia and supporting the weight of each successive stage. This is inefficient, as the actuators typically weigh more than the camera itself. Often times the the actuator for the successive stage makes up the majority of the inertia of a given stage. These high inertias reduce the bandwidth of the mechanism. Naturally, the motor-on-motor configuration is not a very energy efficient design, because considerable power is being used to move the actuators, rather than just the camera itself.

Certain notable non-serial camera positioners exist, and they work on a variety of different principles. One option is to design a parallel, rather than serial mechanism, which allows the actuators for all degrees of freedom to be mounted on the base.

The agile eye is a three-degree-of-freedom parallel mechanism (pan, tilt, and torsion) driven by servomotors and linkages arranged symmetrically. Because each motor does not correspond directly to a given degree of freedom, the desired motor displacements must be determined through inverse kinematics, which are complicated expressions. Gosselin et. al. present the design [35, 36], kinematics [37], [38], and discussion of dexterity and singularities [39] of the agile eye. A two-degree-of-freedom platform which uses two linear motors and universal joints is described in [40]. Truong, et. al [41] use a parallel mechanism with cable bevel transmissions. This cable circuit allows both drive motors to be placed on the base.

2.3.2 Automatic camera positioner using non-traditional actuators

Several notable camera positioners exist which use non-traditional actuators. The spherical pointing motor [40], [42] consists of three sets of orthogonal windings and a permanent magnetic rotor mounted on a gimbal, which can be oriented by appropriately energizing the three coils. Chirikjian and Stein propose a spherical stepper motor which uses close packing of various semi-regular circular packings on a ferromagnetic sphere and coils [43]. The coils have a different packing pattern than the sphere, and as a result, the mechanism can reach a large finite set of final positions. The method of determining a proper step sequence to reach a given position is presented. Villgrattner and Ulbrich [44] present a two degree of freedom camera positioner which uses ultrasonic motors.

2.3.3 Human ocular motion

While these mechanisms represent unique and creative solutions to camera positioning, they have very little to do with how the human eye moves. The human eyeball, or globe, is oriented by means of antagonistic pairs of recti and oblique muscles. The range of achievable orientations follows Donders' Law and Listing's law, both for saccadic motion and smooth pursuit [45]. Cannata and Maggiali [46] maintain that

antagonistic pairs of contractile actuators with insertion points into the globe are key to the eye's kinematics.

Cannata and Maggiali's eye is a cable-driven mechanism actuated by traditional servomotors. In actuality, eye muscles consist of a finite number of on-off motor units, or collection of muscle fibers innervated by a particular motor neuron. Cytoskeletal tissue couples the active acto-myosin filaments to the load. Several researchers claim that this property allows muscles to function well in unstructured environments [47], since the elasticity of the muscle tends to return to a stable equilibrium when perturbed. Muscles are controlled by *recruitment*, whereby the nervous system increases or decreases the number of motor units active to increase or decrease the amount of actuation. Each individual motor unit can only be on or off; it cannot be proportionally controlled [48].

The human eyeball, or globe, is supported by soft tissue, and can be considered to have its center fixed with respect to a head-fixed reference frame [49] [50]. The globe undergoes a pure rotation about this center point. The globe's pan and tilt are driven by two pairs of recti muscles, and torsion is driven by the obliques, which are slightly weaker than the recti [49]. For saccadic motion and smooth pursuit (head-fixed eye motions), the eyes obey Donders' law, which states that the eye assumes a single torsional value for each orientation, and Listing's law, which states that all orientations of the eye can be described in an angle-axis representation where the axis vector (gaze direction) lies in the plane orthogonal to the primary gaze (Listing's Plane). The torsion for a given gaze direction is about an axis tilted out of Listing's Plane by half the angle of the gaze direction [45] [50]. The ends of the muscle are inserted into the globe and pass by tissue known as "soft pulleys" [45], [51] before reaching their insertion point in the skull.

Whether Donders' and Listing's law are enforced by mechanical considerations or by neural "programming" is a subject of great debate. Haustein [50] argues that

Donders' law is not mechanically enforced, but rather is determined by the brain. He argues that Listing's law is also "software," based on the fact that innervation rates are linearly related to eye position. This linear relationship has been experimentally verified up to $\pm 25^\circ$ [50]. Cannata and Maggiali [46] argue that there exists a mechanical basis behind Listing's Law. Given certain plausible simplifying geometric assumptions about the insertion points and modeling the soft pulleys as static points, they show that any torque supplied by the four recti muscles produces a Listing-compatible rotation, regardless of the control strategy that determines this torque. They experimentally demonstrate this on a cable-driven eye-ball like mechanism. Tweed and Vilus [52] suggest such a control strategy that, rather than using subtractive feedback, as in a linear system, uses feedback based on quaternion multiplication. Their method accurately predicts Listing-compatible motion, as opposed to previous negative feedback/integrator models.

Although representation of human eye kinematics is beyond the scope of this thesis, the actuator technology presented will allow future researchers to represent the kinematics more closely. Contractile, flexible actuators that incorporate the concept of motor units will allow researchers to apply these physiological mathematical tools directly; there are no "gimbals" forcing them to relate motion planning and control through Euler angles, as in a motor-on-motor mechanism, or through an additional layer of non-biological inverse kinematics, which may introduce additional singularities, as in Gosselin's agile eye.

2.4 Control of flexible systems

In the past two decades, robotic links have become thinner, more compliant and lighter, to the point where the mass of the manipulator is barely larger than that of the object being manipulated. This trend limits the hardware designer's ability to prevent oscillation in the members of robotic devices simply by making large,

inflexible links, and the design teams rely more heavily on the control designer to achieve a suitably damped response in the presence of flexibility.

2.4.1 Flexible manipulators

Approaches to limiting the amplitude of vibration of robotic members have been numerous, most of which augment the rigid body state space with beam deflection states. Various control laws have been proposed, e.g., traditional linear loop shaping, feedforward, and nonlinear control techniques, such as sliding mode control [53], and dynamic feedback linearization involving the first eigenfunction of an Euler-Bernoulli beam [54]. Book [55] enumerates many of the challenges common to control of flexible bodies and summarizes several approaches to modeling and mitigating the flexibility. Nenchev, et. al. [56] determined control laws for manipulators with certain kinds of kinematic redundancies. These control laws are able to suppress vibration of an elastic base by projecting the control effort into the reaction null space, or the null space of the inertia coupling matrix. Liaw and Shirinzadeh [57] present control of a flexure-based micromanipulator mechanism using a neural network.

2.4.2 Command shaping approaches

In certain situations where the most significant natural frequencies of vibration are known, command shaping techniques, which modify the reference command outside of the feedback loop, can insure that the command does not excite any of the known modes of the system. Input shaping [58] is an approach where the reference signal is convolved with a series of impulses, whose spacing is determined by the resonant frequencies of the system. It produces vibration-free point-to-point motion at the expense of slowing the response. Since an input shaper's transfer function is outside the feedback loop, it cannot produce instability. Díaz, Perira, Feliu, and Cela provide a method to concurrently determine a shaper and add mass at strategic locations that minimizes the additional delay incurred by the shaper [59].

Pao [60] extended the input shaping concept to systems with multiple actuators. She showed that by considering all control inputs simultaneously, one can solve for a shaper that has a faster response than shaping each input separately. Lim, Stevens and How [61] take a convex optimization approach to extend the abilities of input shaping for multiple actuators to include additional effects, most notably, reducing transient oscillation.

2.4.3 Switching control methods

The robots used in [60] and [61] both have servomotors which are capable of implementing a continuously variable control input, but there are many systems where on-off actuators are capable of achieving the desired end effector position. In fact, in some cases switching control has certain advantages, such as simplifying the control interface and creating less waste heat, even when the actuators are capable of continuously variable actuation. In [62], the authors develop a direct switching controller for a servomotor current control loop that compares favorably with PWM and linear methods. This method can be extended to the full control loop, resulting in a form equivalent to sliding mode control. Barth and Goldfarb [63] develop a switching control law for pneumatic actuators that is also based on sliding mode control. Singhose, Seering, and Singer [64] showed that using a vector diagram approach with an on-off actuator can provide a vibration-free command in the same manner as input shaping. Sorensen, Hekman, and Singhose [65] take some steps toward applying input shaping to systems with multiple discrete levels by looking at the results of approximating an input shaped command by the admissible values.

Several works [66], [67] and [68] extend this method to account for and minimize fuel usage, which is particularly important for flexible spacecraft. Song, Buck and Agrawal [69] combine input shaping with pulse width modulation, rather than using a vector diagram approach.

2.4.4 Flexibility in biological systems

In contrast with traditional servomotors, biological actuators are by nature compliant [21], and this renders biological systems capable of a number of fine motor motions that are challenging for traditional actuators. Robots be equipped with such flexible actuators could achieve motions of a more biological nature, and this would enhance robotic capability, energy efficiency, and safety [70]. This compliance is manifest even when the actuator is de-energized.

It is well known that biological muscles possess a number of resonant modes, and that they are quantized in their actuation ability due to the finite number of axons present in a given muscle group. When muscles are subjected to a vibratory stimulus, they are able to provide active damping [71]. The neuromuscular mechanism by which this occurs is not well understood, but it demonstrates that it is possible to remove vibration from oscillatory modes even if the actuation is quantized.

2.4.5 Piezoelectric vibration suppression techniques

Use of PZT materials in active control of structural vibrations has been well studied. In particular, Onoda, et. al. [72] used PZT actuators to create a variable stiffness spring whose stiffness varies based on the location of the state in the phase plane, driving the state to the origin. The PZT actuators do not actuate the flexible member, but are rather used to couple and decouple additional structural elements to change the stiffness at the appropriate time. Corr and Clark [73] extended this method by applying a PZT stack to the structure with an resistor–inductor shunt instead of a mechanical spring element. Although these approaches are of interest in robotics, they would mainly be considered as additional measures to be added to the robot once all options in the control architecture and joint actuation strategies had been exhausted, since implementation of such a strategy would incur additional cost and complexity.

2.4.6 Feedback and sampled control for vibration suppression

Command shaping methods only suppress oscillation induced by the actuator itself; it cannot reduce oscillation due to disturbances in the environment. Similar methods, such as input shaping [58], likewise only add transfer zeros at specified frequencies; they cannot add damping to lightly damped flexible poles and remove existing oscillation.

There is a rich body of literature on control techniques for suppressing vibration in flexible automatic devices. Most of these take a sampled–data system with a zero–order–hold as a given and few look at what can be done during the sample period itself to suppress oscillation. Fujimoto and Hori [74], however, recognized that the sampling rate is often times limited by the measurement rate of sensors and A/D conversion, and often times the control signal can be changed more quickly. By predicting the evolution of the state during the sample period at several intersample points, they were able to design a controller that would suppress oscillation at frequencies approaching the Nyquist frequency for a flexible disk drive head.

2.5 Control of Quantized Systems

All digital control systems have quantization effects due to finite word length and digital to analog conversion. Most of the time, these effects are minor, and quantization errors are typically treated as a white noise input disturbance. Delchamps [75] performed a rigorous mathematical analysis of quantization and showed that by viewing quantization of state feedback as a limited amount of information about the state that knowledge of the state can be improved with successive quantized measurements. He showed that a control law based on quantized state feedback measurements can drive the state to within a prescribed distance of the origin for a finite amount of time, provided the system is reachable. This is generally referred to as "practical stability," because the state cannot be shown to be within an arbitrarily small distance of the

origin for all time. It has been shown that a logarithmic quantizer is stable [76,77]. Fu and Xie [78] looked at quantization as an H_∞ problem and looked at more arbitrary quantizations.

The cellular actuator proposed by Ueda, Secord, and Asada [1] has equal inputs, and therefore can be represented as a uniform quantizer on the input. Richter, et. al. [79–81] treat the stability of a uniform quantizer on the input and the state using the sector bound method. Brockett and Liberzon [82] proposed a hybrid control scheme that changes the sensitivity of quantization of the state feedback based on the value of the state and showed that such a scheme is Lyapunov stable.

Azuma and Sugie [83, 84] study optimality of quantized systems. In their work, the quantization error is filtered and added to the input. Each of these methods described in this section are interesting from a controller design point of view, but they are mainly oriented toward information transmission. They do not consider the case where the quantization is an artifact of the actuator itself. For example, since the cellular actuator's quantization cannot be changed on the fly, the methods of Brockett and Liberzon cannot be implemented to stabilize the system. So while the methods in these works are not directly applicable to the problems confronted in this thesis, they provide an interesting context and some general principles have influenced the development of the work.

2.6 Summary

Biological systems are characterized by a compliant interaction with the load, a two-way relationship with the environment, and quantization in the control input to a muscle. The area of biologically inspired actuators has recently produced a number of unique devices and good constitutive models of the active materials, but there is a void in terms of the number of analytical tools and systematic descriptions to describe their behavior in a general way. This thesis aims to create some analytical

and mathematical tools to aid in the understanding and use of these types of systems.

Several key principles are combined from disparate areas in the literature and put into the context of biologically inspired systems. The following are those that most shape lines of reasoning in this thesis. The performance characteristic of piezoelectric ceramic (or other active materials) can be modified by using an appropriately chosen compliant mechanism. This mechanism has the added effect of introducing compliance and better replicating the two-way relationship characteristic of biological systems. It is possible in both biological systems and in robotic systems to suppress oscillation and generate smooth trajectories in spite of quantization, using carefully timed switching inputs.

This chapter discussed a range of topics related to the modeling, performance specification, and control of biologically inspired actuators. It draws from various communities relevant to the work. The next chapter begins the study of nested strain amplifying mechanisms, and presents an analytical model that reduces complicated geometries to a simple set of parameters.

CHAPTER III

TWO-PORT NETWORK MODELS FOR COMPLIANT RHOMBOIDAL STRAIN AMPLIFIERS

This chapter describes the relationship between the geometry of a rhomboidal strain amplifying mechanism and its input-output performance. With appropriate mechanical-electrical analogies, a strain amplifying mechanism can be described as a *two-port network* circuit model. Two-port networks are typically used to describe input/output behavior of complicated or unknown electrical networks. This abstraction will prove useful in subsequent chapters when various strain amplifiers are interconnected.

For the purposes of this thesis, a *rhomboid* can be considered to be any doubly symmetric convex polygon composed of initially straight segments of elastic material. The mathematical formulation for this generalized rhomboid will be presented, which applies to mechanisms with both distributed and localized compliance. The two-port network model is described in terms of a 2×2 matrix which has units of stiffness.

The method of determining a two-port model for a rhomboid is demonstrated for particular set of geometric parameters. The fidelity of model is evaluated by comparing results with those returned by finite element methods for various sets of these parameters. Finally, the two-port model is determined empirically for a particular sample mechanism and the results compared to the analytical model.

3.1 Two-port models of strain amplifying compliant mechanisms

According to Choma, [28], the two-port network is a simple way to model an electrical network when the mathematical models of the underlying components are either unknown, or are inordinately cumbersome. The two-port concept allows the designer

to analyze the network as a "black box" and focus on its input-output behavior, and ignore the constitutive relationships interior to the network. Input-output behavior can be described by simple passive impedances plus voltage-controlled current sources or current-controlled voltage sources interior to the network. Interested readers can find additional details in Appendix A.

With the appropriate mechanical-electrical analogies, two-port networks can also be used to model rigid body or flextensional mechanical systems. This makes two-port networks a simple but powerful analysis tool, one that is particularly useful for describing the two-way interactions characteristic of biologically inspired actuation. Abdalla [6] et al. model not only the compliant mechanism as a two port network, but also the piezoelectric stack actuator itself. The four quantities of interest in the model are the voltage applied to the stack, the charge stored in the stack, the force applied by the stack, and the stack displacement. Because of the relationship between these quantities, the electromechanical transduction of the PZT ceramic also lends itself to a two-port network description. It is even more advantageous to model the compliant mechanism as a two-port network, for then the interconnection laws for two-port networks can simply and elegantly describe an entire multi-stage compliant device, and if the source impedance (electrical) and terminal impedance (mechanical) are known, the entire response can be predicted. This will be explored in Chapters 4 and 5. Abdalla, et al. show some key properties of the two-port model approach, but do not explain how to determine the immittance matrix from the geometry and material properties of the compliant mechanism constituting each layer, necessitating the contribution described in this chapter. Abdalla's method optimizes the compliant mechanism for a particular load, whereas in robotic devices the load can vary widely.

The approach in [6] assumes that the designer begins the design with knowledge of the load impedance. The authors show that the compliant mechanism and the PZT stack can be designed separately, in that order. They also derive an expression

for the efficiency and show that it varies inversely with the geometric advantage (or displacement amplification factor) of the mechanism,

$$a = \frac{\delta_{out}}{\delta_{in}}. \tag{1}$$

They then begin with an assumed truss ground structure and numerically follow a topological optimization approach. The most efficient structure is the ground structure, which is the most rigid, and is therefore not useful. Using a quadratic cost function with weights on the geometric advantage and efficiency, they arrive at an optimal compliant mechanism for the assumed load. While Abdalla's work highlights the benefits of two-port modeling for compliant mechanisms, it is not clear how well the mechanism will work across varying loads typical in robotics and how the model will vary with manufacturing tolerances, because it does not draw the connection between geometry and mechanism function in general.

Rhomboidal mechanisms are an intuitive topology and lend themselves well to interconnections in series, parallel, and nested configurations and can thus be used to construct muscle-like robotic actuators. Another good rationale for using rhomboidal mechanisms is that automatically generated topology optimizations have converged to structures that are rhomboidal in shape [17]. Trying to achieve a desired stroke length with series combinations of piezoelectric stacks amplified a single time (such as the commercially available Cédrat APA50XS) results in an overall actuator that is too long relative to its stroke length.

3.2 Nested amplification mechanisms

Most of the discussion of nested mechanisms is deferred to Chapter 4, but a short description is given here to motivate the discussion in this chapter. A nested actuator begins with single-layer amplified PZT stacks, concatenates a small number of these in series, and amplifies their displacement a multiple times using compliant

rhomboidal mechanisms. Each layer of amplification can be expressed as a two-port network. Ueda, Secord, and Asada [1] propose such a multi-layer strain amplified mechanism, and briefly mention its connection to the two-port network formalism. Rather than supplying connections to the mechanism's geometry, their immittance matrix parameters are related to the stiffnesses in a lumped parameter Hill muscle model, whose parameters are fictitious; Hill parameters have no connection to the physical geometry and material constants. Using finite element methods, they develop a prototype two-layer actuator optimized for maximum output displacement given reasonable manufacturing constraints. However, this actuator has very low force capability and the design procedure was performed using ad hoc methods. It is not clear from this work how force-displacement specifications are satisfied by a set of immittance parameters and how to determine the geometrical characteristics of the various layers that meet these performance specifications.

In essence, Ueda, Secord, and Asada [1] solve the "forward" problem: given a geometry, determine its performance characteristics. To produce actuators useful in robotics, one must solve the "reverse" problem: given a set of performance specifications, determine the geometry characteristics that will meet these specifications, i.e., determine what compliant mechanisms allow a robot to supply required forces within the desired range of poses when a voltage is applied to a PZT stack. *It is the reverse problem that really benefits from an analytical model.* The two-port model of rhomboidal strain amplifying mechanisms presented in this article is a key step towards making the reverse problem easier to solve, because it encapsulates complicated geometric relationships in 3 elements per layer that are key to its input-output behavior. Optimization routines generally must solve the forward problem multiple times in order to find an optimal point. To analyze complicated series-nested compliant actuators with multiple stages of amplification using finite element methods, great care needs to be taken with the mesh at interfaces, thin sections, and changes

in cross section to ensure that the problem will be numerically solvable. Even if a search direction can be computed using finite differences, to perform a finite element simulation, a new CAD model needs to be constructed. In addition, the finite element results give no insight on how to choose the trial geometry to get closer to the goal. This makes solving the reverse problem using finite element models extremely labor intensive. The two-port approach allows the designer to find an analytical model for a given choice of geometric parameterizations, and quickly get a sense of how changing each parameter affects the performance of the compliant strain amplifier and the nested mechanism as a whole. Since this makes the forward problem a function evaluation, common optimization routines can be used, provided the parameterization and constraints result in a convex problem. Search directions can be automatically computed form the analytical model, and the only CAD model that need be created is the one used for manufacture. Using the two-port formalism, it is easy to see how manufacturing tolerances will affect the performance of the entire device. The two-port model also shows clearly how each layer in a nested hierarchy contributes to the function as a whole.

3.3 Finding expressions for the immittance parameters using Castigliano's theorem

Since the rhomboidal strain amplification mechanism will be modeled as two-port network, this work is less concerned with the internal stress and strain fields than the input-output behavior of the mechanism. For this reason, it is natural to use Castigliano's theorem [85], since it provides an input-output relationship between the loads on a structure and a displacement at a given point.

Castigliano's theorem has been used in several previous works to determine the stiffness of flexure hinges [12, 16]. Lobontiu and Garcia [13] characterize an entire hinged mechanism in terms of three parameters, the input stiffness, the output stiffness, and the displacement amplification and optimize the filleted flexure hinges to

achieve a balance between amplification and stiffness, however, unlike a two-port model, it does not describe the function of the mechanism across varying loads and control inputs and was not formulated with large-stroke robotic applications in mind. In an actual compliant displacement amplification mechanism, the amplification factor will vary with loading conditions and along the stroke necessitating a slightly more involved description. The bilateral two-port approach adds a level of abstraction that makes the problem tractable with larger numbers of parameters and is naturally suited to representing the two-way interactions of nested multi-stage compliant mechanisms.

This analysis begins along the lines of the "chain method" described by Howell [86] for a simply connected body. Unlike Howell, this work is not interested in a numerical evaluation of nodal displacements. Instead, the boundary conditions for a multiply connected body are resolved analytically, resulting in an analytical input-output model. In order to determine the two-port model of a general rhomboidal compliant mechanism, this analysis makes several simplifying, but justified, assumptions. First, it assumes that the mechanism is symmetric about about two orthogonal axes, aligned with the input and output directions. This allows derivation of the input-output relationships by analyzing a quarter mechanism. Second, it assumes that forces are applied to a given layer only at the input and the output. Third, it assumes that the compliant mechanism is composed of finitely many thin straight segments rigidly connected in series and fillet radii are small relative to the segment length and have negligible effect.

The method to determine the expressions for the immittances is summarized as follows: first, it resolves the static indeterminacy in the doubly connected rhomboid, eliminating the moment reaction in favor of the input and output forces. The internal moment reaction is a hidden parameter and is subsumed in the two-port formalism. This is possible because of the symmetry of the compliant mechanism. Second, Castiglianos theorem is applied in both the input and output directions. The third step

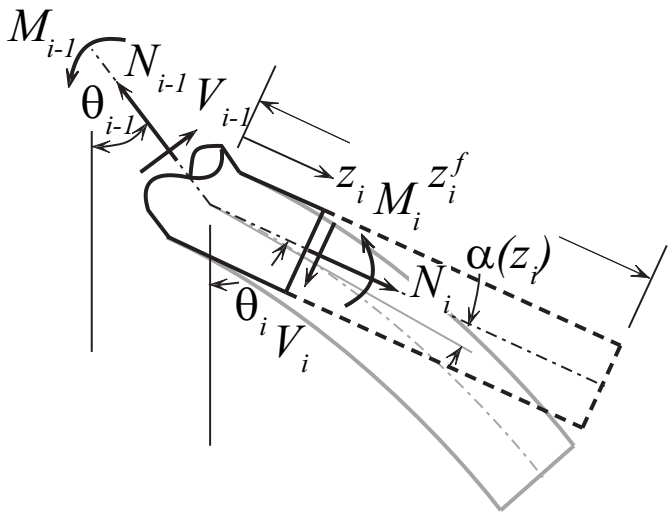

Figure 7: Free body diagram of a general flexible segment with no loads applied to its interior.

collects terms so that the two relations found in the second step correspond to the two-port model relationships.

Consider a general single straight segment (i) rigidly connected to the preceding segment ($i-1$). The free body diagram of this segment is shown in Figure 7. In this way, the internal forces in a given segment can be expressed in terms of its geometric parameters and the forces in the preceding segment. N_i is the internal axial load, V_i is the internal shear force, and M_i is the internal moment for segment i. z_i is the distance to a point on the segment, ranging from 0 to z_i^f. $\alpha(z)$ is the angular deflection at z_i. θ_i is the orientation of the segment in the undeformed configuration. Beginning with the reactions at the fixed flange (section 0), one can propagate the internal forces and moment outward from segment to segment through the quarter mechanism until the point of application of the input force is reached.

Applying the equations of static equilibrium to section i, in matrix-vector form, the internal forces and moments in segment i at a distance along the segment z_i can be expressed in terms of those in the preceding segment as:

$$\begin{bmatrix} N_i \\ V_i \\ M_i \end{bmatrix} = {}^{i}P_{i-1} \begin{bmatrix} N_{i-1} \\ V_{i-1} \\ M_{i-1} \end{bmatrix} \tag{2}$$

where

$${}^{i}P_{i-1} = \begin{bmatrix} \cos(\theta_i - \theta_{i-1}) & -\sin(\theta_i - \theta_{i-1}) & 0 \\ \sin(\theta_i - \theta_{i-1}) & \cos(\theta_i - \theta_{i-1}) & 0 \\ z_i \sin(\theta_i - \theta_{i-1}) & z_i \cos(\theta_i - \theta_{i-1}) & 1 \end{bmatrix}. \tag{3}$$

To propagate this to the next segment, evaluate (2) at $z_i = z_i^f$, which is a geometric parameter. The rhomboidal amplification layer is a doubly connected, statically indeterminate structure. In order to solve a doubly connected structure, one needs additional compatibility conditions expressed in terms of the displacement, which are developed here. A generalized compliant mechanism that conforms to the assumptions above is shown in Figure 8. $N_k, M_k, k = \{P, Q, R\}$ are the equivalent moment and axial reactions from the removed section. The circled numbers $\{1 \cdots N\}$ denote the index of each segment. R_x, R_y, and M_R are the reactions at the fixed end condition. To resolve the static indeterminacy, proceed as follows: imagine that the structure is cut in half along A–A, discarding the right hand (light gray) half. A fixed end condition is then applied at point R. Due to symmetry about A–A, each half of the structure will carry half of the applied load F_{out}, and deform by the same amount in the direction of F_{out}. Therefore, the right half will impose no shear reaction on the left half. However, there will be a normal reaction force, N_P, imposed by the right half on the left half to insure that point P remains on the center line. The right half will also apply a moment reaction M_P on the left half, ensuring that the deflection angle of the final segment is continuous at P. These two compatibility conditions allow the determination of these unknown internal reactions.

Because the structure is also symmetric about B–B, the upper and lower quarters

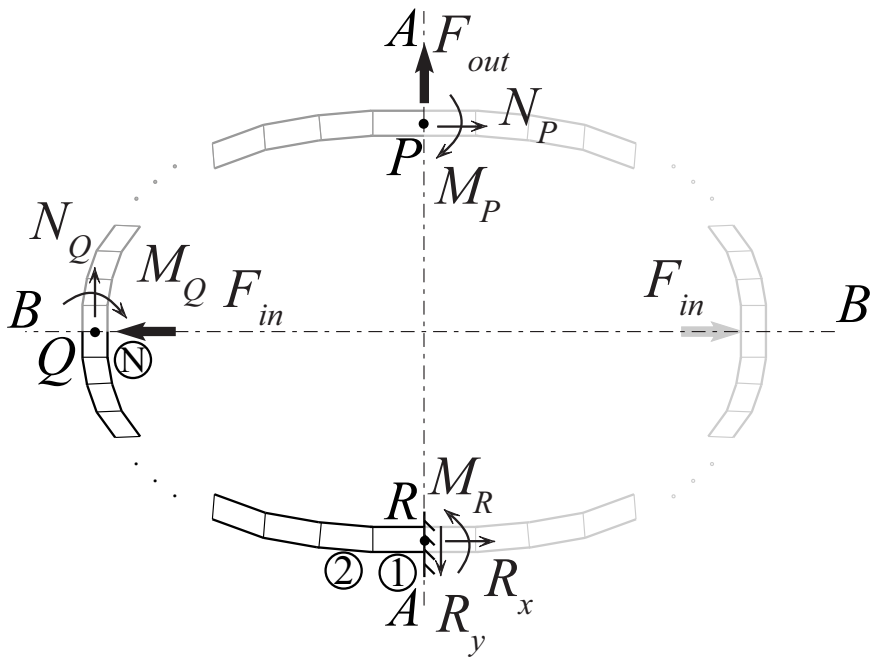

Figure 8: Doubly symmetric actuator composed of straight segments. Because of the symmetry, the entire behavior can be determined by analyzing the black structure only.

will each carry 1/2 of the load F_{in}, and deform in this direction by the same amount. This allows the compatibility conditions to be expressed at point Q, simplifying the results, discarding the upper, dark gray quarter, replacing it by its internal reactions N_Q and M_Q. Because of symmetry about B–B, the internal reaction $N_Q = F_{out}/2$. Due to symmetry, the compatibility condition on the deflection angle stipulates that the tangent at Q must remain unchanged from its undeformed configuration, or:

$$\alpha(z_i^f) = \theta_N. \tag{4}$$

where α is the function for the deflection angle of segment i. In [13,85], expressions for redundant reactions are found using Castigliano's theorem, but in this case, since only one integration is required, it is simpler to proceed by direct integration of the moment and then solve for M_Q. Assuming each segment is linearly elastic, has negligible shear deformation and undergoes small deflections, applying the well-known slope-moment

relationship [85] gives:

$$\alpha(z_i) = \frac{dv}{dz_i} = \frac{1}{EI_i} \int M_i(z_i)\ dz_i, \tag{5}$$

where E is the Young's modulus of the material, and I_i is the moment of inertia of the segment, and v is the deflection. Integrating, augmenting (2), and evaluating at z_i^f, the internal forces and deflection angles of each segment can be propagated forward according to:

$$\left[\begin{array}{c} N_i \\ V_i \\ M_i \\ \hline \alpha_i(z_i^f) \end{array}\right] = {}^{i}P_{i-1}^{aug} \left[\begin{array}{c} N_{i-1} \\ V_{i-1} \\ M_{i-1} \\ \hline \alpha_i(z_{i-1}^f) \end{array}\right]. \tag{6}$$

$${}^{i}P_{i-1}^{aug} = \left[\begin{array}{ccc|c} \cos(\theta_i - \theta_{i-1}) & -\sin(\theta_i - \theta_{i-1}) & 0 & 0 \\ \sin(\theta_i - \theta_{i-1}) & \cos(\theta_i - \theta_{i-1}) & 0 & 0 \\ z_i^f \sin(\theta_i - \theta_{i-1}) & z_i^f \cos(\theta_i - \theta_{i-1}) & 1 & 0 \\ \hline \frac{z_i^{f\ 2}}{2EI} \sin(\theta_i - \theta_{i-1}) & \frac{z_i^{f\ 2}}{2EI} \cos(\theta_i - \theta_{i-1}) & \frac{z_i^f}{EI} & 1 \end{array}\right] \tag{7}$$

The compatibility conditions state that:

$$\left[\begin{array}{c} N_N \\ V_N \\ M_N \\ \hline \alpha_N(z_N^f) \end{array}\right] = \left[\begin{array}{c} N_Q \\ V_Q \\ M_Q \\ \hline 0 \end{array}\right]. \tag{8}$$

The first three equations are trivial, but the final equation can be solved to find the expression for the unknown internal moment M_Q in terms of F_{in} and F_{out}. Once this expression is determined, it can be substituted it into the expression for M_R and propagated outward using (2). Now that the static indeterminacy has been resolved, the expressions for the input displacement (displacement at Q along the direction of

F_{in}), and the output displacement (displacement at R along the direction of F_{out}) can be found using Castigliano's theorem.

Because the integration limits in this application of Castigliano's theorem are finite constants, and for a linearly elastic structure, the strain energy/per unit length will be continuous, the derivative can be brought inside the integral. Castigliano's theorem can then be expressed as:

$$\delta_j = \sum_{i=1}^{N} \int_0^{z_i^f} \left(\frac{M_i}{EI_i} \frac{\partial M_i}{\partial F_j} + \frac{2(\nu+1)V_i}{EA_i} \frac{\partial V_i}{\partial F_j} + \frac{N_i}{EA_i} \frac{\partial N_i}{\partial F_j} \right) \, dz_i, \tag{9}$$

where ν is the Poisson's ratio of the material, and A_i is the cross-sectional area of the segment. Since each of the internal forces and moment is linear in the loads F_j, one can use (2) to propagate the partial derivatives forward segment by segment, with the internal forces and moment replaced by their partial derivatives. Assuming each summand is calculated iteratively, [N_{i-1} V_{i-1} M_{i-1}] and their partial derivatives will not depend on z_i, and thus are pulled out of the integral. The output displacement can then be expressed as:

$$\delta_j = \sum_{i=1}^{N} \begin{bmatrix} N_{i-1} \\ V_{i-1} \\ M_{i-1} \end{bmatrix}^T Q_i \begin{bmatrix} \frac{\partial N_{i-1}}{\partial F_j} \\ \frac{\partial V_{i-1}}{\partial F_j} \\ \frac{\partial M_{i-1}}{\partial F_j} \end{bmatrix}, \tag{10}$$

where

$$Q_i = \int_0^{z_i^f} {}^iP_{i-1}^T \begin{bmatrix} \frac{1}{EA_i} & 0 & 0 \\ 0 & \frac{2(\nu+1)}{EA_i} & 0 \\ 0 & 0 & \frac{1}{EI_i} \end{bmatrix} {}^iP_{i-1} \, dz_i. \tag{11}$$

Performing the integration with respect to z_i, and assuming each segment has a rectangular cross section of width t_i, results in:

$$
\begin{aligned}
Q_i &= \frac{1}{24EI_i}\begin{bmatrix} q_{11} & q_{12} & q_{13} \\ q_{21} & q_{22} & q_{23} \\ q_{31} & q_{32} & q_{33} \end{bmatrix} \\
q_{11} &= 2(z_i^f t_i^2 \cos^2(\theta_{i+1}-\theta_i) \\
&+ ((2\nu+1)z_i^f t_i^2 + 4{z_i^f}^3)\sin^2(\theta_{i+1}-\theta_i)) \\
q_{12}=q_{21} &= ((2\nu+1)z_i^f t_i^2 + 4{z_i^f}^3)\sin(2(\theta_{i+1}-\theta_i)) \\
q_{13}=q_{31} &= 12{z_i^f}^2\sin(\theta_{i+1}-\theta_i) \\
q_{22} &= 2(z_i^f t_i^2 \sin^2(\theta_{i+1}-\theta_i) \\
&+ ((2\nu+1)z_i^f t_i^2 + 4{z_i^f}^3)\cos^2(\theta_{i+1}-\theta_i)) \\
q_{23}=q_{32} &= 12{z_i^f}^2\cos(\theta_{i+1}-\theta_i) \\
q_{33} &= 24z_i^f
\end{aligned} \tag{12}
$$

Applying (10), requires a change of variable: $F = F_{in}/2$. This is necessary because the quarter actuator carries the 1/2 the input force, and taking the partial derivative with respect to the full input force F_{in} will yield an erroneous result. To find the input displacement δ_{in}, apply (10) with $F_j = F$. This quantity will be multiplied by 2, since each half of the actuator undergoes this displacement. Applying (10) with $F_j = N_Q$ yields the displacement of point Q. Because of symmetry about B–B, The displacement at point Q can simply be multiplied by 2 to get the displacement of point P, or δ_{out}.

Because each segment is a linearly elastic, Euler-Bernoulli beam with point loads, one would anticipate that the displacement expression will be linear in the loads multiplied by a multivariate cubic polynomial in d, h, and w. This is indeed the case. However, the application of the symmetric compatibility conditions along section A–A and B–B in Figure 8 make the expression more complicated. This analysis solved (6) for the unknown moment reaction M_Q, and this shows up in the denominator of

the expression. Because the denominator of the displacement expression arises from the coefficient of the M_Q term in (6), the denominator will be first order in d, h, and w. However, looking at the *relative order* of the displacement expression (order of the numerator - order of the denominator), it is 3, the same order as a simple beam. If the structure is not rectangular, there are also trigonometric factors as part of these expressions. For this reason, it is advisable to keep the number of geometric parameters to a minimum, since the complexity of the expression will scale with the number of geometric parameters.

Collecting terms in the expressions for δ_{in} and δ_{out} with respect to the loads F_{in} and F_{out}, the denominator D_M will be common, up to a multiplicative constant. Therefore, these equations can be written as:

$$\begin{bmatrix} \delta_{in} \\ \delta_{out} \end{bmatrix} = \frac{1}{D_M} \begin{bmatrix} C_{11} & C_{12} \\ C_{21} & C_{22} \end{bmatrix} \begin{bmatrix} F_{in} \\ F_{out} \end{bmatrix}, \tag{13}$$

where C_{ij} are quartic factors of the geometric parameters. The compliance matrix in this equation is precisely an immittance matrix of a two-port network. (Choosing displacement to be analogous to voltage makes it an admittance matrix). Its inverse is precisely the stiffness (impedance) matrix introduced in [1]. According to Maxwell's reciprocity theorem [6], at DC, the compliant mechanism will be a reciprocal two-port network. Therefore, following the notation in [1] the stiffness form is written as:

$$\begin{bmatrix} F_{in} \\ F_{out} \end{bmatrix} = \begin{bmatrix} s_1 & s_3 \\ s_3 & s_2 \end{bmatrix} \begin{bmatrix} \delta_{in} \\ \delta_{out} \end{bmatrix}, \tag{14}$$

where s_1 corresponds to the stiffness in the input direction when the output is blocked, s_2 corresponds to the stiffness in the output direction when the previous amplification layer is completely rigid, and s_3 describes the cross-coupling from input to output, e.g. how much force is generated at a fixed output due to a given input displacement. s_3 also has units of stiffness. This matrix is positive definite; The combined effect

of the stiffnesses in the input and output load's own direction will always be greater than the cross-coupling effect, due to the storage of strain energy in the compliance of the mechanism.

3.4 Model validation by finite element methods

The procedure in the previous section produces an analytical two-port model for a wide class of geometries. In order to implement this method, the designer must choose a useful set of geometric parameters that will be varied. The immittance matrix will be a function of these parameters. To demonstrate how this procedure works, this section considers an octagonal mechanism ($N = 3$) of constant thickness ($t_i = t \quad \forall\ i$), varies its parameters and compares the analytical model's predictions to Finite Element Methods (FEM). The associated geometric parameters and the expected deformed shape with tensile input and output loads are shown in Figure 9. Since the purpose of the FEM evaluation is merely to quantify how well the linear model performs compared to a numerical approach, $w/2 = 1$ m and $b = 2$ mm were chosen as general characteristic dimensions. This "meterstick" size gives an intuitive feel for how much deformation should occur, providing a useful check. As long as the size permits the device to be analyzed as a continuum, the mesh size will scale with the geometry of a given part, and the level of accuracy should be the same. In the actual application, w will be set by the previous layer and b is the thickness of the plate from which the compliant mechanism is machined, so these quantities are considered fixed. The FEM evaluation varied d, θ, and t one at a time with the sum $h + 2d$ held equal to w. θ was held at 45° when it was not being varied, d was held at 500 mm when not being varied and t was held at 2 mm when not being varied. Loads were chosen for each geometry such that the mechanism would have a small, but visually discernible displacement at true scale.

The expressions in (13) were found using Wolfram Mathematica and evaluated

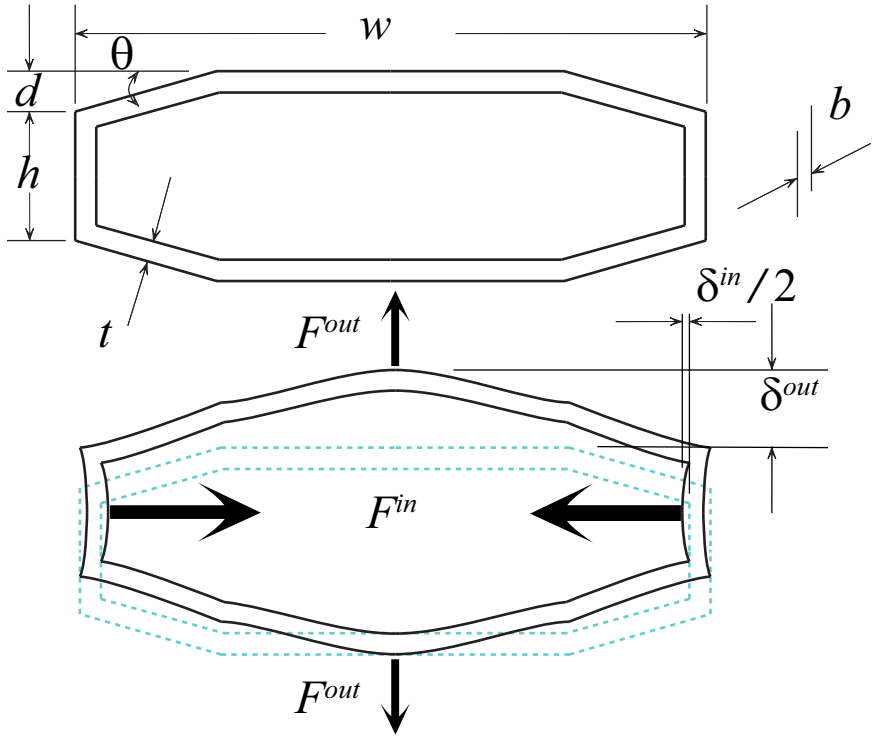

Figure 9: Example parameters for model verification

numerically for the various choices of geometric parameters. The expressions for D_M and the various C_{ij} can be found in Appendix B. One half of the compliant mechanism was simulated for each set of parameters using Dassault Systèmes' SolidWorks Simulation finite element modeling software. The results for various geometries are shown in Tables 1 - 6. In the case of variation of the parameter t, the load was varied so as to keep the final displacement in a consistent range. The level of agreement between the two methods is good, within 1% in most cases for thin mechanisms. As the ratio between t and w approaches 0.1, the accuracy begins to suffer, but for most useful compliant mechanisms, the ratio will be below this value.

3.5 Experimental Results

A series of experiments were performed in order to evaluate how well the expressions developed in the previous sections match the behavior of a true mechanism, which

Table 1: Mechanism displacements, varying d , h, $F_{in} = 0.002$ N, $F_{out} = 0$ N

d [mm]	δ_{in}			δ_{out}		
	FEM	Proposed Method	% difference	FEM	Proposed Method	% difference
2	1.481	1.488	0.47	-1.780	-1.787	0.39
5	1.486	1.487	0.06	-1.782	-1.788	0.34
10	1.479	1.485	0.41	-1.785	-1.791	0.34
50	1.469	1.473	0.27	-1.809	-1.816	0.39
200	1.404	1.409	0.35	-1.928	-1.816	6.16
500	1.225	1.230	0.41	-2.140	-2.127	0.61
900	0.932	0.937	0.54	-1.863	-1.870	0.37
990	0.847	0.852	0.59	-1.696	-1.700	0.23

Table 2: Mechanism displacements, varying θ, $F_{in} = 0.002$ N, $F_{out} = 0$ N

θ [°]	δ_{in}			δ_{out}		
	FEM	Proposed Method	% difference	FEM	Proposed Method	% difference
85	1.462	1.468	0.49	-1.830	-1.836	0.33
80	1.442	1.448	0.42	-1.880	-1.884	0.21
70	1.398	1.404	0.43	-1.966	-1.971	0.26
60	1.344	1.350	0.44	-2.043	-2.048	0.26
30	0.967	0.971	0.41	-2.011	-2.018	0.36

Table 3: Mechanism displacements, varying t, F_{in} variable, $F_{out} = 0$ N

d [mm]	F_{in} [N]	δ_{in}			δ_{out}		
		FEM	Proposed	% difference	FEM	Proposed	% diff
2	0.02	1.481	1.488	0.47	-1.780	-1.787	0.39
5	0.2	7.814	7.874	0.76	-13.50	-13.61	0.81
6		4.515	4.557	0.93	-7.804	-7.88	0.97
10	1	4.372	4.922	1.53	-8.377	-8.51	1.59
25	12	3.641	3.782	3.89	-6.285	-6.535	3.98
50	60	2.196	2.370	7.90	-3.779	-4.087	8.15
100	1200	5.131	5.978	16.5	-8.740	10.24	17.2

Table 4: Mechanism displacements, varying d , h, $F_{in} = 0$ N, $F_{out} = 0.002$ N

d [mm]	δ_{in}			δ_{out}		
	FEM	Proposed Method	% difference	FEM	Proposed Method	% difference
150	-9.43	-9.46	0.33	28.57	28.66	0.31
250	-9.84	-9.88	0.37	27.56	27.65	0.32
500	-10.57	-10.63	0.33	24.52	24.60	0.35
900	-9.31	-9.35	0.45	18.66	18.74	0.47
990	-8.40	-8.52	1.45	16.96	17.04	0.49

Table 5: Mechanism displacements, varying θ, $F_{in} = 0$ N, $F_{out} = 0.002$ N

θ [°]	δ_{in}			δ_{out}		
	FEM	Proposed Method	% difference	FEM	Proposed Method	% difference
45	-10.57	-10.63	0.33	24.52	24.60	0.35
35	-10.47	-10.51	0.36	24.69	24.78	0.35
30	-10.05	-10.09	0.41	25.09	25.18	0.36
27.5	-9.56	-9.69	1.4	25.48	25.5	0.08

Table 6: Mechanism displacements, varying t, $F_{in} = 0$ N , F_{out} variable

d [mm]	F_{in} [N]	δ_{in}			δ_{out}		
		FEM	Proposed	% diff	FEM	Proposed	% diff
2	0.02	-10.57	-10.63	0.33	24.52	24.60	0.35
5	0.02	-0.6753	-0.6806	0.78	1.563	1.575	0.77
	0.2	-6.725	-6.806	1.2	15.45	15.75	1.94
10	2	-8.376	-8.508	1.58	19.39	19.68	1.50
25	24	-6.285	-6.535	3.98	14.56	15.13	3.91
50	60	-3.780	-4.087	8.12	8.778	9.472	7.91
100	1200	-8.748	-10.24	17.06	20.53	23.86	16.2

measured the immittance parameters s_1, s_2, and s_3 for a representative strain amplifying structure. The mechanism used was the outermost layer of the actuator for the biologically inspired camera positioner, the design of which is described in Chapter 5. The full three-layer actuator has a predicted stroke length of 5.6 mm, with a resting length in the output direction of 20.6 mm. By way of comparison, 16 Cédrat APA50XS strain amplified PZT stacks placed in series would have a stroke length of 1.26 mm and a resting length in the output direction of 76.3 mm. The three-layer actuator uses 16 of these in its construction. The geometry of the compliant mechanism is of the class described in section 3.4; it is a constant thickness mechanism whose geometry is parametrized by d, w, h, θ, and t. A photograph of the mechanism is shown in Figure 10 and the numerical values of its parameters are found in Table 7. A rigid section was added to the middle to increase the height, because the chosen value of h does not allow enough space for the internal layers to be placed within this mechanism. The mechanism was machined from a 5mm thick plate of C655 High Silicon Bronze, which has an elastic modulus of 105 GPa and a Poisson's ratio of 0.346.

Figure 10: Mechanism characteristics used in experiment. Parameters are as in Figure 9.

Table 7: Parameter values used in experiment

Parameter	Value	Units
d	2.4	mm
h	1	mm
θ	6	$^\circ$
t	0.15	mm

To identify s_1, s_2, and s_3 experimentally, two experiments were conducted. The first experiment (shown in Figure 11) varied the output displacement with the input fixed and measured input and output force. The second experiment (shown in Figure 12) varied the input displacement with the output free and measured input force and output displacement. Displacement (when it was the dependent variable) was varied using a pair of NAI Aperture micropositioning stages. Force was measured using Futek LSB200 load cells and displacement (when it was an dependent variable) was measured using Microepsilon OptoNCDT laser position sensors. s_1, s_2, and s_3 for this mechanism were determined from the combined data from both experiments using an unweighted least squares regression. Since the data was taken with either the input or output in a fixed or free condition, owing to the nature of the sensors, two experiments were necessary so that the measurements matrix would be full column rank. For instance, placing a load cell at the output would block the laser beam, so that output displacement and output force could not both be measured in the same experiment. Testing in a fixed or free condition gave implicit knowledge that either a force or displacement was zero.

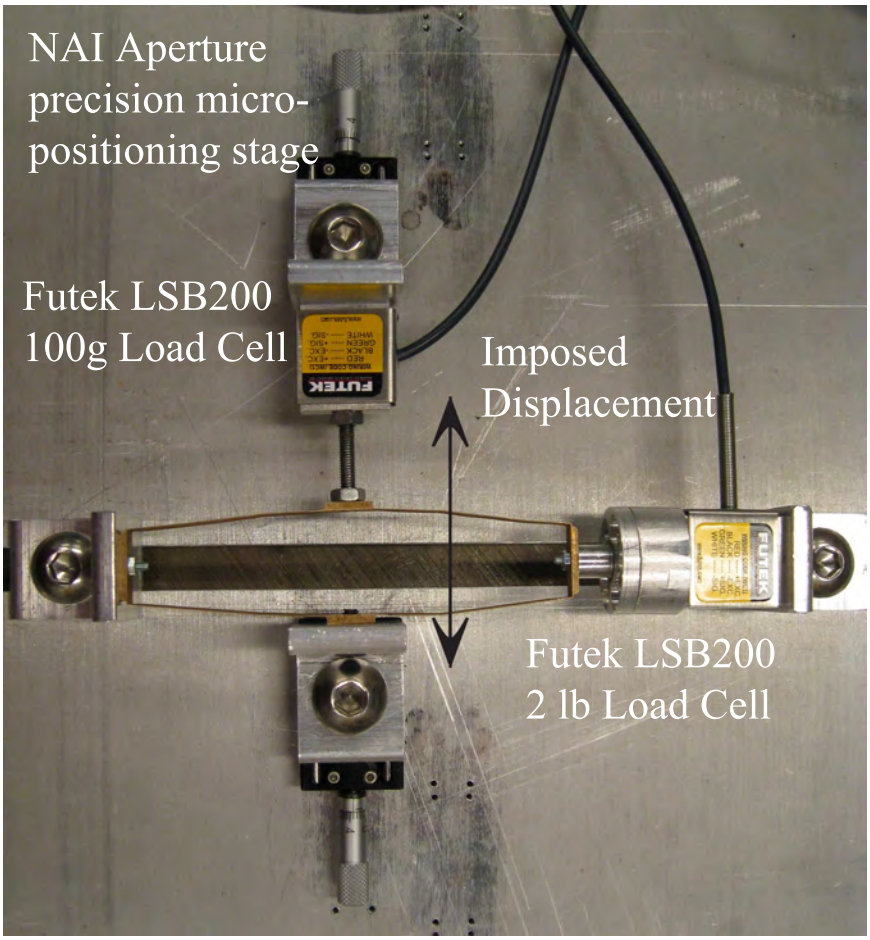

Figure 11: First experiment (input fixed)

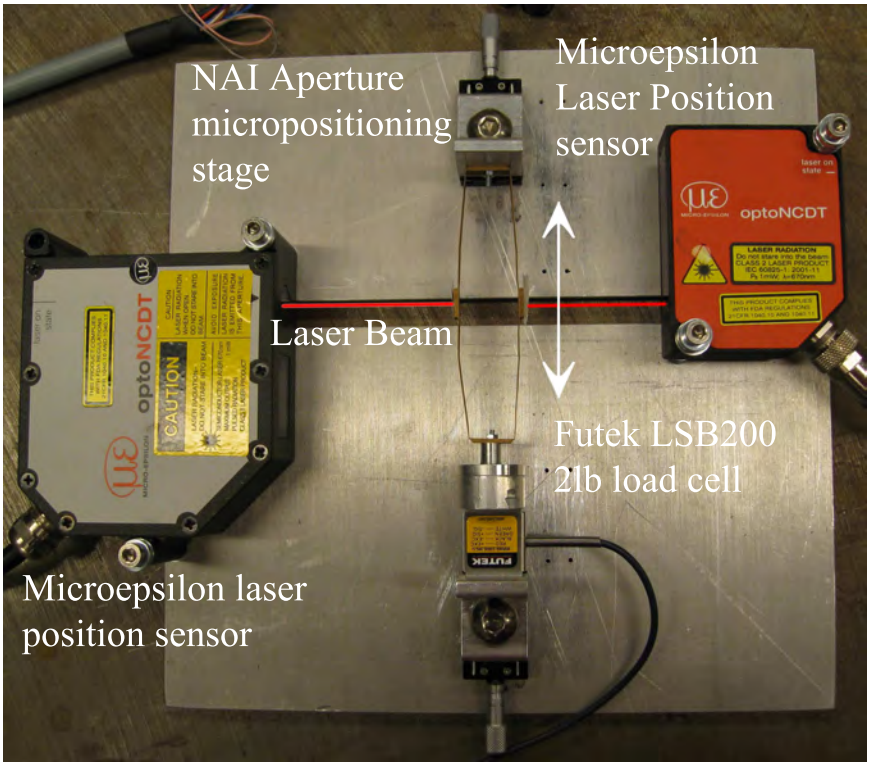

Figure 12: Second experiment (output free)

Table 8: Measured and modeled immittances

Parameter	Analytical Model [N/m]	Experiment [N/m]
s_1	83400	80000
s_2	561	660
s_3	6560	5770

The results of the experiments are shown in Table 8. The analytical model predicts all parameters to within 18%.

3.6 Discussion

The purpose of this theoretical construction of the various immittance parameters is not an end in itself. The goal of the two-port model is to give a designer a simple model that can be used to make an informed choice of geometry in the first iteration of a design of the complete actuator, which consists of several compliant layers. The formulation of this model makes the traditional mechanics of materials

assumptions of linearity and small deformations. In fact, the errors on each of the immittance parameters (which have units of stiffness) are on the order of errors found in experimental evaluations of flexure hinge stiffness [87–89]. This evaluation is more complicated because it is trying to determine a matrix of values that correspond to coupled actions in orthogonal directions, not simply a stiffness in a given direction. Since the mechanism evaluated was the outermost stage of a multistage amplification mechanism for robot-scale displacement, rather than a single-stage mechanism, as in previous works, the displacements are larger. One of the strengths of this modeling approach is that it works equally well for distributed compliance as well as localized compliance. The mechanism shown in Figure 10 takes advantage of this. However, the drawback of distributed compliance is that the deformation can vary more widely with manufacturing tolerances. So it is understandable that the errors are slightly larger.

In addition, the mechanism considered represents an aggressive force-displacement tradeoff, and as a result, the surrounding region of the design space is very sensitive to parameter variations. This is illustrated in Figure 13. When θ is small, varying θ while fixing d can be problematic because it can result in degenerate geometries, so to preserve valid geometries, $d = d' \tan\theta / \tan\theta'$ was chosen when generating the surface shown, where d' and θ' are the nominal values. Although a small change in one of the geometric parameters may affect blocked force and free displacement only slightly, the immittances can vary widely.

Because the mechanism tested was so fragile, some permanent deformation occurred either through the manufacturing process or shipping and handling. It was assumed that the immittances would not be largely changed by this deformation, but the residual stresses may have contributed to some of the error. There was some compliance inherent in the micropositioning stages and the load cells and this may have introduced some error in measurement. There also may have been some variation in

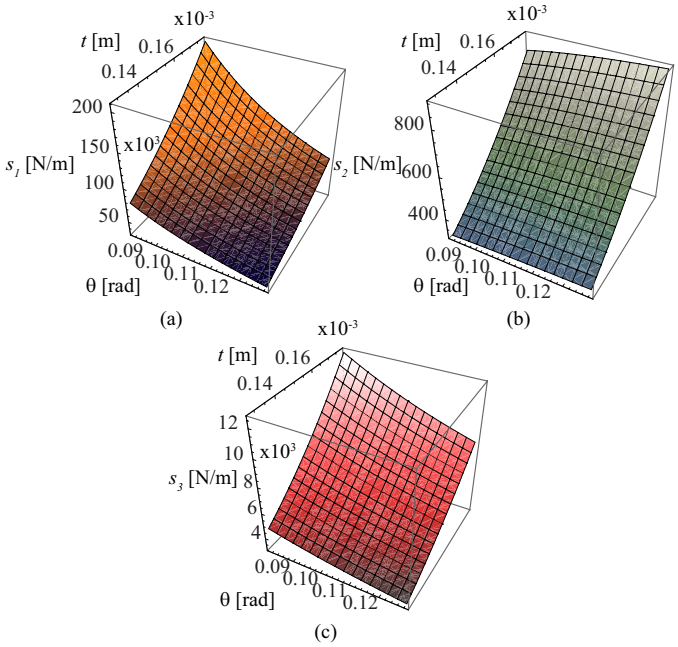

Figure 13: Variation in immittance parameters: (a) s_1, (b) s_2, (c) s_3 with geometry

the material constants from typical tabulated values.

3.7 Summary

Piezoelectric stack actuators have the potential to be of great usefulness in robotics applications, but are limited by their low strain rate. This can be mitigated by the use of compliant strain amplification mechanisms. This chapter presents a generalized Euler-Bernoulli formulation for the two-port model of any doubly symmetric strain amplification mechanism composed of a single loop of initially straight rectilinear segments. Unlike previous works, which either present purely numerical two-port models, or lists of long expressions, this provides an analytical two-port model. This higher level of abstraction is a prerequisite for studying interconnections of these units because without it the expressions can become unwieldy, as well as topologically troublesome. A motivating example is shown for a particular class of mechanism described by 5 geometric parameters. The model for this example has been verified by finite element methods. In addition, a particular mechanism of this type has

been evaluated experimentally and shows good agreement, with an accuracy better than 18%. The analytical model for the two-port network can be used to eliminate guesswork as to how many layers of amplification should be used in a nested compliant mechanism. In Chapter 4, further interesting properties that emerge from nested compliant mechanisms will be discussed and Chapter 5 will show how the models developed in this chapter are used to choose geometries of each layer in response to desired performance specifications.

CHAPTER IV

NESTED HIERARCHICAL STRAIN AMPLIFICATION MECHANISMS

The two-port network formalism described in Chapter 3 provides the necessary abstraction to describe the interconnections between the various stages in a simple, tractable manner. Using this formalism, several interesting characteristics emerge. When the geometries of the layers are chosen appropriately, it is possible to produce actuators with strain rates, stiffnesses, displacement range, and force capability suitable for many novel robotic applications. Layer geometry selection will be demonstrated in Chapter 5, but first it is important to present some key mathematical characteristics of nested hierarchical strain amplification.

This chapter presents some useful theoretical results that emerge when considering hierarchical interconnections of strain amplifying mechanisms when the immittance parameters for each layer are known. The formulation considers a hierarchy that may include large numbers of layers. Although the examples and experiments are conducted on rhomboidal mechanisms, the results of sections 4.1, 4.4, 4.6, and 4.11 can be applied to a wide variety of hierarchical geometries, provided each stage admits a two-port representation.

When studying mechanisms of this type, it quickly becomes apparent that making the assumption that all internal layers operate at either their blocked force or free displacement results in models that fail to predict the output performance. Instead, for a given load/displacement characteristic, each internal layer is at some intermediate force and displacement. There is not much value in computing these explicitly, but they are important internal variables in the system. The key unifying theme is that

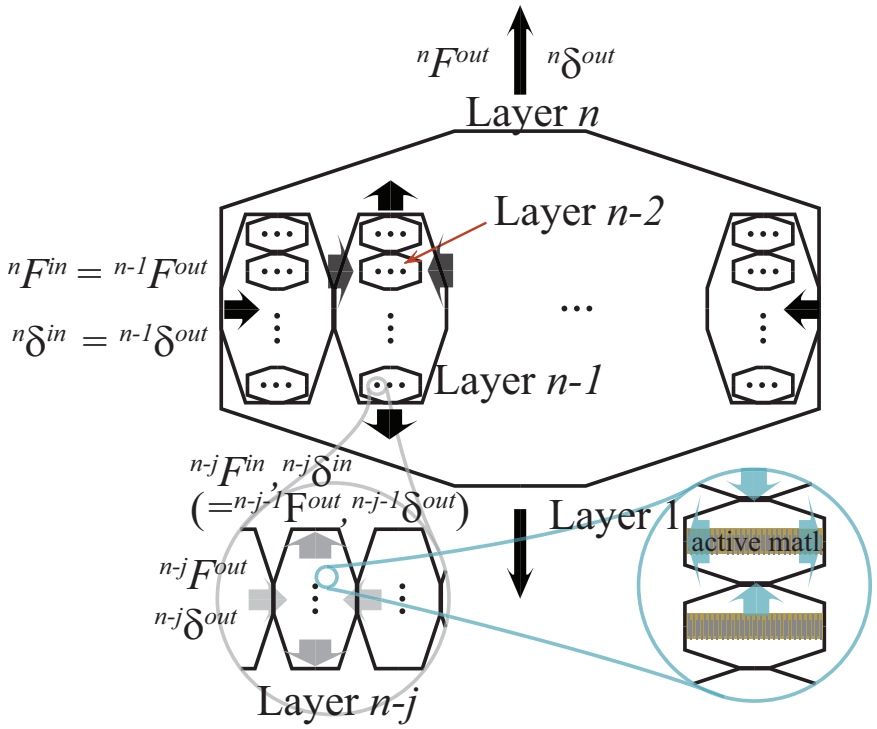

Figure 14: Diagrammatic construction of a hierarchical nested strain amplifying mechanism. The term *nested* is used because each stage is typically placed inside the subsequent stage. The force and displacement produced by each stage serves as the input to the next.

the output force and displacement of a given layer is the input force and displacement to the subsequent layer, as illustrated in Figure 14. Beginning with this fact, with knowledge of the immittances, the overall behavior and properties can be elegantly described.

4.1 Performance metrics

Amplified piezoelectric stacks are unlike servomotors in several respects. Most importantly, their force is not constant with stroke, but decreases with displacement. Likewise, muscle forces depend on the length [26]. There are 3 natural metrics associated these types of actuators, illustrated in Figure 15. The first (a) is the stiffness of the de-energized actuator as perceived from the environment. The second (b) is the free displacement, or the maximum displacement achieved when the actuator is

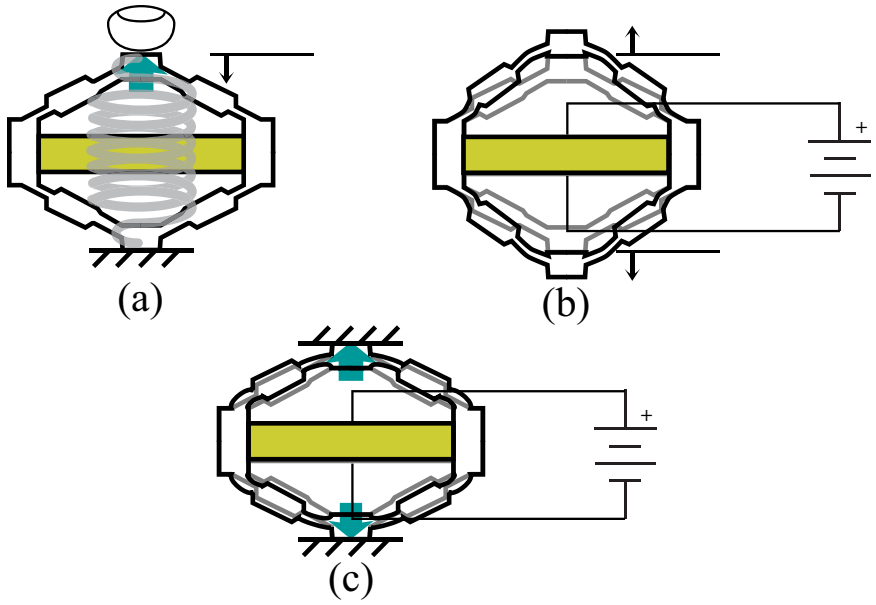

Figure 15: Performance metrics for compliant actuators

energized. At this point the actuator can impose zero force on the environment. The third (c) is the blocked force, or the force applied to the environment when the environment prevents the actuator from moving. This is equivalent to an isometric contraction in muscle.

Like biological actuation systems, these actuators can only contract, not extend. Therefore they are often used in antagonistic configurations with a second actuator.

4.2 Antagonistic connections

Consider a mechanism driven antagonistically by two identical multi-stage amplified actuators in the absence of any external load, with no preload at the neutral position, such as the camera positioner illustrated in Figure 16. Each actuator consists of m piezoelectric stacks with n layers of amplification. To achieve some desired position, one of the cellular actuators (henceforth called the "active" actuator, or agonist) will be energized, and will contract. Its antagonist (the "passive" actuator) will not be energized, but will, due to its inherent stiffness, oppose the motion of the active actuator. Therefore, the active actuator will stop short of its free displacement.

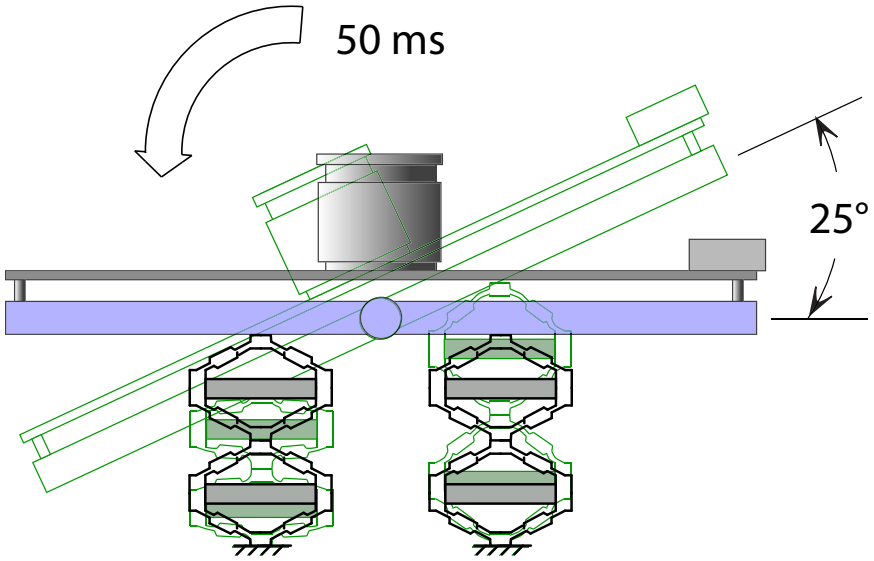

Figure 16: Camera driven by an antagonistic pair

Using a two-port network framework [28] and assuming the material properties and terminating electrical impedance characteristics of the piezoelectric stack are known, it is possible to predict the maximum displacement of the antagonistically driven device.

4.3 Interconnecting two-port strain amplifying mechanisms

The amplification mechanism of each layer can be described by a two-port network model using the methods in Chapter 3. Recall that the mathematical relationship between the input and output to the mechanism is described by:

$$\begin{bmatrix} F_{in} \\ F_{out} \end{bmatrix} = \begin{bmatrix} s_1 & s_3 \\ s_3 & s_2 \end{bmatrix} \begin{bmatrix} \delta^{in} \\ \delta^{out} \end{bmatrix}, \tag{15}$$

where F_{in}, F_{out}, δ_{in} and δ_{out} denote the forces and displacement at the input and output ports, respectively. s_1, s_2, and s_3 have units of stiffness and are functions of the geometry and material properties. The matrix in (15) is the stiffness matrix, one of several *immittance* matrices [28] that is used to describe the two-port network relationship. The strength of the two-port network approach is that it accurately

accounts for the effects of both the control force applied by previous layers and environmental or load forces from subsequent layers. Using this framework, it is possible to model systems that do not have the high input impedance/low output impedance characteristics necessary in most branches of circuit analysis. An alternate way of expressing this is to say that the two-port (or multiport) network succeeds in modeling devices that have significant "back effects."

The innermost, or "zeroth," layer of a nested cellular device will be some active material of known characteristic. Typically the manufacturer tabulates the totally blocked, or clamped, force and the mechanical stiffness. This can be represented as a Norton equivalent circuit, as shown in Figure 17, where the clamped force is represented by a current source, and the mechanical stiffness is represented by the Norton resistance. The displacement of this device, which is analogous to the voltage across the Norton resistance, will depend on the load impedance. Several of these zeroth layer units can be combined in series, and their Norton circuits combined according to the methods of circuit analysis. The voltage across the Norton equivalent resistance corresponds to the input displacement of the first layer displacement amplification mechanism. The current to the load impedance corresponds to the input force. When the amplification mechanism is represented as a two-port network, this is the voltage and current at the left hand port. With appropriate mechanical analogies, this can be expressed as:

$$F_1^{in} = F_0^{block} - k_0 \delta_1^{in} \tag{16}$$

Because series combinations of springs add compliances, not stiffnesses, the Norton equivalent resistance is set to $1/k_0$. Interconnections between networks are described in terms of matrix operations on the immittance matrices and are well known [28]. Therefore any combination of two-port networks can be readily analyzed. The topological relationships between the various layers in the hierarchy will be represented

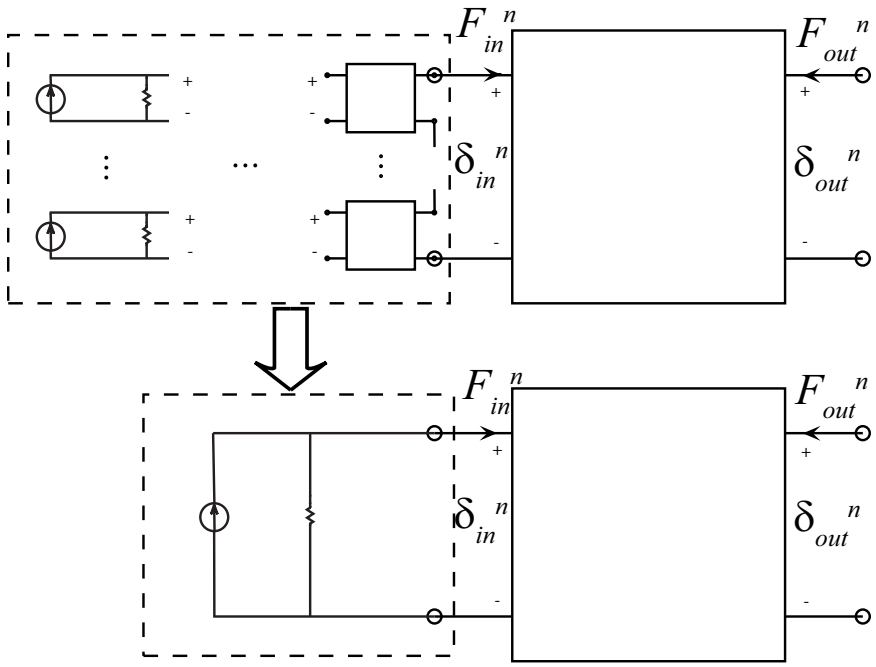

Figure 17: collapsing of two-port networks. Each square box represents a two-port network, with a voltage and current at the right and left hand ports. The entire hierarchy within the dashed lines is collapsed and replaced with its Norton circuit.

by the electrical connections of their two-port models.

4.4 Collapsing nested two-port models to Norton circuits

Since the impedance characteristic at the input to the first amplification layer is known, and the immittances of the amplification mechanism's two-port model is known, the entire connection can be "collapsed" and replaced with its Norton equivalent circuit that represents the characteristic at the output of the first layer. This can be performed repeatedly, up to the outermost layer, which connects to the load. Figure 17 illustrates collapsing connections of two-port networks. The following derives the equations that describe the collapsing process.

Consider an active material with blocked force F_0^{block} and stiffness k_0. The output of this Norton circuit is applied to the left hand port of a two-port network representing the first layer amplification mechanism. The displacement of the zeroth layer, δ_1^{in}, is analogous to the voltage across the Norton resistance. To collapse the first

layer, it is not necessary to assume a particular output impedance at the right hand port of the two-port network. Using (16) and (15) the two-port relationship can be represented by the following equation:

$$\begin{bmatrix} F_0^{block} - k_0\delta_1^{in} \\ F_1^{out} \end{bmatrix} = \begin{bmatrix} s_1 & s_3 \\ s_3 & s_2 \end{bmatrix} \begin{bmatrix} \delta_1^{in} \\ \delta_1^{out} \end{bmatrix} \tag{17}$$

Solving the upper of the two equations for δ_1^{in} results in the following expression:

$$\delta_1^{in} = \frac{F_0^{block} - s_3\delta_1^{out}}{s_1 + k_0} \tag{18}$$

Substituting this into the lower of the two equations in (17) and collecting terms results in the following:

$$F_1^{out} = \frac{s_3 F_0^{block}}{s_1 + k_0} + \frac{s_2(s_1 + k_0) - s_3^2}{s_1 + k_0}\delta_1^{out} \tag{19}$$

Defining the following:

$$F_1^{block} = \frac{s_3 F_0^{block}}{s_1 + k_0} \tag{20}$$

$$k_1 = \frac{s_2(s_1 + k_0) - s_3^2}{s_1 + k_0} \tag{21}$$

(19) can be written as:

$$F_1^{out} = F_1^{block} + k_1\delta_1^{out}. \tag{22}$$

This has physical significance; F_1^{block} is the fully blocked force of the displacement amplified active material, and $k_1\delta_1^{out}$ is the stiffness as seen from the output of the mechanism. Since this is an equivalent stiffness for the nested connection, it is referred to as the *lumped stiffness*. In the Norton equivalent circuit, F_1^{block} corresponds to the current source and $\frac{1}{k_1\delta_1^{out}}$ corresponds to the equivalent Norton resistance. This procedure can be performed repeatedly for each subunit in the hierarchy.

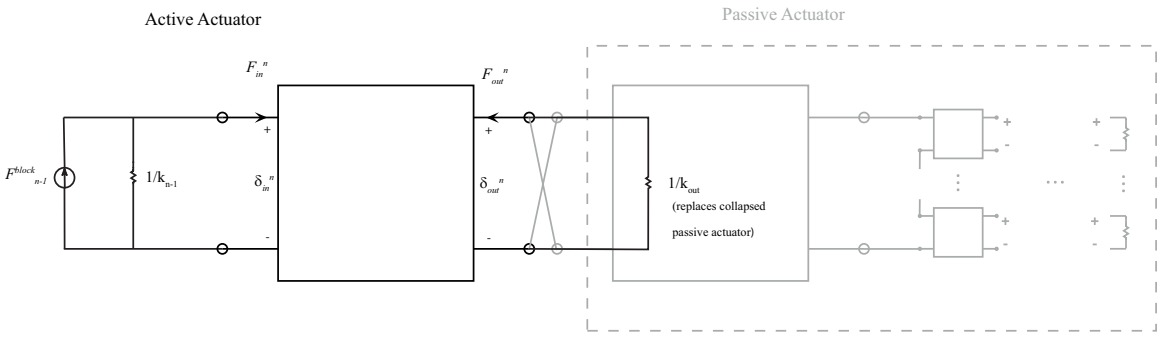

Figure 18: Two port representation of antagonistic pairs. The active actuator is in black and has all but the outermost layer collapsed and represented by its Norton circuit. The passive actuator is in gray and is will be replaced by a simple stiffness).

4.5 Displacement of the mechanism against the passive actuator

Modeling the device driven by the antagonistic pair as a rigid body that rotates about a frictionless pivot, with no acceleration, the following relations hold:

$$\delta^{out}_{active} = -\delta^{out}_{passive} \tag{23}$$

$$F^{out}_{active} = F^{out}_{passive} \tag{24}$$

Assume that the antagonistic actuators are identical. Because the passive actuator is off, the current source F_0^{block} will be zero. The stiffness, k_0, at the zeroth layer of the passive actuator will depend on the electrical terminating impedance on the leads of the active material.

Because the passive actuator is not energized, it can be completely collapsed and simply be represented as a terminal resistance $\frac{1}{k_{eq}}$ across the active actuator. This is illustrated in Figure 18. The displacement of the antagonistic mechanism corresponds to the voltage across the right hand port of this outermost layer.

Using (17) and Ohm's law, solving for δ_n^{out} gives:

$$\delta_n^{out} = -\frac{s_3 F_{n-1}^{block}}{s_1 s_2 - s_3^2 + k_{eq}(s_1 + k_{n-1}) + s_2 k_{n-1}}. \tag{25}$$

The free displacement of the actuator (against its own stiffness) has $k_{eq} = 0$ or:

$$\delta^{free} = -\frac{s_3 F_{n-1}^{block}}{s_1 s_2 - s_3^2 + s_2 k_{n-1}}. \tag{26}$$

Taking the ratio of the two:

$$\frac{\delta_n^{out}}{\delta^{free}} = \left(1 + \frac{k^{out}(s_1 + k_{n-1})}{s_1 s_2 - s_3^2 + s_2 k_{n-1}}\right). \tag{27}$$

Assuming that the electrical terminating impedance of the passive actuator is chosen such that the zeroth layer has the same mechanical stiffness as that on the active side, using (20) the stiffness from the point of view of the output can be written as:

$$k^{out} = \frac{s_2(s_1 + k_{n-1}) - s_3^2}{s_1 + k_{n-1}}. \tag{28}$$

substituting into (27) gives $\delta_n^{out}/\delta^{free} = 1/2$. Therefore, in an antagonist configuration with identical actuators, each actuator must be designed so that its free displacement is double that required by the angle specification.

4.6 Nesting of layers

If a passive actuator is in an antagonistic pair arrangement with an active actuator, it will appear to the active actuator as a stiffness. This stiffness will depend on the immittances of the previous layers, as well as the terminal stiffness of the zeroth layer. This section will consider an amplified mechanism with n layers, with the outermost layer (the actuator connected to the load) denoted layer n. The innermost layer (the actuator connected to the active material) will be denoted layer 1. Immittances for a given layer will be denoted with a leading superscript. k will be used to count layers outward from the active material, and $j \in \mathbb{N} \mid n - j \in [\ 0,\ k\ ]$ will be used to count layers inward from outermost. The stiffness of a passive actuator with n layers is

$$k_{passive} =^{n} s_2 - \cfrac{^{n}s_3^2}{^{n}s_1 +^{n-1} s_2 - \cfrac{^{n-1}s_3^2}{^{n-1}s_1+^{n-2}s_2-\cfrac{^{n-2}s_3^2}{^{n-2}s_1+^{n-3}s_2-\ddots}}}}. \tag{29}$$

For the jth layer, denoting

$$^{j}x =^{n-j} s_2 - \frac{^{n-j}s_3^2}{^{n-j}s_1 + k_{n-j-1}} \tag{30}$$

where k_{n-j-1} is the lumped stiffness of the $j-1st$ layer and subsumes all terms for $i > j$, it can be stated that:

$$-\frac{^{n-j}s_3^2}{^{n-j}s_1} <^{j-1} x -^{n-j} s_2 < 0. \tag{31}$$

Therefore, approximating the stiffness of the passive actuator by truncating remaining terms in the denominator will result in a conservative estimate of the displacement for a nested structure.

4.7 Estimating stiffnesses of actuators with large numbers of layers

(29) has a form of a continued fraction. This results in some desirable properties. The following section will show that for an actuator with a large number of layers, the properties of the entire actuator can be approximated to a desired degree of accuracy by replacing the continued fraction representing the remaining layers by an arbitrary constant. In the literature [90, 91], these approximations are known as *convergents*.

This section intends to show that the sequence of convergents P_j is Cauchy, and therefore, all convergents beyond some finite k lie within some interval of size ϵ of P_k on $\mathbb{R}$.

Lemma 1. *All denominators for the continued fraction expansion of the stiffness of a nested linearly elastic mechanism are positive.*

Proof. Each compliant mechanism has a positive definite immittance matrix. Therefore, the determinant for any layer, ${}^k s_1^k s_2 -^k s_3^2 > 0$. Because any realizable nested actuator will have a finite number of compliant mechanisms, the continued fraction expansion terminates. The sequence of continued fraction expansions for the lumped stiffness at the output of each layer, beginning with the innermost, will be referred to as z_k. The zeroth term of the sequence, z_0 is constant. Because the stiffness is derived from passive elastic material, z_0 will be positive, and all elements of the immittance matrix are positive. The remaining terms of the sequence can be expressed by the recursive relation:

$$z_k =^k s_2 - \frac{{}^k s_3^2}{{}^k s_1 + z_{k-1}} \tag{32}$$

This can be rewritten as

$$z_k = \frac{{}^k s_2^k s_1 -^k s_3^2 +^k s_2 z_{k-1}}{{}^k s_1 + z_{k-1}} \tag{33}$$

if $z_{k-1} > 0$, $z_k > 0$. The proof is completed by induction on k. □

When a force is applied at the output of a compliant mechanism, it not only causes a deformation in the output direction; it causes a deformation in the input direction as well. This deformation at the input has an effect equivalent to a force transmitted back to the output, even when no load is applied at the input. Essentially, Lemma 1 says the effective stiffness due to this back, then forward transmission, s_3^2/s_1 will always be less than the input–clamped output stiffness, s_2.

Lemma 2. *In the set of all terminating continued fractions of the form:*

$$\left\{ p_k = a_0 - \cfrac{b_1}{a_1 - \cfrac{b2}{a_2 - \cfrac{b3}{\ddots \cfrac{}{a_{k-1} - \frac{b_k}{c_k}}}}} \;\middle|\; a_i, b_i > 0 \quad \forall i, c_k \in \left(\frac{b_k}{a_{k-1}},\ c_{max} \right] \right\} \tag{34}$$

with a_i, b_i constant the maximum p_k is achieved by choosing the maximum c_k, c_{max}.

Proof. For $k = 1$, $p_k = a - \frac{b}{c}$. It is clear that this quantity is maximized by the largest possible c. For the general case: define the quantity $a_k - \frac{b_k}{c_k} = c_{k-1}$. c_{k-1} is maximized by $c_k = c_{max}$. Therefore, by induction, choosing the maximum c_k maximizes all denominators, and p_k is minimized. □

This is equivalent to saying that the stiffest possible nested structure for a given number of layers (proceeding from the outside in) can be realized by clamping the input of the innermost mechanism considered.

Theorem 1. *The sequence of convergents of the continued fraction expansion of the stiffness of a nested mechanism, with successive denominators for $n - j < k$ replaced by ${}^{k-1}s_1 +^k s_2$ is Cauchy.*

Proof. Any continued fraction can be represented by:

$$p_n =^n s_2 - \cfrac{{}^n s_3^2}{{}^n s_1 +^{n-1} s_2 - \cfrac{{}^{n-1} s_3^2}{{}^{n-1} s_1 + \cfrac{\ddots}{{}^{n-j+2} s_1 +^{n-j+1} s_2 - \cfrac{{}^{n-j+1} s_3^2}{{}^{n-j+1} s_1 + z_j}}}}}. \tag{35}$$

This considers the denominators from the top level, n, down to level $n-j$; z_j represents the continued fraction expansion for the remaining layers. It can be approximated by:

$$z_j \approx^{n-j} s_2 - \frac{{}^{n-j} s_3^2}{{}^{n-j} s_1 +^{n-j-1} s_2}. \tag{36}$$

Let y_j represent the convergent where z_j is replaced by the approximation in (36). y_{j-1} represents the previous convergent in the sequence, replacing the final z_j by ${}^{n-j}s_2$. By lemma 1, the quantity $\frac{{}^{n-j}s_3^2}{{}^{n-j}s_1 + z_j}$ will be positive for all j. Also from lemma 1, it can be determined that this quantity will not exceed ${}^{n-j}s_2$. y_{j-1} and y_j are identical except for the terminating constant. Therefore, they are both of the form of the

continued fraction in lemma 2. y_{j-1} terminates with the constant $c_k = ^{n-j} s_1 + ^{n-j} s_2$ and y_j terminates with the constant $c_k = ^{n-j} s_1 + ^{n-j} s_2 - \frac{^{n-j}s_3^2}{^{n-j}s_1 + ^{n-j-1}s_2}$. By lemma 2, and induction on j, the sequence of convergents is monotonically decreasing, or

$$y_{j-1} > y_j \ \forall j. \tag{37}$$

Applying lemma 1 at level n, the sequence is bounded below by 0. Since the sequence is monotonically decreasing and bounded below, it must be Cauchy. □

For any Cauchy sequence, for any arbitrary ϵ, one can find a k such that all terms in the sequence beyond k are within a distance ϵ from one another [92]. Physically speaking, this means that for an actuator consisting of nested compliant mechanisms, a roboticist can approximate its stiffness to some desired accuracy by considering merely the outer k layers and considering the lumped stiffness of the $k-1^{st}$ layer to be infinite. Alternatively, the kth layer can be said to be clamped at its input.

Theorem 1 says that outer layers, regardless of whether they are rigid or compliant, have the greatest effect on the stiffness of the overall actuator. Therefore, the innermost layers do not need to have as strict tolerances as the output layers to achieve a uniform result from actuator to actuator. It also means that the electrical terminating impedance of the passive actuator is not critical for actuators with large numbers of layers, justifying the assumption made in Section 4.5. The procedure of Theorem 1 provides an upper bound on the true stiffness.

An alternate choice is to approximate z_j by $^{n-j}s_2 - \frac{^{n-j}s_3^2}{^{n-j}s_1}$ instead. The sequence of these approximants (which are not convergents, strictly speaking, since they do not result from a strict truncation) will be denoted by x_j. This is equivalent to the stiffness perceived at the output when the innermost mechanism is considered free to deform in the input direction. It will be shown that y_j and x_j have the same limit.

Theorem 2. *The sequences y_j and x_j converge to the same limit.*

Proof. Any continued fraction of the form in Lemma 2 can be represented by the recursive relation:

$$\begin{aligned} B_{j+1} &= a_{j+1}B_k - b_{j+1}B_{j-1} \\ A_{j+1} &= a_{j+1}A_k - b_{j+1}A_{j-1} \\ y_{j+1} &= \frac{B_{j+1}}{A_{j+1}} \\ B_{-1} &= 1 \\ B_0 &= a_0 \\ A_{-1} &= 0 \\ A_0 &= 1 \end{aligned} \tag{38}$$

This is shown in Rockett and Szüsz [91]. In this case $a_{j+1} =^{n-j+1} s_1 +^{n-j} s_2$ and $b_{j+1} =^{n-j+1} s_3^2$. Using an a similar procedure, it is simple to demonstrate that x_{j+1} can be written as:

$$x_{j+1} = \frac{B_{j+1} - k_{j+1}B_j}{A_{j+1} - k_{j+1}A_j} \tag{39}$$

where $k_{j+1} = \frac{^{n-j}s_3^2}{^{n-j}s_1}$. Note that each term of x_j is written in terms of the B_j, A_j used to construct y_j. It can be shown that the sequence $y_j - x_j$ approaches zero in the limit. After algebraic manipulations, the $j+1^{st}$ term of the sequence can be written as:

$$y_{j+1} - x_{j+1} = \frac{y_j - y_{j+1}}{\frac{A_{j+1}}{k_{j+1}A_j} - 1}. \tag{40}$$

The numerator approaches zero for large j by Theorem 1. To show that the entire sequence goes to zero it is sufficient to show that $\frac{A_{j+1}}{A_j} \neq k_{j+1}$. This can be proved by contradiction.

Assume that for all j greater than some k the sequence $\frac{A_j}{A_{j-1}} = k_j$. Then $\frac{A_{j+1}}{A_j} = k_{j+1}$. This can be rewritten as:

$$A_{j+1} = k_{j+1}A_j = a_{j+1}A_j - b_{j+1}A_{j-1}. \tag{41}$$

collecting terms and substituting in the immittances results in:

$${}^{n-j}s_3^2 A_{j-1} = \left({}^{n-j}s_1 + {}^{n-j-1}s_2 - \frac{{}^{n-j-1}s_3^2}{{}^{n-j-1}s_1}\right) A_j. \tag{42}$$

This quantity will be divided by A_{j-1}. Since j is assumed to be greater than k, the sequence $\frac{A_j}{A_{j-1}} = k_j$. Substituting in for this quantity in terms of the immittances:

$${}^{n-j}s_3^2 = \frac{{}^{n-j}s_3^2}{{}^{n-j}s_1}\left({}^{n-j}s_1 + {}^{n-j-1}s_2 - \frac{{}^{n-j-1}s_3^2}{{}^{n-j-1}s_1}\right). \tag{43}$$

Simplifying:

$$\frac{{}^{n-j-1}s_2\,{}^{n-j-1}s_1 - {}^{n-j-1}s_3^2}{{}^{n-j-1}s_1\,{}^{n-j}s_1} = 0. \tag{44}$$

All ${}^k s_i$ are finite, and the numerator of (44) is simply the determinant of the immittance matrix for layer $n-j-1$. This must be strictly positive for all j, hence the contradiction and the result is proved. □

A simple numerical example of the convergence is shown in Figure 19. Two-port network immittance parameters were chosen randomly for each of the 6 layers with ${}^k s_1 \in (0, 18)$, ${}^k s_2 \in (0, 27)$, and ${}^k s_3 \in (0, \min[\sqrt{{}^k s_1^k s_2},\ 16])$.

The lumped stiffness of the remaining unconsidered layers will be in the interval $[0, \infty)$. x_j represents the stiffness of the actuator when this lumped stiffness for the remaining layers is zero. y_j represents the stiffness of the actuator when this lumped stiffness for the remaining layers is infinite. For a finite nonzero compliance, the stiffness of the overall actuator should be between the values of x_j and y_j. Since these are the same in the limit, then the compliance of the innermost layers have

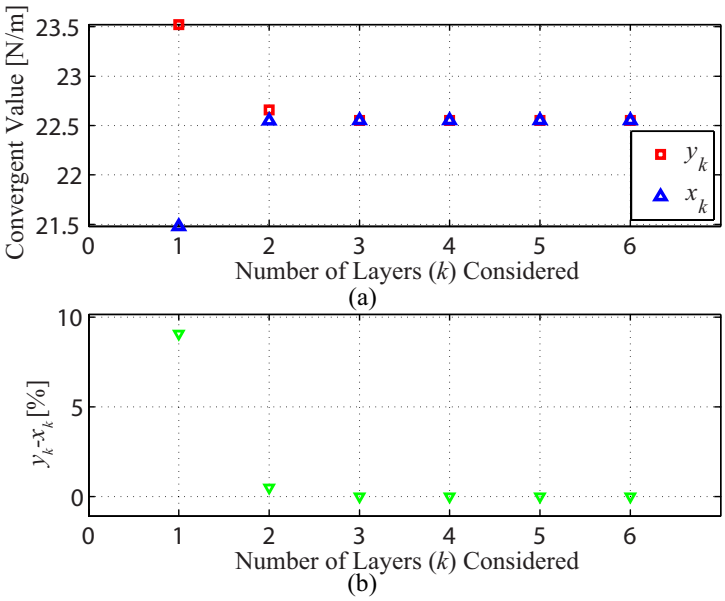

Figure 19: Convergence of the various approximations for passive actuator stiffness.

a negligible effect on the overall stiffness of the passive actuator for actuators with many layers.

4.8 Experimental evaluation of stiffness convergents

In order to see how these theorems apply to an engineering situation, this section will examine the convergents for a particular actuator with known immittances for each layer. The details of how the geometry of each layer was chosen will be presented in Chapter 5. The immittance parameters for each rhomboidal strain amplification mechanism can be calculated from the geometry using the method in Chapter 3. These immittances can be used to calculate the convergents.

The convergents can be measured using a collection of experiments. The experiment that measures y_0 takes the third layer alone, as it is the outermost layer. The third layer is fixed in the input direction as shown in Figure 20. The output position is varied using an NAI aperture micropositioning stage, and the force is recorded using a Futek LSB200 load cell with a 1 N range. y_0 was determined from a linear fit to the force-displacement data. Because the input was fixed, the experiment is really

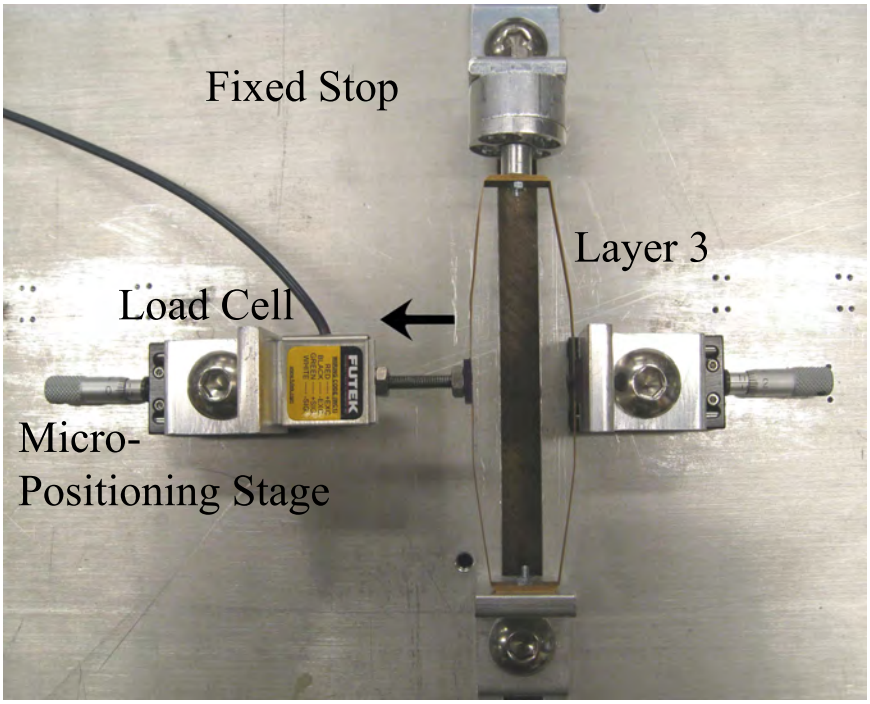

Figure 20: Experimental evaluation of y_0

recording the stiffness of half the rhomboidal mechanism. Therefore, the mechanism was inverted and the procedure repeated, and the average value taken.

To measure x_0, a similar procedure was used, shown in Figure 21. This time the input is free to contract along the major axis (input) as the minor (output) axis extends. x_0 was recorded from a linear fit to the force-displacement data.

To measure y_1, the second layer was installed within the third layer, and a steel block was installed along the input axis of each rhomboid in the second layer, as shown in Figure 22. The steel block can be considered rigid compared to the rhomboidal mechanisms. The output of the third layer was extended using the micropositioning stage as in the previous experiments. x_1 was determined using the same setup, but with the blocks removed. Both were determined from linear fits to the force-displacement data.

The first layer is the strain amplifying mechanism incorporated into the APA50XS, and there is no way to test it independently without damage. Cédrat also tabulates

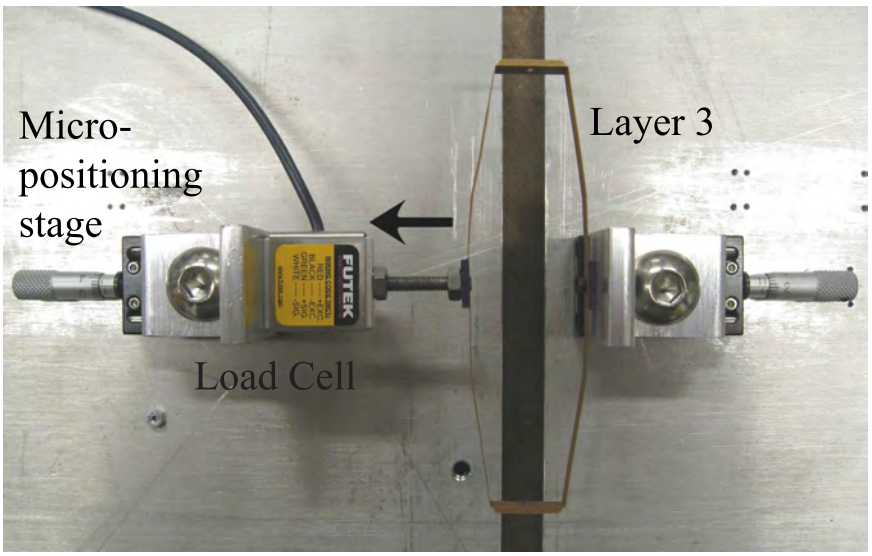

Figure 21: Experimental evaluation of x_0

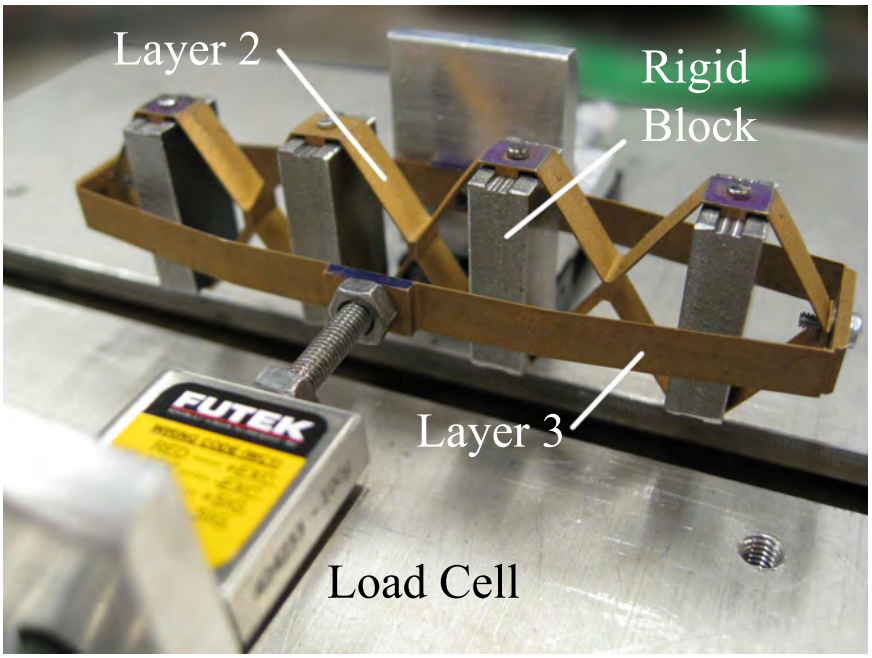

Figure 22: Experimental evaluation of y_1. The evaluation of x_1 is similar, but with the rigid blocks removed. $y_2 = x_2$ is similar, but with the rigid blocks replaced by Cédrat APA50XS amplified piezoelectric actuators.

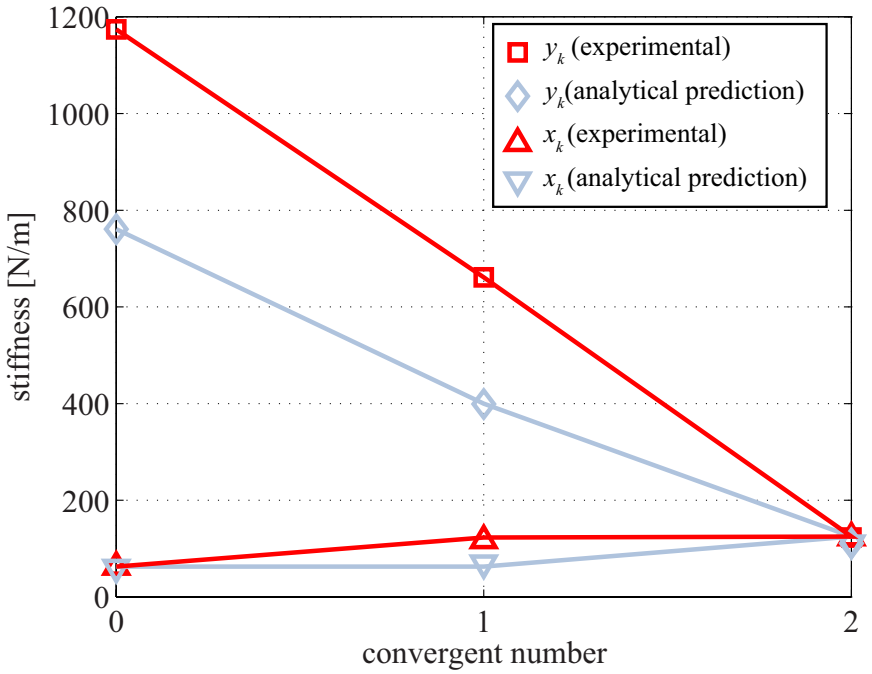

Figure 23: Measured and theoretical stiffness convergents for a 3 layer cellular actuator

the blocked force and stiffness for the entire part, not separately for the piezoelectric stack and compliant mechanism. Therefore, the continued fraction is considered to terminate here, and x_2 ,y_2 and the lumped stiffness are synonymous. This value is equal to F^{block}/δ^{free}. Since F^{block} and δ^{free} are important in their own right, experiments are conducted in subsequent sections to determine these quantities separately. The resulting values were used to determine the experimental lumped stiffness value. The experimental results and analytical predictions are shown in Figure 23. Although the individual values themselves vary due to manufacturing inaccuracies and misalignments in the setup, it is clear that the sequences x_k and y_k are monotonically increasing and monotonically decreasing, respectively, and that they converge to the same limit. Hence, the consequences of the theorems are borne out by real engineering situations.

4.9 Blocked force and free displacement measurements

In addition to verifying the stiffness of the actuator, the blocked force and free displacement were evaluated on the complete actuator prototype. The goal was to see not only how closely the actuator matched the predicted values based on the model, but also to see how repeatable the force and displacement values at the output are when different combinations of piezoelectric stacks are activated.

The experiment to measure the blocked force is similar to that shown in Figure 22, however, each rigid block is replaced with a set of first layer units (4 Cédrat APA50XS amplified piezoelectric stacks in series). Each piezoelectric stack is activated one at a time. The output is held stationary. The force at the output is measured and recorded using the Futek LSB200 load cell for each level of activation. When all inputs have been activated, they are deactivated one by one and the forces recorded. 16 trials were conducted, with an arbitrary activation/deactivation order each time. The results are shown in Figure 24. Figure 24 shows that the force profile is quite linear and very repeatable regardless of the order in which the piezoelectric stacks are activated. Although the maximum blocked force falls short of the 0.907 N predicted by the theoretical model for this geometry, it shows there is enough fidelity for the model to be useful in generating the first iteration of a nested multilayer actuator design. Accuracy will likely be better for less aggressive force/displacement tradeoffs and will improve with better manufacturing and assembly techniques. The study of manufacturing processes for these devices is beyond the scope of this thesis.

The free displacement of the actuator is measured using the setup shown in Figure 25. Due to the weight of the piezoelectric stacks and the low out of plane rigidity of the third layer, there will be significant deflection if the actuator is suspended from one end. For this reason the actuator is clamped at its centroid and both mounting flanges are allowed to extend outward as piezoelectric stacks are activated. The piezoelectric stacks are activated one by one as in the blocked force experiment. The position of

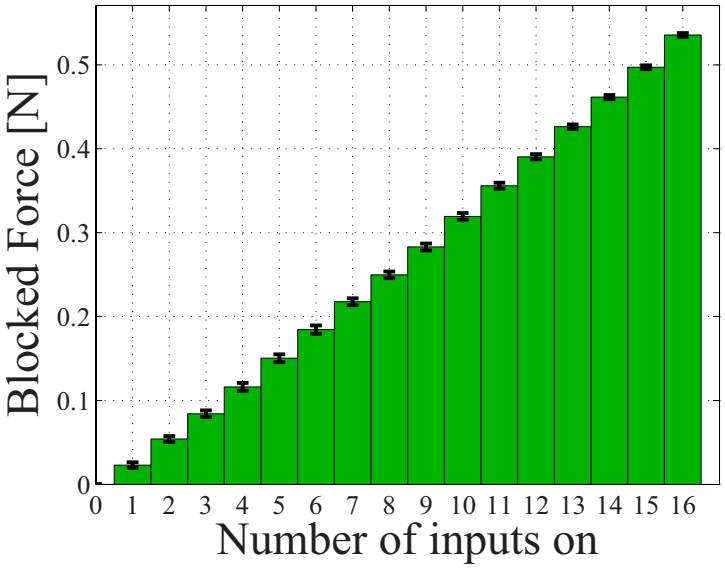

Figure 24: Blocked force measurements with activation. Error bars are 1 standard deviation.

each output flange is sensed by a Micro-epsilon optoNCDT laser positioning sensor with a range of 20 mm. The two measurements are summed to determine the free displacement. Results are shown in Figure 26.

As with the blocked force, the analytical model predicts a higher value than the experiment (8 mm). The repeatability is also very good. The linearity is good through activation of the first 8 units . Beyond this there is a visible reduction in the amount of displacement per unit activated. This is due to a saturation effect; as the actuator contracts, the angle in the deformed configuration approaches zero and the rhomboid approaches a rectangle. This effect is not captured by the linear model. Because this actuator is designed to be used in an antagonistic configuration, as described in section 4.5, its extension will only be in the first half of its range. For comparison, a trendline based on activation of the first 8 inputs has been added to Figure 26. The dashed portion shows the line extrapolated to show the "effective free displacement." In actuators designed to be used in a single-ended configuration, this saturation effect will be less pronounced.

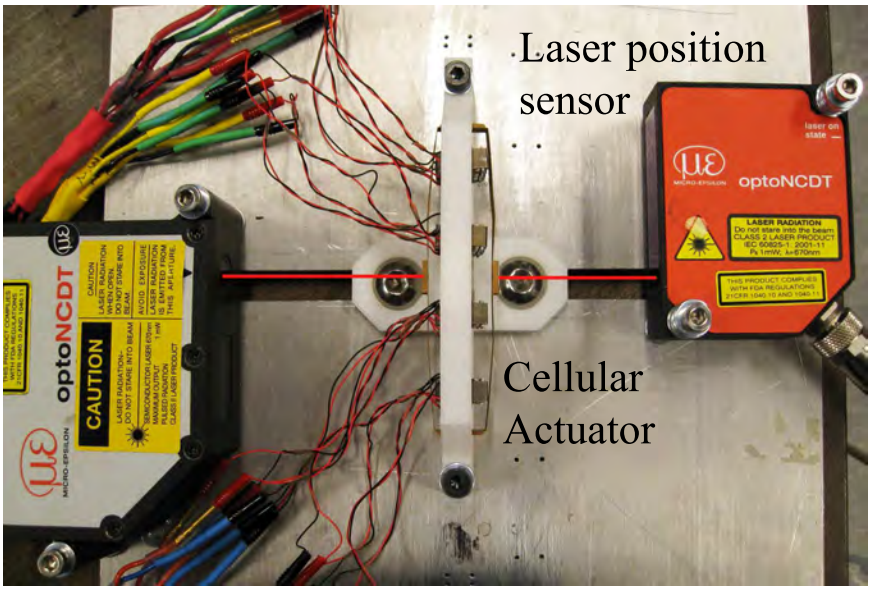

Figure 25: Free displacement experiment

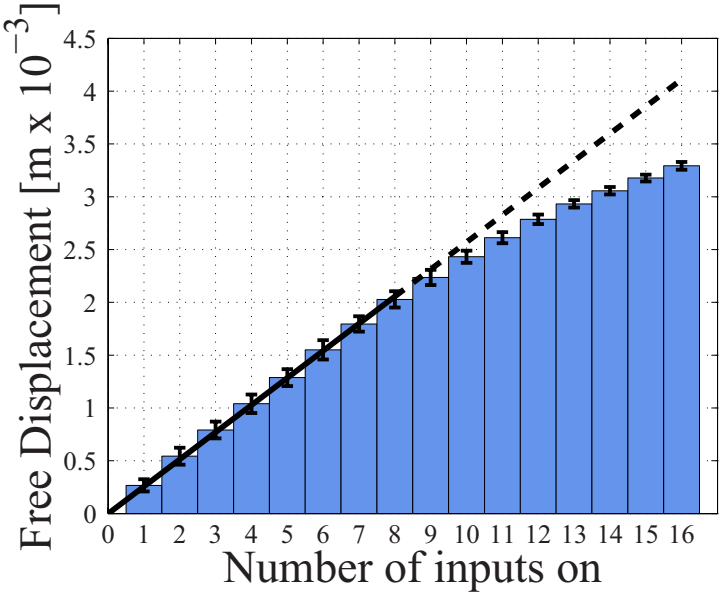

Figure 26: Free displacement measurements with activation. Error bars are 1 standard deviation.

4.10 Series combinations of internal subunits

At any given layer in the nested hierarchy, subunits at the prior layer are combined in series. This increases the displacement of the resulting actuator in two ways: first, the displacement of the subunits are additive, resulting in a larger input displacement to be amplified, second, the amplification mechanism has to be larger to accommodate the series combination of subunits at its input, resulting in a larger displacement at this output. The optimizations conducted in Chapter 5 will tend to produce an outermost amplifying mechanism that is as wide as possible in order get the largest displacement. This is intuitive, however, there is a need to estimate how much of an effect adding an additional subunit to a given series combination will have on the displacement and force capability of the subunit at the next layer in the hierarchy. It turns out that simply multiplying by the number of units present does not adequately describe the force-displacement relationship of series combinations in an internal layer, and by using the two-port model the effect of adding an additional subunit to the series combination can be evaluated.

This is illustrated in Figure 27. Figure 27a shows a strain amplifying mechanism whose input is the effort of 4 subunits in series. Figure 27b shows an equivalent mechanism, but with a single subunit and rigid spacers to transmit its action to the input of the mechanism. How much better is the actuator in Figure 27a than the one in Figure 27b in terms of displacement or force? Is there a point of diminishing returns when adding more subunits is only marginally helpful? The answer can be found using the two-port model.

Let the outermost amplifying layer be described by the two-port model of (15). The rigid portions do not contribute to the amplification, so the mechanisms of Figure 27a and Figure 27b will have the same two-port model. Each of the internal subunits will have a lumped stiffness k. Inactive units in the series combination will appear as passive springs of stiffness k.

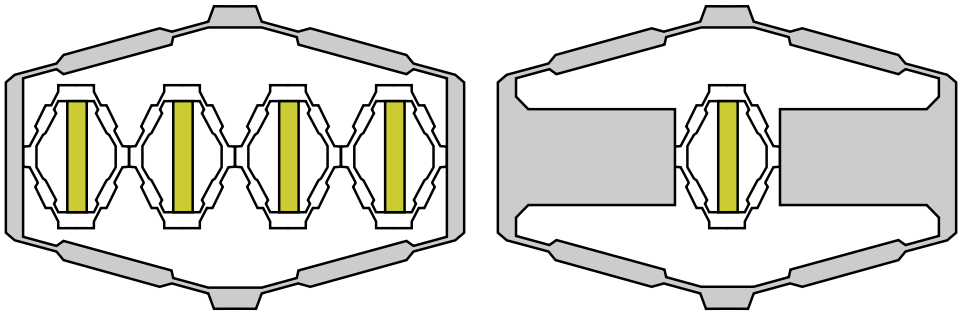

(a) Four subunits in series **(b)** Single subunit with rigid spacer

Figure 27: Comparison of an actuator with the same outer layer and different numbers of internal subunits

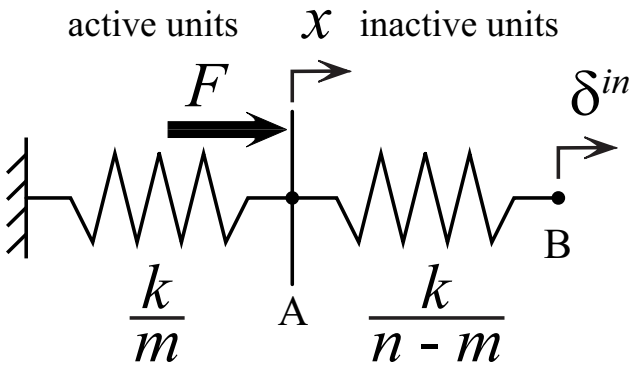

Figure 28: Active and inactive subunits represented as springs

The amplifying layer will have n subunits, of which m will be active. Without loss of generality, the active and inactive units can be represented as in Figure 28. The active units will displace by an amount x and impart a force F to the inactive units. The end of the series combination displaces by an amount δ^{in}, or the input displacement to the amplifying mechanism.

When a subunit is activated, its new resting length is δ_s^{free}, or the free displacement of that individual subunit. The force F can then be expressed as

$$F = \frac{k}{m}(m\delta_s^{free} - x). \tag{45}$$

applying equilibrium at point A and solving for x results in

$$x = \frac{m}{n}\left((n-m)\delta_s^{free} + \delta^{in}\right). \tag{46}$$

Substituting this into (45) yields

$$F = \frac{m}{n}k\delta_s^{free} - k\frac{\delta^{in}}{n} = \frac{m}{n}F_s^{block} - k\frac{\delta^{in}}{n}. \tag{47}$$

where F_s^{block} is the blocked force of a single subunit. Substituting into (15) and solving in the blocked and free cases gives

$$\delta^{free} = -\frac{m}{n}\frac{s_3 F_s^{block}}{s_3^2 - s_2(s_1 + k/n)} \tag{48}$$

$$F^{block} = \frac{m}{n}\frac{s_3 F_s^{block}}{s_1 + k/n}. \tag{49}$$

To compare the merits of a series combination of subunits, as in Figure 27a over that with just a single subunit, as in Figure 27b for a given amplification layer with immittances s_1, s_2, s_3, simply consider the ratio of the absolute value of expression (49) with an unspecified n to the absolute value of the same expression with n taken to be 1, and likewise for (48). This results in the following expressions:

$$R_\delta = \frac{m(\Delta + s_2 k)}{n\Delta + s_2 k} \tag{50}$$

$$R_F = \frac{m(s_1 + k)}{ns_1 + k}. \tag{51}$$

where $\Delta = s_1 s_2 - s_3^2$ is the determinant of the stiffness matrix. One useful metric is to find the minimum m for which both R_F and R_δ exceed 2. This is the number of units that need to be activated in order for the mechanism in Figure 27a to double the performance of that in 27b.

Full activation of all subunits means $m = n$. Looking at (51), when $k >> s_1$ (the amplifying structure is extremely compliant in the input direction when compared

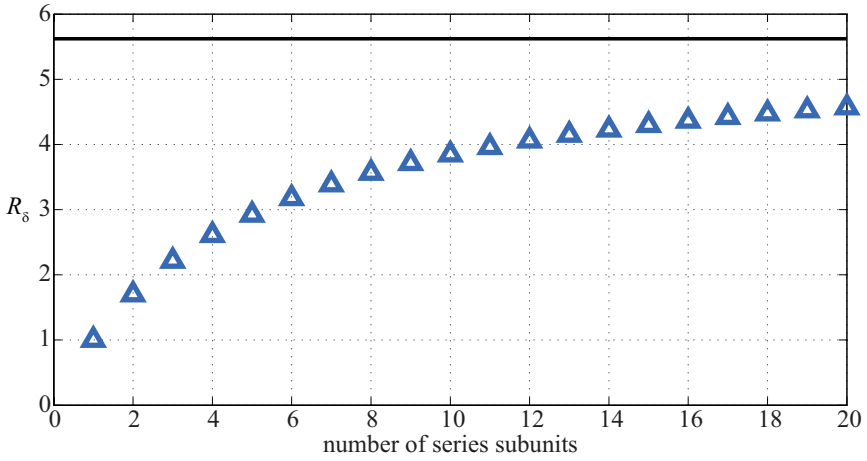

Figure 29: Free displacement ratio for series combinations of second layer subunits within the third layer amplifying mechanism. Black line is the theoretical upper limit.

to a subunit), R_F approaches n, or simple multiplication. This is an intuitive upper bound. It also means that the blocked force of the mechanism in Figure 27a will be less than 4 times that of Figure 27b. It also underscores the importance of the relative stiffnesses of various layers in the hierarchy. Looking at (50), it is clear that R_δ approaches n as Δ approaches 0. This describes the idealized or hinged mechanism described in [20]. It is clear than that the non-ideal nature of the flexural mechanism will cause the final displacement to be less than that predicted by simple multiplication.

As n becomes large, R_F approaches an upper bound of $1 + k/s_1$. Likewise, R_δ has an upper bound of $1 + s_2 k/\Delta$. Evaluating these simple metrics can be helpful to the designer when choosing how many subunits to put in series at a given layer in the hierarchy. Figures 29 and 30 show the progression of R_δ and R_F, respectively with increasing n at maximum activation.

4.11 Effectiveness of multiple layers and figures of merit

Nested mechanisms can produce more aggressive force-displacement tradeoffs than a single compliant mechanism, reaching larger stroke lengths without drastically increasing the resting length of the actuator. Each time a layer is added, some strain

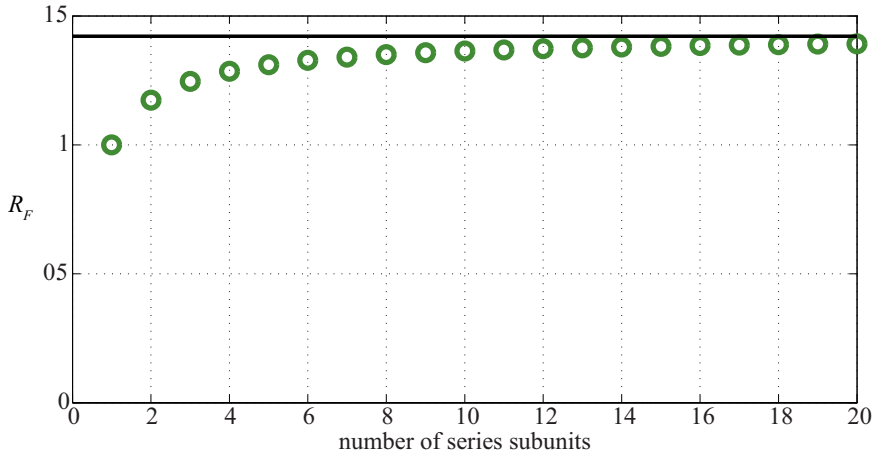

Figure 30: Blocked force ratio for series combinations of second layer subunits within the third layer amplifying mechanism. Black line is the theoretical upper limit.

energy is stored in the compliant mechanism, so unlike the idealized mechanism, the amplification effect is not simply multiplicative. The two-port network formalism allows one to analyze the effect of adding successive layers of strain amplification, determine if adding an additional layer is really a good idea, and estimate the point of diminishing returns.

4.11.1 Reuse of the same mechanism

Suppose that a rhomboidal compliant mechanism has been designed such that it amplifies the displacement of a piezoelectric stack while satisfying all manufacturing constraints. This "two-dimensional" mechanism is shown in Figure 31a. However, suppose also that this mechanism has a blocked force in excess of the requirements and does not meet the stroke length requirements. How much does the designer gain by reusing the same compliant mechanism to amplify the displacement still further, generating the "three dimensional" mechanism shown in Figure 31b?

(a) two dimensional mechanism **(b)** three dimensional mechanism

Figure 31: Multi-layer nested geometry with reuse of a compliant mechanism

4.11.1.1 Analysis of 3D nested structure with two identical compliant mechanisms

Suppose that the expressions for the immittance matrix have been determined for the compliant mechanism used in Figure 31a. The two-port force-displacement relationship can then be expressed as in (15), where s_1, s_2, and s_3 have units of stiffness, and each are expressions of the geometric parameterization and material properties.

In order to represent the cascaded connection of two strain amplification mechanisms, a different immittance matrix, the forward transmission matrix, is needed. This relationship expresses a different input-output choice for the same two-port network. Fortunately, the forward transmission matrix can be calculated directly following the procedure in [28] and is expressed as follows:

$$\begin{bmatrix} -\delta_{out} \\ F_{out} \end{bmatrix} = \frac{1}{s_3} \begin{bmatrix} s_1 & -1 \\ -\Delta & s_2 \end{bmatrix} \begin{bmatrix} \delta_{in} \\ F_{in} \end{bmatrix}, \tag{52}$$

where Δ represents the determinant of the stiffness matrix in (15). δ_{out} is negated to represent the change of direction of displacement with each added layer in the hierarchy. It is more advantageous to experimentally measure and tabulate the stiffness matrix in (15) than the forward transfer matrix because the stiffness matrix has consistent units among all the elements, whereas the forward transfer matrix does

not.

The forward transfer characteristic of the cascaded connection of two nested compliant mechanisms is simply the product of the two forward transfer matrices. Denoting the stiffness matrix elements for each layer with a leading superscript, beginning with the innermost, the combined forward transfer characteristic is as follows:

$$\begin{bmatrix} \delta_{out} \\ F_{out} \end{bmatrix} = \frac{1}{{}^1s_3^2 s_3} * \begin{bmatrix} {}^1s_1\ {}^2s_1 + {}^1\Delta & -{}^1s_2 - {}^2s_1 \\ -{}^2\Delta\ {}^1s_1 - {}^1\Delta\ {}^2s_2 & {}^2\Delta + {}^1s_2\ {}^2s_2 \end{bmatrix} \begin{bmatrix} \delta_{in} \\ F_{in} \end{bmatrix}, \tag{53}$$

the negative sign having canceled out due to the direction being reversed twice. If the two mechanisms are the same, as in Figure 31b, the leading superscripts become unnecessary, and (53) becomes

$$\begin{bmatrix} \delta_{out} \\ F_{out} \end{bmatrix} = \frac{1}{s_3^2} \begin{bmatrix} s_1^2 + \Delta & -s_1 - s_2 \\ -\Delta(s_1 + s_2) & \Delta + s_2^2 \end{bmatrix} \begin{bmatrix} \delta_{in} \\ F_{in} \end{bmatrix}. \tag{54}$$

4.11.1.2 Displacement amplification figure of merit

One important metric for strain amplified piezoelectric stacks is their *free displacement*, or the displacement of the output when no load is applied. This is synonymous with the maximum stroke length. One good dimensionless figure of merit that will tell whether it is advantageous to add another instance of a given mechanism to amplify the displacement still further is the ratio of the free displacement of the three dimensional mechanism in Figure 31b to that of the two dimensional mechanism in Figure 31a. From (15) and (54) it can be shown that

$$FOM = \frac{\mid \delta_{3D}^{free} \mid}{\mid \delta_{2D}^{free} \mid} = \frac{s_3}{s_1 + s_2} \tag{55}$$

If this figure of merit is greater than one, it is worth adding another instance of the compliant mechanism to amplify the displacement still further. However, since the stiffness matrix must be positive definite, this figure is upper bounded by $\frac{\sqrt{s_1 s_2}}{s_1 + s_2}$.

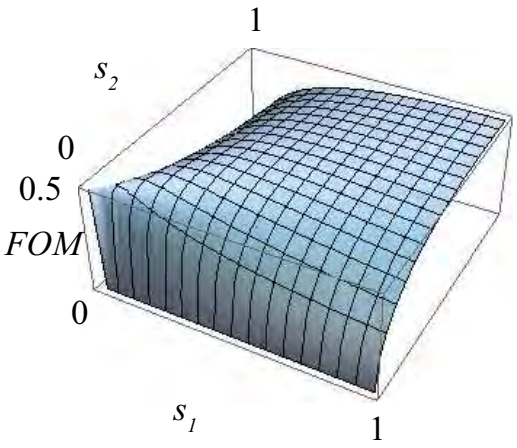

Figure 32: Bounding surface on figure of merit over s_1,s_2

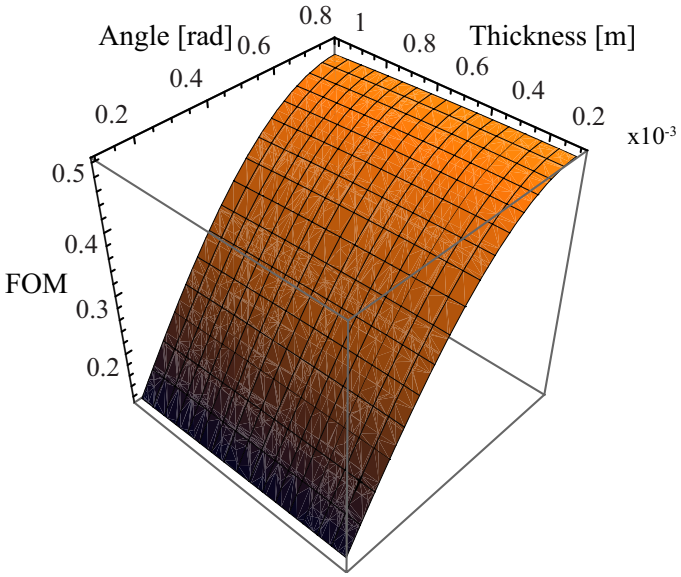

Figure 33: Variation in figure of merit with angle and thickness

Therefore, the figure of merit must lie below the surface shown in Figure 32. Using the analytical expressions for the two-port model of the mechanism, one can look at the figure of merit as it varies with *geometric* parameters. As an example, variation with thickness and angle are plotted in Figure 33 over a wide range of values. The maximum value is around 0.5. This suggests that there is nothing to be gained by adding another instance of a known compliant mechanism; the free displacement is actually lower!

This is not to suggest a figure of merit greater than one cannot be achieved

when the two layers are allowed to vary independently, in fact, previous work [1, 23, 25] indicates that this is possible. In each of these cases, the geometry of the outer layer is drastically different from the inner layer. The process for optimizing multi-layer mechanisms is quite involved and will be addressed in Chapter 5. This example shows how analytical expressions for the two-port immittance parameters from Chapter 3 combined with the results in this chapter allow for quick evaluation of nested topologies. In this way, one can determine whether there is a good range of geometric parameters for a given performance characteristic, something that is not easily done with purely numerical tools, such as finite element methods.

4.11.2 Mechanisms of different characteristic

The previous discussion shows that "re-using" a second instance of a strain amplifying mechanism in an attempt to amplify the displacement still further results in an actuator with a *smaller* displacement than the single-layer actuator. This is intuitive; if this method worked, roboticists could get unlimited displacement (albeit with a small force) from a single piezoelectric stack. It is clear then, that each subsequent layer added to the hierarchy must be more compliant than the prior layers in order to increase the amplification factor still further. This is the case in the two-layer mechanisms of [23, 25], [1].

Now consider augmenting an existing multi-layer amplified active material with one additional layer and compare the free displacement of the two mechanisms. δ_{aug}^{free} will denote the free displacement of the mechanism with the additional layer added to the hierarchy (or the augmented mechanism) and δ_{ext}^{free} will denote the free displacement of the mechanism without the additional layer (or the existing mechanism). Rewriting (55) with this new nomenclature, it becomes:

$$FOM = \frac{\mid \delta_{aug}^{free} \mid}{\mid \delta_{ext}^{free} \mid}. \tag{56}$$

In order for the additional layer to have some benefit, FOM must be greater than 1. The output characteristic of the two general mechanisms are as follows:

$$\begin{bmatrix} \delta_{ext}^{out} \\ F_{ext}^{out} \end{bmatrix} = \frac{1}{\prod_{k=1}^{n} {}^{k}s_3} \quad S_n \begin{bmatrix} \delta^{in} \\ F^{in} \end{bmatrix} \tag{57}$$

$$S_n = \begin{bmatrix} s_{11} & s_{12} \\ s_{21} & s_{22} \end{bmatrix} \tag{58}$$

$$\begin{bmatrix} \delta_{aug}^{out} \\ F_{aug}^{out} \end{bmatrix} = \begin{bmatrix} {}^{n+1}s_1 & -1 \\ -{}^{n+1}\Delta & {}^{n+1}s_2 \end{bmatrix} \begin{bmatrix} \delta_{ext}^{out} \\ F_{ext}^{out} \end{bmatrix} \tag{59}$$

where F^{in} and δ^{in} are the input force and displacement from the active material, F_{ext}^{out}, and F_{aug}^{out} are the forces at the output of the existing and augmented mechanisms, respectively, and δ_{ext}^{out} and δ_{aug}^{out} are the displacements of the existing and augmented mechanisms. S_n is the product of all the forward transmission matrices [28] (with $1/{}^{k}s_3$ pulled out front) of layers 1 through n in the existing mechanism. The matrix in (59) is the forward transmission matrix of the additional layer. ${}^{n+1}\Delta$ is the determinant of the stiffness matrix for the additional layer.

The free displacement expressions can be found by setting $F_{aug}^{out} = 0$ and $F_{ext}^{out} = 0$ in (57) and (59) and solving for δ_{ext}^{out} and δ_{aug}^{out}. Taking the ratio of the absolute values and simplifying, the FOM becomes:

$$FOM = \frac{{}^{n+1}s_3}{{}^{n+1}s_2} - {}^{n+1}\Delta \ \frac{s_{11}}{s_{21}}. \tag{60}$$

if the existing mechanism has a single layer, denoting the additional layer as layer 2, this becomes:

$$FOM = \frac{{}^{2}s_3}{{}^{2}s_2 + {}^{1}s_2 \ \frac{{}^{2}\Delta}{{}^{1}\Delta}}. \tag{61}$$

For any valid geometry ${}^{k}s_3$ is upper bounded by $\sqrt{{}^{k}s_1 \ {}^{k}s_2}$. Substituting this into (61) reveals that in order for FOM to be greater than 1, a necessary condition is:

$$\sqrt{\frac{{}^{2}s_2}{{}^{2}s_1}} + \frac{{}^{2}\Delta}{{}^{1}\Delta}\sqrt{\frac{{}^{1}s_1^2}{{}^{2}s_1^2 s_2}} < 1. \tag{62}$$

This expression has two terms, both of which must be less than one. This leads to several conclusions. The first term involves only the parameters of the additional layer. In order for the additional layer to be effective, it must have a much higher stiffness in the input direction than the output direction. The second term is more complicated, and involves both layers. This term will be small if ${}^{2}\Delta << {}^{1}\Delta$. For an idealized (hinged) mechanism, described in [1], ${}^{j}\Delta = 0$. This means that to contribute to the displacement, the outermost layer should be as close as possible to an idealized layer, whereas the inner layer should not look anything at all like all like the idealized mechanism. The second factor in the second term can be troublesome, since a large ${}^{1}s_1$ reduces the figure of merit. Since ${}^{1}s_2$ does not appear in the second factor of the second term, it to some degree can be used to increase the determinant. In reality, the immittances are coupled in the geometric parameters of a given layer, and cannot be set independently. The forgoing analysis shows that if a mechanism already exists with a good FOM, having a compliant outer layer and stiffer inner layers, it will be difficult to design an additional layer to amplify it further. However, it may be possible to start from scratch and design a new multi-layer mechanism with a larger free displacement that has more layers. This also underscores that the main purpose of multi-layer amplification mechanisms is to mitigate the effects of geometric constraints (such as the actuator's envelope) on the aggressiveness of the force-displacement tradeoff that prevent more aggressive trade-offs in a mechanism with fewer layers.

4.12 Summary

This chapter has discussed the method of "nesting" compliant strain amplification mechanisms to produce larger strain rates and displacements than single-stage amplification mechanisms. Nesting becomes necessary because geometric constraints on robotic devices often limit the amount of displacement amplification that can be produced by a single compliant mechanism. This chapter establishes a mathematical framework to understand and calculate the properties of the entire actuator when the properties of each stage in the hierarchy are known. Experimental results confirm the mathematical trends observed. It is shown that the stiffness perceived from the environment depends most strongly on the outermost layers in the hierarchy. For this reason, any design criteria related to stiffness will not constrain the design of the innermost layers.

This chapter has discussed the principles and metrics relevant to nested hierarchical strain amplification, and relevant mathematical features of the nested compliant mechanism architecture. With these properties of nested mechanisms in hand, Chapter 5 will show how a layered strain amplification mechanism can be selected to meet a design specification described in terms of these metrics.

CHAPTER V

A CAMERA POSITIONER DRIVEN BY MUSCLE-LIKE ACTUATION

This chapter will show how the two-port formalism for a rhomboidal strain amplifying mechanism can be put to use. The application is a biologically inspired camera positioning mechanism that orients a camera by means of an antagonist pair of contractile soft actuators containing a multi-stage hierarchical strain amplifier for piezoelectric stacks. Performance specifications for the camera positioning mechanism can be translated into performance specifications on the actuator itself.

The strain amplifier consists of several rhomboidal mechanisms, the output of each of which is the input to the next. Using the relationships derived in Chapter 3 and Chapter 4, various geometries or ranges of geometries can be quickly evaluated. Interplay between the various layers in the hierarchy is considered. Numerical, analytical, and geometric parameter studies are conducted, and optimization tools are used to identify a point in the parameter space that will give the camera a satisfactory range of operation. From there, the parameter space is explored further to identify a design with good overall performance.

5.1 Cellular actuators

Cellular actuators [1] consist of a number of lead zirconate titanate (PZT) ceramic stacks and deformable amplification mechanisms. When a voltage is applied to a piezoelectric material, it undergoes a mechanical strain, however, this strain is too small to be useful in robotic applications. The PZT stack applies a load to the amplification structure at the input, which due to the geometry of the mechanism results

in a larger displacement at the output. This technique has been used successfully for planar grippers [7]. Cellular actuators use a simple rhomboid geometry and are modular devices. The rhomboid has a major diagonal, aligned with the PZT stack actuation direction and a minor diagonal, aligned with the output direction. The result is a larger output displacement, but smaller output force. Compliant mechanisms such as rhomboidal strain amplifiers transmit an action from the input to the output, but also transmit an action from the output to the input. For this reason, they are modeled well by two-port network circuit models, which are described by

$$\begin{bmatrix} {}^{j}F^{in} \\ {}^{j}F^{out} \end{bmatrix} = \begin{bmatrix} {}^{j}s_1 & {}^{j}s_3 \\ {}^{j}s_3 & {}^{j}s_2 \end{bmatrix} \begin{bmatrix} {}^{j}\delta^{in} \\ {}^{j}\delta^{out} \end{bmatrix}, \tag{63}$$

where ${}^{j}F^{in}$,${}^{j}F^{out}$ is the force at the input and output respectively, ${}^{j}\delta^{in}$,${}^{j}\delta^{out}$ are the displacements at the input and output, respectively. ${}^{j}s_1$, ${}^{j}s_2$, and ${}^{j}s_3$ are functions of material and geometric properties, and the matrix in (63) is positive definite. As in Chapter 4, the leading superscript, j, denotes the rhomboid's position in the hierarchy, consisting of n "layers". In theory, a rhomboid can be designed to produce ${}^{j}s_1$, ${}^{j}s_2$, and ${}^{j}s_3$ that give any level of tradeoff desired, but certain factors limit this. These include internal interferences under deformation, manufacturing constraints, and buckling on thin sections. A solution is to use *successive layers of nested rhomboids* [1], each of which may include series-parallel combinations of subunits at lower levels of amplification. A schematic of this mechanism-within-a-mechanism design concept is shown in Figure 35. The PZT stacks themselves form the innermost layer (layer 0). Once a good overall force-displacement tradeoff is achieved, cellular actuators can be combined in series and parallel bundles in order to have the stroke and maximum force required for the task.

Although PZTs can be controlled proportionally by varying the voltage, they are subject to hysteresis and thus require complicated drive electronics. When many

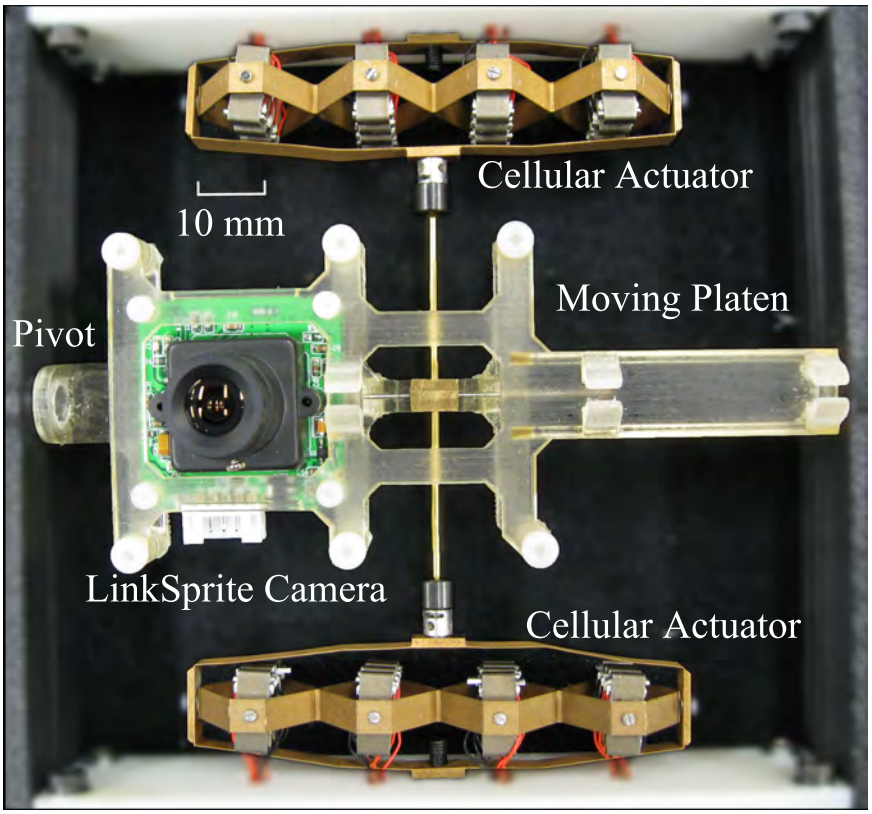

Figure 34: Single degree-of-freedom biologically inspired camera positioner

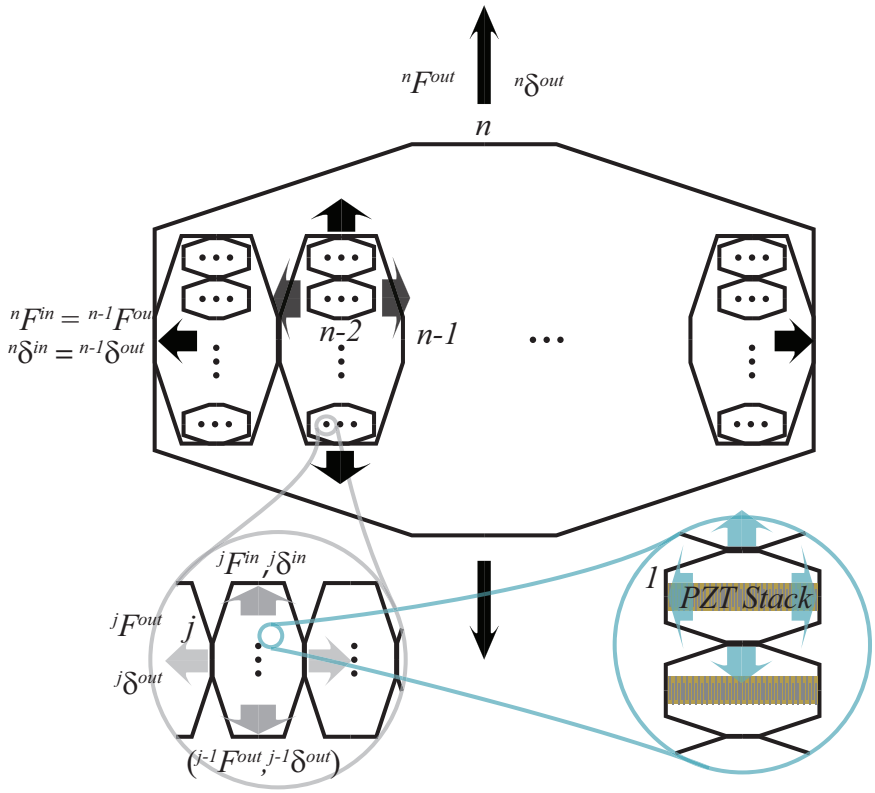

Figure 35: Hierarchical nested mechanisms

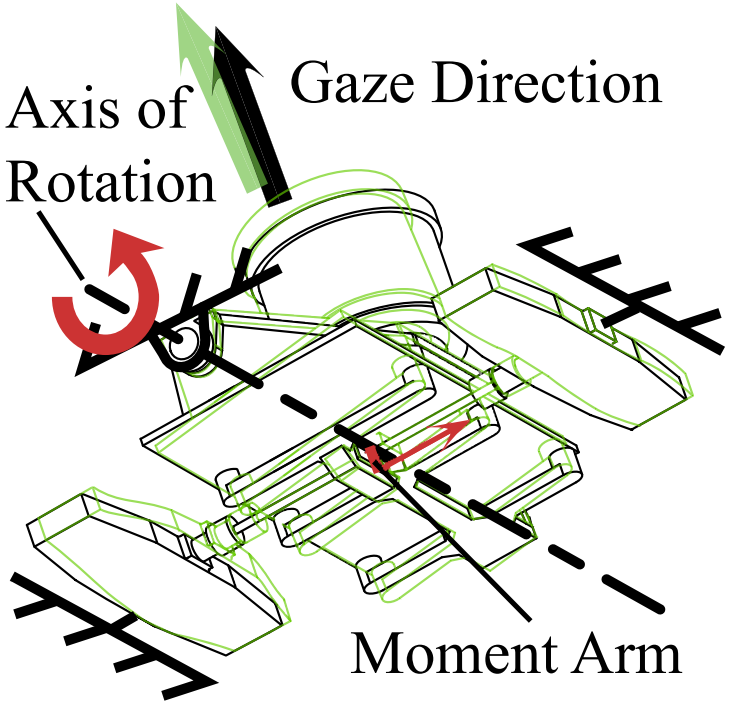

Figure 36: Positioner centered (black) and reoriented (green)

stacks are available, reasonable resolution can be obtained by operating each stack in an on-off manner and simply choosing how many stacks to activate, avoiding these issues. In this way, collections of cellular actuators or cellular actuators with several stacks per "cell" share principles in common with muscles; their action is a sum of the individual units recruited and their effects are linked by an elastic medium.

5.2 Single-degree-of-freedom device

Although it is hoped that the research in this thesis will eventually lead to a three-degree-of-freedom Listing-Donders compatible camera positioning mechanism, to accomplish the goals of this research, it is sufficient to build and test a single-degree-of-freedom-device, shown in Figure 34. This will allow verification of recruitment-based control algorithms and to review actuator performance independently of the kinematic and design challenges of a 3 degree of freedom device, which will require some sort of novel low-friction ball or gimbaled joint. The operation of the camera positioning device is illustrated in Figure 36.

The camera positioner supports a LinkSprite LS-Y201 camera. Since the goal is for the device to have performance similar to the human eye, it should have a working angle of $\pm 25^\circ$ (consistent with the linear region of human eye motion [50]). It should be capable of completing saccadic motions throughout its range within 50 ms [93]. The working range of the positioner is directly related to the actuator's free displacement (displacement of the actuator when no external force is applied). The saccade speed can be related to the actuator's blocked force (force applied by the actuator when no displacement occurs) and the inertia of the camera mechanism. With a moment arm of 5.84 mm, an antagonistic configuration, and adding a safety factor to avoid operating at the extremes of displacement (where the force capability is near zero), the desired free displacement comes out to be 8 mm.

Control and positioning is performed by a National Instruments NI cRIO-9024

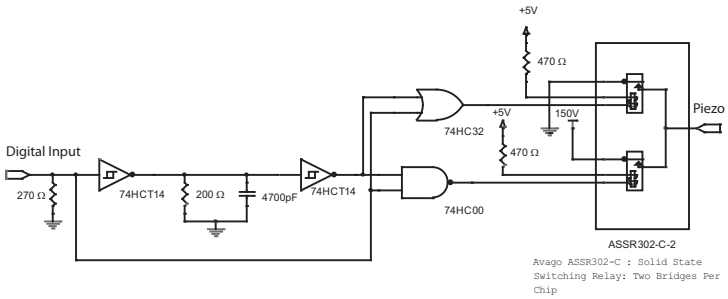

Figure 37: Discrete piezoelectric switching circuit with shoot-thru protection (single channel)

device, which includes an embedded processor and 40 MHz FPGA. Switching signals are generated by an NI 9401 module with a 100ns resolution. Because PZT requires a high drive voltage, switching signals from the NI 9401 are sent to a custom switching circuit that uses Avago ASSR302-C solid state switching ICs to connect each individual stack to 150V or ground. The circuit is equipped with an electronic delay to enforce a "break before make" condition on the switching IC to prevent damage. The switching delay is nominally 80 μs. A simple schematic for a single channel is shown in Figure 37. More detailed information is found in Appendix C. When the controller indicates that a given input should be recruited, the PZT stack will be connected to 150V. In order to release a given input, both ends of the PZT stack must be connected to ground so the charge stored can run into the ground plane. For this reason, simply disconnecting the PZT is not sufficient and both bridges of the ASSR302C must be used to control a single input. The circuit performs this operation automatically and requires only one signal line per PZT stack.

5.3 Actuator design

5.3.1 Amplified PZT base units

To ease the implementation of the control algorithms, it is advantageous to have a number of active units that is a power of two. In addition, a somewhat coarse quantization was desired in order to show the algorithm's effectiveness. So each

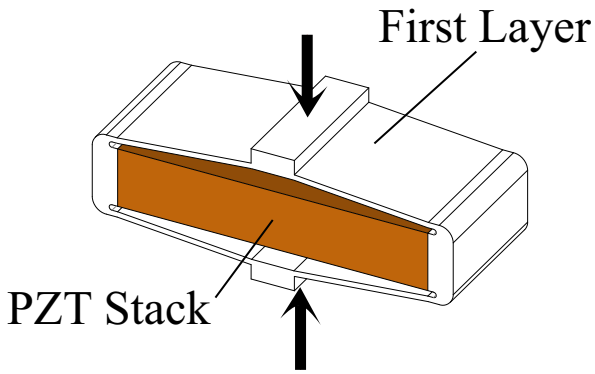

Figure 38: PZT stack with a single layer of amplification

actuator in the antagonistic pair contains 16 PZT stacks. This example seeks to determine the following:

- whether a nested compliant mechanism can be designed so that the action of 16 active units is sufficient to meet the desired free displacement
- if so, what blocked force can be achieved while also satisfying the desired free displacement

Because assembling the PZT stack into the innermost layer involves careful manufacturing techniques and closely held knowhow, the innermost layer consists of 16 amplified piezoelectric stacks from the Cédrat corporation, model APA50XS. The included rhomboidal amplification mechanism constitutes the first layer, i.e., the first layer amplification mechanism is pre-determined. A PZT stack with a single layer of amplification is shown in Figure 38. 16 of these units in series have a free displacement of 1.25 mm, which is well short of the desired value. So another layer of amplification is necessary. Keeping in mind the principles of Chapter 4, this section will search for a series of nested layers to produce the desired displacement.

5.3.2 Two layer actuator

To further increase the strain rate, Cédrat units can be placed inside another rhomboidal mechanism, resulting in the two-layer structure shown in Figure 39. This rhomboid will have parameters chosen for a good tradeoff. There are many possibilities for parameterization of a rhomboidal mechanism; this mechanism uses the set of parameters from the example in Chapter 3, shown again in Figure 40. When multiple layers are being considered, each parameter will be given a subscript to denote the layer to which it applies, with the largest number referring to the outermost layer. Using the methods of Chapter 3, it is possible to obtain the immittance matrix elements ${}^{j}s_1$,${}^{j}s_2$, and ${}^{j}s_3$ as expressions of these parameters. Once the immittance elements are determined, the free displacement and blocked force can be computed from (63) as:

$$ {}^{2}\delta^{free} = -\frac{{}^{2}s_3 \ {}^{1}F^{block}}{{}^{2}s_1 \ {}^{2}s_2 - {}^{2}s_3^2 + {}^{2}s_2 k_1} \tag{64} $$

$$ {}^{2}F^{block} = \frac{{}^{2}s_3^1 F^{block}}{{}^{2}s_1 + k_1}, \tag{65} $$

where ${}^{1}F^{block}$ is the blocked force and k_1 is the stiffness of the APA50XS units.

Using Wolfram Mathematica's `NMaximize[]` routine, the free displacement was maximized subject to manufacturing and physical constraints. From this, several things become evident: other than interior of the small surface shown in Figure 41, maximizing blocked force and free displacement seem to be competing goals, and free displacement falls off quickly with thickness, making it difficult to achieve a good tradeoff given manufacturing tolerances.

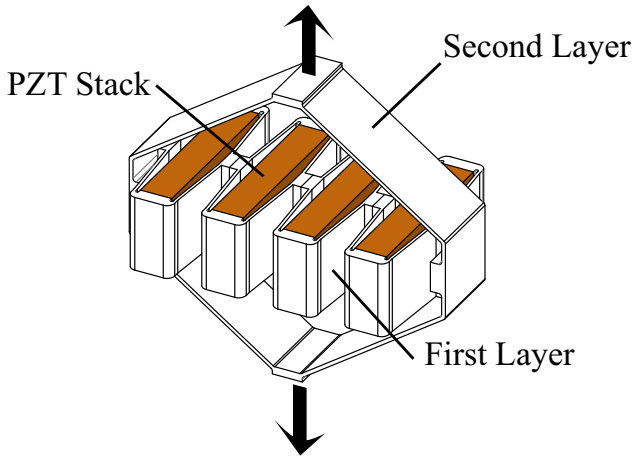

Figure 39: PZT stack with two layers of amplification

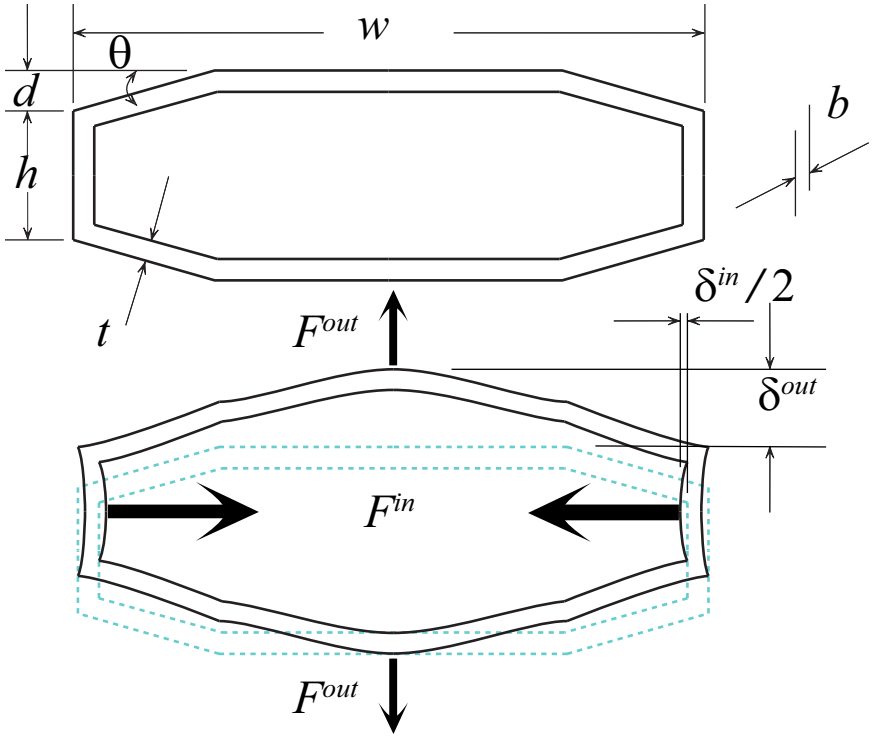

Figure 40: Parameterization of a rhomboidal mechanism

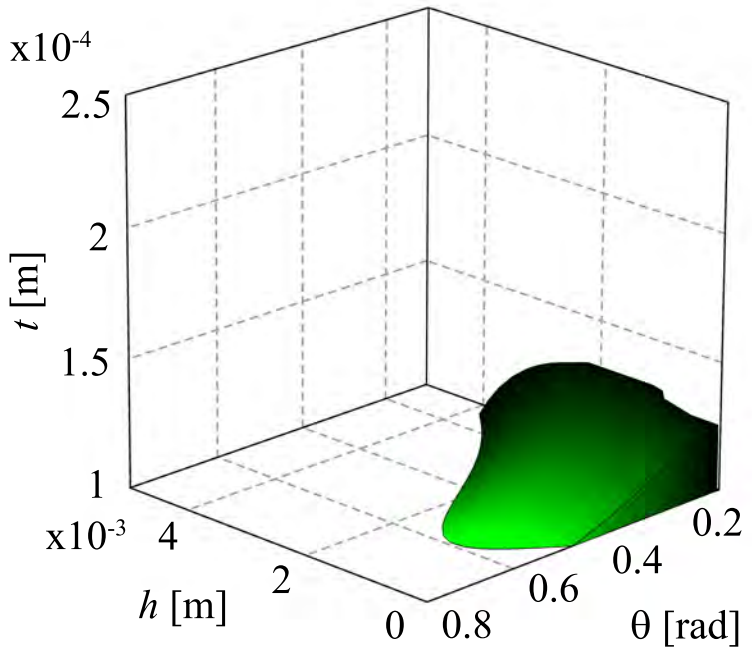

Figure 41: Region in θ, h, t space where both good force and displacement properties can be achieved. Plot shown for 4 two-layer units in series with 4 Cédrat APA50XS units each. d is fixed at 1 mm. Displacement threshold is 4 mm total, force threshold is 0.5 N. Notice that the displacement threshold is only half of that required; the specification is not met by this configuration.

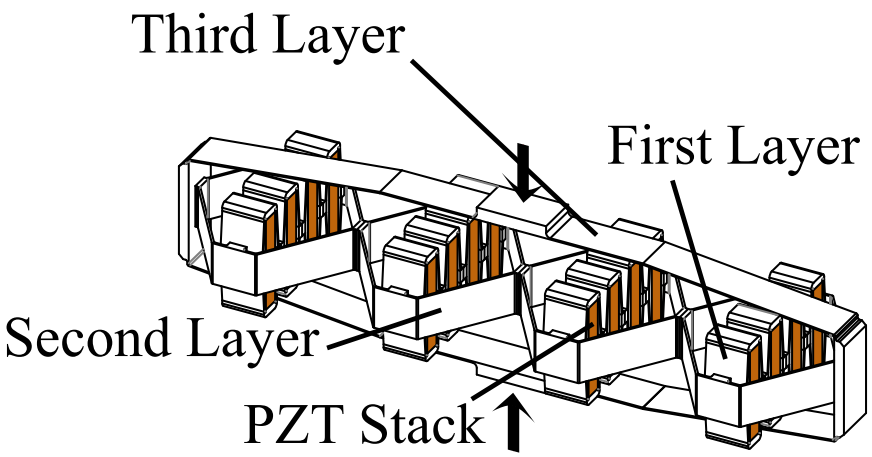

Figure 42: PZT stack with three layers of amplification

5.3.3 Three layer mechanism

Chapter 3 showed that for a given rhomboidal mechanism, the immittance matrix elements ${}^{j}s_1$, ${}^{j}s_2$, and ${}^{j}s_3$ are coupled, being analytical expressions of the same geometric parameters. This makes it difficult to achieve a favorable tradeoff between blocked force and free displacement by modifying a single layer. Optimization of a weighted function of force and displacement tend to return results that favor only one, with the other quantity being unsuitable. One might speculate that better tradeoffs can be achieved by exploiting the interplay between various layers, since the immittance matrices of each layer are largely decoupled from one another. In addition, rhomboidal mechanisms alternate between contractile and extensile outputs with each added layer, and a two-layer mechanism happens to be extensile. This can be overcome by using a concave "bow-tie" shaped mechanism [22, 23] but this topology may interfere with device being driven, and is not very compact. Since a goal of this research is to create actuation that is similar to human muscle, a compact, contractile mechanism is necessary. The remainder of this chapter therefore explores the three-layer mechanism shown in Figure 42, performing selection of the second and third layer rhomboidal geometry. The third layer uses the same parameterization as the second layer.

The impedance of each layer affects the performance of the others; optimization of each of the layers cannot be conducted separately. The optimization problem for the three-layer actuator has 9 parameters, resulting in much greater complexity. The general idea is to search the level surface corresponding to the desired free displacement for the maximum blocked force on the surface. Wolfram Mathematica's `NMaximize[]` routine is unable to solve this problem directly with 9 parameters, so it proved necessary to break the search into steps, "guiding" the optimization routines to find an acceptable solution. This solution may not be globally optimal.

The first step maximized the lumped stiffness, or stiffness viewed from the output, of the two-layer unit, independently of the third layer. Then the third layer parameters were varied with the second layer geometry held fixed, maximizing free displacement. The resulting geometry serves as the initial condition to an unconstrained maximization on the free displacement. This resulted in a maximum free displacement of 12.9 mm, exceeding the specification.

The next step is to increase the blocked force. The natural procedure to arrive at a final design is to modify the geometry in the neighborhood of the maximum displacement and maximize the blocked force subject to the constraint that the free displacement be greater than 8 mm, possibly by constraint deletion since the free displacement constraint is a complicated function. While appealing, the numerical realities of the problem rendered it unsolvable using Wolfram Mathematica's optimization routines. Therefore, the geometry selection proceeded by using a graphical search for a solution, varying two or three of the most significant parameters at a time.

5.3.4 Design constraints

There are a number of constraints on the geometry imposed when optimizing a rhomboidal strain amplifying mechanism. The ones applicable to this case are summarized

here; analogous constraints in the general case should follow logically from this example.

- Each rhomboid will be machined by wire EDM techniques, for which the minimum thickness t is 0.1 mm.

- The length of the angled section along the actuation direction d must exceed the desired displacement of the amplification stage. Otherwise the rhomboid will fold up into a rectangle and the two-port model no longer applies. In this case the minimum d_3 was 2.4 mm.

- Although it is theoretically possible to have very small angles, there must still be a discernible angle when manufacturing tolerances, assembly misalignments, deformations during motion, and preloads are applied. In this case the angle of all stages was limited to $6^\circ < \theta < 45^\circ$.

- The length of each layer in the output direction must match the length of the subsequent layer in the input direction. This was relaxed slightly between the second and third layers, allowing for a rigid "spacer" no longer than 5 mm on each side. Thus, w_3 was allowed to vary in a 10mm range.

- Each rhomboid must have its major axis along the input direction, i.e., $2d + h < w$.

- d, θ, and w must be chosen so that the geometry results in a simple convex polygon; anything else is considered a degenerate geometry and is not included.

In addition, the actuator must not impinge on itself when activated. For this reason, a rigid section was added to the middle of the third layer to make room for the first layer units.

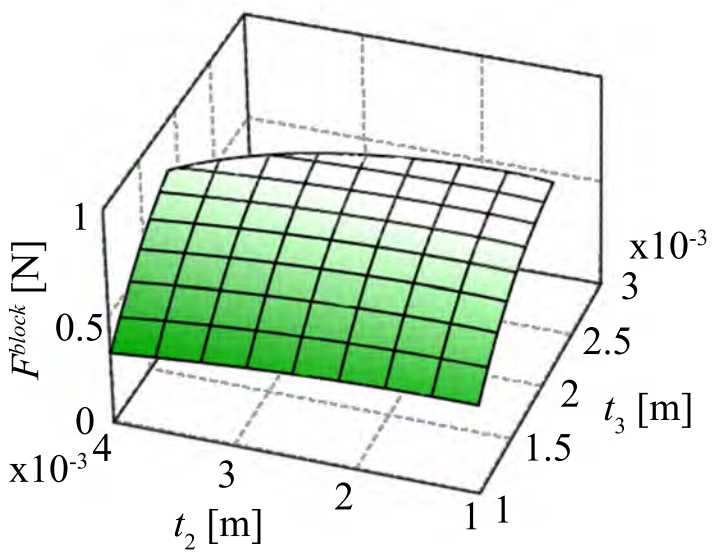

Figure 43: Variation in (simulated) blocked force with t_3,t_2

5.4 Results

It turns out that the thickness of the outermost layer t_3 has the greatest effect on the free displacement/blocked force tradeoff, and high displacement actuators tend to have low t_3, θ_3 and d_3 values, with high w_3. These results are intuitive and follow from the results in Chapter 4. A plot of blocked force vs. t_3 and t_2 is shown in Figure 43. The surface is only plotted over regions that produce sufficient free displacement. This shows that the blocked force is greatest along the level surfaces where the displacement spec is just met.

The second layer parameter, t_2, affects the shape of this level surface, and the other second layer parameters do likewise. As can be seen in Figure 44, the free displacement level surface is curved in h_2-θ_2 space, meaning that there is an internal point that represents the best force in this region. A correct second layer impedance is important to the design.

By plotting these surfaces for several t_2, eventually the design summarized in

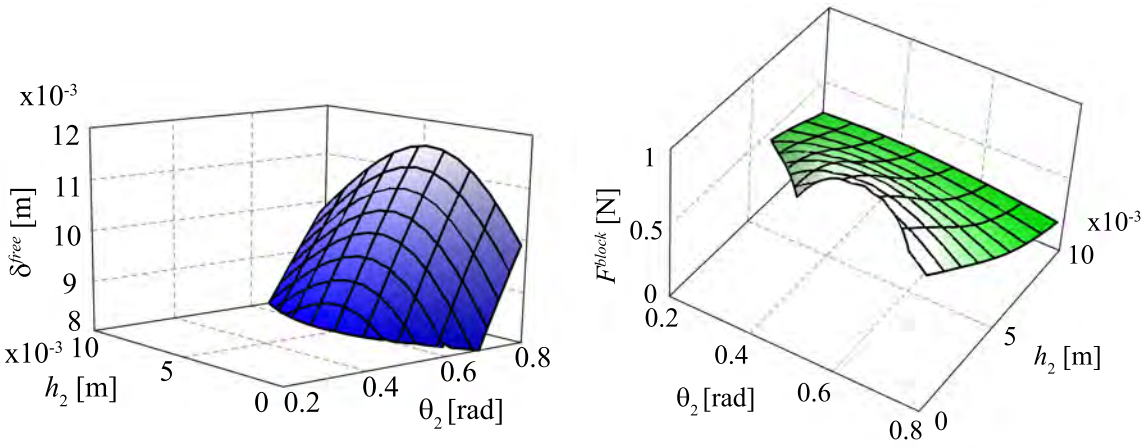

(a) Allowable Free Displacement **(b)** Blocked Force

Figure 44: Variation in (simulated) performance with h_2,θ_2

Table 9: Final design of three-layer actuator

Quantity	Value	Units
d_3	2.40	mm
h_3	1.00	mm
θ_3	6	°
t_3	0.170	mm
w_3	68.8	mm
d_2	6.60	mm
h_2	3.00	mm
θ_2	35.1	°
t_2	0.250	mm
${}^3F^{block}$	0.907	N
${}^3\delta^{free}$	8.10	mm

Table 9 was selected. The resulting three layer actuator design has a free displacement of 8.1 mm and a blocked force of 0.907 N. By way of comparison, the Cédrat APA1000XL, the largest in their amplified piezoelectric stack actuator series, has a free displacement of 1.05 mm and has a footprint nearly 7.5 times larger than the three-layer actuator presented here. The APA100XL, like the other offerings from Cédrat, has only a single stage amplification mechanism.

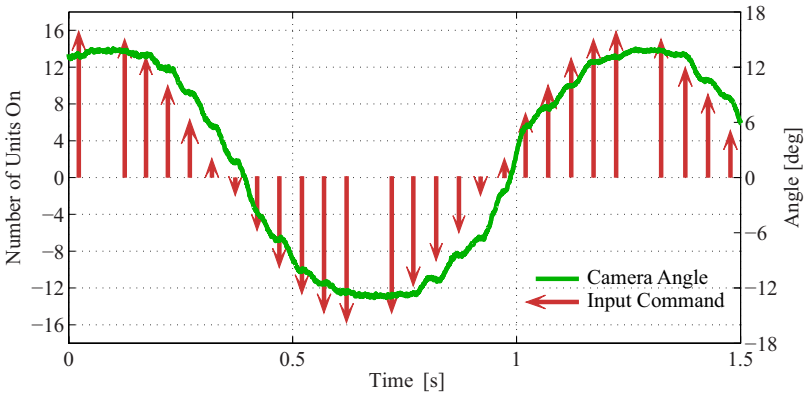

(a) Open loop trajectory

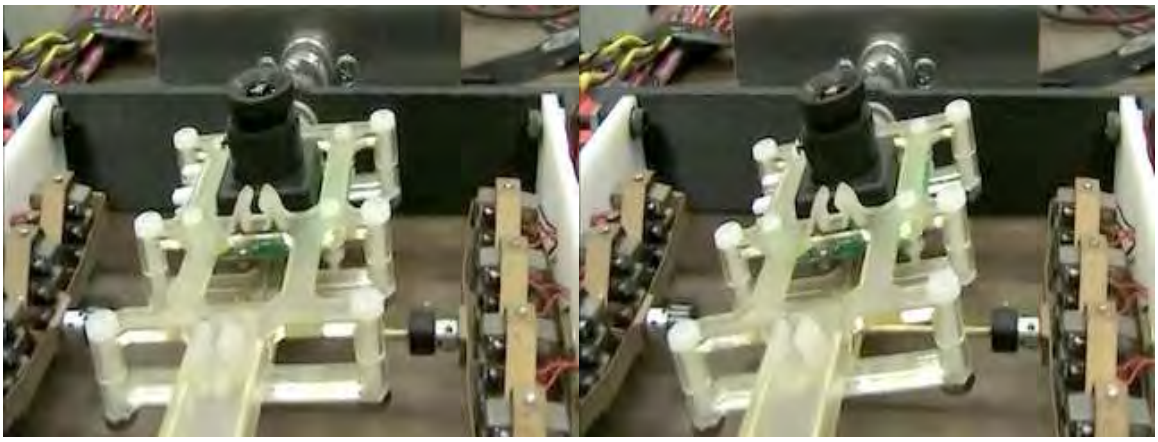

(b) Position I **(c)** Position II

Figure 45: Motion of the camera positioner

5.5 Positioner motion

Two instances of the piezoelectric cellular actuator designed in section 5.3 are placed in an antagonistic pair arrangement. Figure 45 shows the response of the camera to a quantized sinusoid with an amplitude of 16 units active (maximum activation). Figure 46 shows the image capture from the camera at the center and extremes of motion. It is theoretically possible to reach arbitrary positions for some finite length of time using discretized control efforts. This will be discussed in Chapter 8.

Theoretically, each actuator should move 4 mm (half of its free displacement) at maximum activation, exceeding the required angle of 25 degrees. Parasitic effects such as misalignments, residual stresses from manufacturing and assembly, and bearing

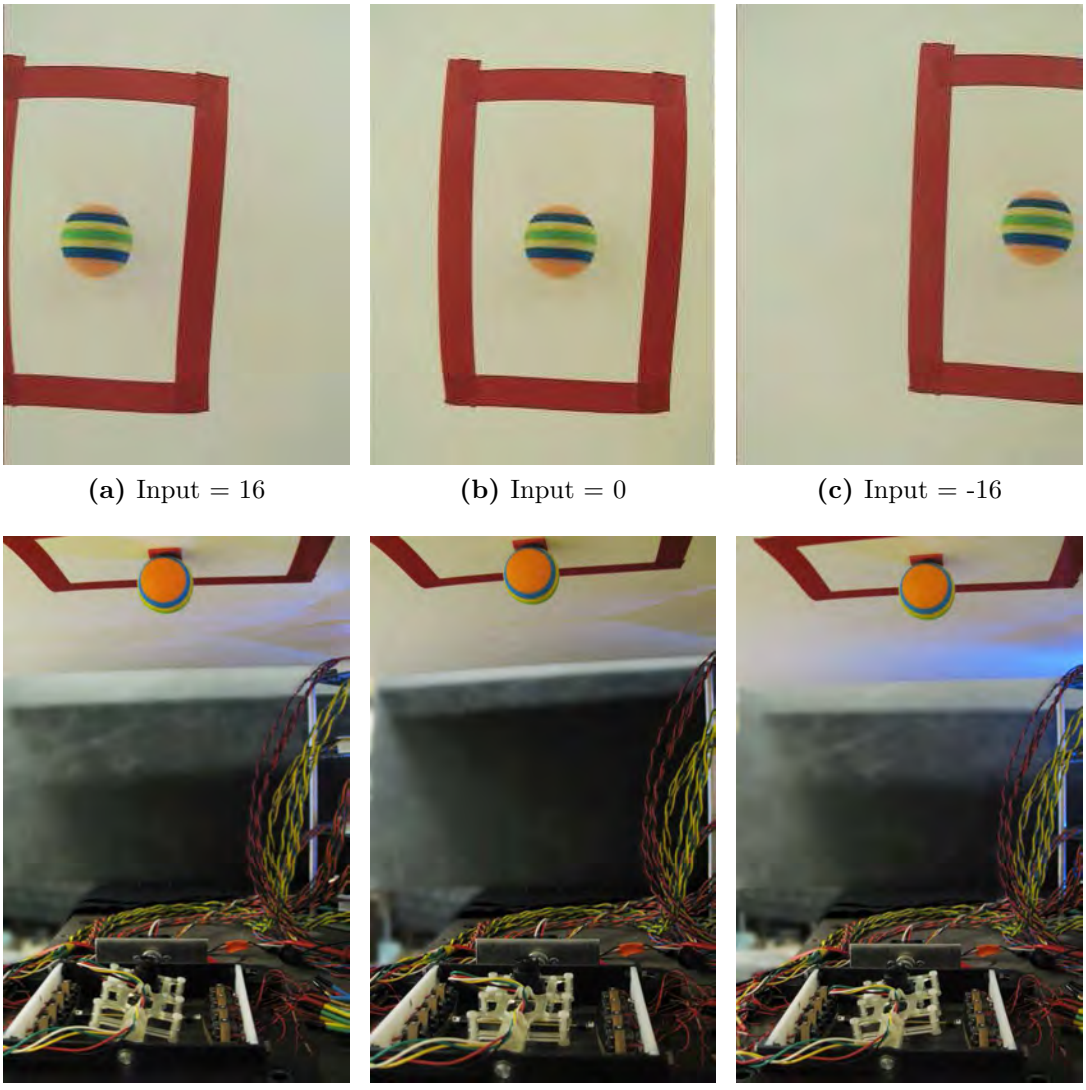

(a) Input = 16 **(b)** Input = 0 **(c)** Input = -16

(d) Input = 16 **(e)** Input = 0 **(f)** Input = -16

Figure 46: Camera images from full activation to the left, zero activation, and full activation to the right. The antagonist actuator is not activated. The object is roughly 200 mm from the camera imaging sensor. Photos 46d-46f taken by William Gallagher.

friction limit this somewhat, so the displacement of this first prototype is less than that predicted by the theoretical model.

5.6 Summary

This chapter presents an analysis of the force-displacement tradeoffs involved in the actuator design and shows how to find geometry that meets the requirements of a camera positioner. Actuator performance is demonstrated on a single degree-of-freedom device. It is compact enough to be used in autonomous robot navigation, indoor security, and humanoid applications. The cellular actuator, a biologically inspired actuation technology that uses a multi-stage hierarchical compliant mechanism to scale up the displacement of piezoelectric ceramic stacks, holds great potential to more accurately replicate human eye motion than do traditional actuators. This chapter shows that by exploiting the principles revealed in Chapters 3 and 4, compact, large-strain actuators can be achieved. Chapters 6, 7 and 8 will discuss open and closed loop control algorithms compatible with the discretized nature of these actuators.

CHAPTER VI

MINIMUM SWITCHING DISCRETE SWITCHING VIBRATION SUPPRESSION ON A 6 INPUT, TWO-LAYER CELLULAR ACTUATOR

The actuators developed in chapter 5 and [1] each contain several piezoelectric stacks that can be activated independently. In order to avoid hysteresis and to simplify the drive electronics, it is advantageous to make each of these inputs on-off only. The compliant nature of the strain amplifying mechanisms developed in chapters 3 and 5 and the impulsive nature of the these on-off inputs can lead to oscillatory behavior. In this way, these actuators bear similarity to human muscle, where efforts of on-off muscle fibers are linked by compliant tissue.

This chapter presents a control method whereby the activation timings of these discrete-valued inputs can be carefully coordinated to suppress multiple modes of vibration. This method is demonstrated on a replica of the actuator used in [1]. The dynamic response of the actuator is determined experimentally and reveals two significant lightly damped modes of vibration.

6.1 All On/All Off Control

Each time an actuator changes from one state to another (forward, off, reverse) its effort is associated with an impulse. Each impulse is represented by a phasor in the complex plane. The direction of the phasor, ϕ_j, is the angle corresponding to the time delay from the initial impulse, t_j, with respect to the natural period of the mode of vibration, T_n, (angular frequency ω_n) being considered.

$$\phi_j = 2\pi \frac{t_j}{T_n} = \omega_n t_j \tag{66}$$

If the vector sum of these impulses is zero, there will be no residual oscillation at frequency ω_n after the command is completed. Inputs to the cellular actuator have only two states, on and off. Although each input can be independently commanded, the switching method of Singhose, Singer, and Seering [64] can be applied by "linking" inputs and applying the same command identically to all inputs. For example, if activating 3 units will reach the desired steady state position, but a step command is oscillatory, an on-off switching vibration suppression command can be identically applied to 3 inputs, with the remainder inactive, to reach the goal without oscillation. The vibration suppression command is computed as if the device had only a single switching input. This will be referred to in this chapter as *All On/All Off control*.

6.2 Discrete Switching Vibration Suppression

Typically, in systems with on-off actuators, the input has a fixed amplitude. Although Singhose, Seering and Singer [64] make provision for impulse amplitudes that take different values, in their work, the variation in amplitude is used mainly to account for reduction in oscillation over time due to damping effects, undamped amplitudes being normalized to one. It is not set up for a highly discretized input, such as redundant array of cellular actuators. If a degree of freedom is actuated by an array of actuators, all of which produce the same amount of generalized force, the control input $u(t)$ at any time can be defined to be

$$u(t) = \sum_{j=0}^{m-1} A_j \delta(t_j), A_j \in \mathbf{D} \subset \mathbb{Z}, 0 \notin \mathbf{D} \tag{67}$$

where A_j is some integer impulse amplitude, m is the total number of impulses, and $\delta(t_j)$ is the Dirac delta function. Each A_j is normalized with respect to the generalized force provided by a single actuator, which is assumed to have the same magnitude in

either direction. Since applying an impulse j at some time corresponds to turning a certain number of actuators on or off, it is limited by practical considerations, namely, how many actuators are, at a given time, in the "on" state and therefore available to be turned off, and how many actuators are in the "off" state and are available to be turned on. Thus, the set of possible input amplitudes, $\mathbf{D}$, will change each time an impulse is applied.

The vibration due to impulse A_j can be represented as a multiplicity of phasors in the complex plane, each rotating at a natural frequency of vibration. It is assumed that any amplitude reduction due to damping is negligible on the time scale of interest. If damping is significant, appropriate scaling of the impulse amplitudes with time can be incorporated.

Because the impulse amplitudes must take integer values, it is assumed that a set of amplitude values are known *a priori*, and that the times at which they are applied, which can vary continuously, are the unknowns. All timings can be expressed as a phase ϕ_j with respect to the lowest natural frequency of the system. In order to suppress vibration at all natural frequencies, the real and imaginary components of the residual oscillation at all natural frequencies must be zero. This condition can be derived from the vector diagram and amounts to solving the system below:

$$
\begin{aligned}
A_0 + A_1 \cos\phi_1 + \cdots + A_{m-1} \cos\phi_{m-1} &= 0 \\
A_1 \sin\phi_1 + \ldots + A_{m-1} \sin\phi_{m-1} &= 0 \\
A_0 + A_1 \cos\frac{f_2}{f_1}\phi_1 + \cdots + A_{m-1} \cos\frac{f_2}{f_1}\phi_{m-1} &= 0 \\
A_1 \sin\frac{f_2}{f_1}\phi_1 + \cdots + A_{m-1} \sin\frac{f_2}{f_1}\phi_{m-1} &= 0 \\
&\vdots \\
A_0 + A_1 \cos\frac{f_n}{f_1}\phi_1 + \cdots + A_{m-1} \cos\frac{f_n}{f_1}\phi_{m-1} &= 0 \\
A_1 \sin\frac{f_n}{f_1}\phi_1 + \cdots + A_{m-1} \sin\frac{f_n}{f_1}\phi_{m-1} &= 0
\end{aligned}
\tag{68}
$$

where f_i is the natural frequency of the ith mode and there are n significant modes. Since (68) contains two equations for every frequency to be suppressed, due to the real and imaginary parts, the command must contain 2 impulses occurring at some phase ϕ per frequency to satisfy the constraints.

Activating any single input in the array, while leaving the remaining inputs off, will result in a steady state displacement. This displacement will be the same (to within the accuracy measured in Chapter 4) regardless of which input is activated. Therefore the steady state displacement due to any combination of inputs can be normalized by this value. The desired steady state displacement can then be expressed as an integer goal displacement y_g, which corresponds to the total number of inputs turned on. This adds an additional constraint that must be satisfied:

$$
\sum_{j=0}^{m-1} A_j = y_g \tag{69}
$$

There may be many choices of A_j for which a set of ϕ_j exists that can achieve the goal displacement and suppress vibration at the frequencies considered. There are a number of advantages to choosing the *minimum switching condition*, or

$$\{A_j \in \mathbf{D} \subset \mathbb{Z}\} \text{ such that } \sum_{j}^{m-1} |A_j| \text{ is minimized} \tag{70}$$

6.3 Redundantly actuated flexible cellular actuator

When a device has multiple actuators for a single degree of freedom, this thesis will use the term "redundant actuation" to describe this scenario. The cellular actuator shown in Figure 47 is one such device. It is constructed from commercially available strain-amplified [18] [94] [1] lead zirconate titanate (PZT) piezoelectric stack actuators from the CEDRAT corporation, model APA50XS. These have a maximum no load displacement of 80 μm [9]. This collection will be referred to as the "first layer." Because each of the first layer subunits has such a small displacement, 6 of them are stacked in series so that the first layer output displacement is the sum of the 6 actuators. This strain is amplified by the "second layer," a rhomboidal high silicon bronze strain amplifier that surrounds the first layer. If a (non-square) rhombus has some small strain along its major diagonal, ε_0, the minor diagonal will experience a larger strain, $\varepsilon_1 = \alpha_1 \varepsilon_0$ where $\alpha_1 > 1$ [94] [1]. The first layer units in series actuate along the major diagonal of the rhomboidal second layer. Figure 48 illustrates this amplification concept. The second layer was designed to achieve 20% strain. The design process to achieve this displacement (along the minor diagonal) is described in detail in [1]. Cellular actuators can be cascaded to form robotic devices, as described in [22].

Because each first layer unit actuates in the same direction and has the same function, the numerous first layer units represent redundant actuation. This type of actuator is equipped with redundancy deliberately because several first layer units are necessary to achieve the desired stroke. Human muscle also possesses redundant actuation to increase stroke length and force. Any given muscle group will have many muscle fibers, each with many sarcomeres. Redundant actuation may also be present

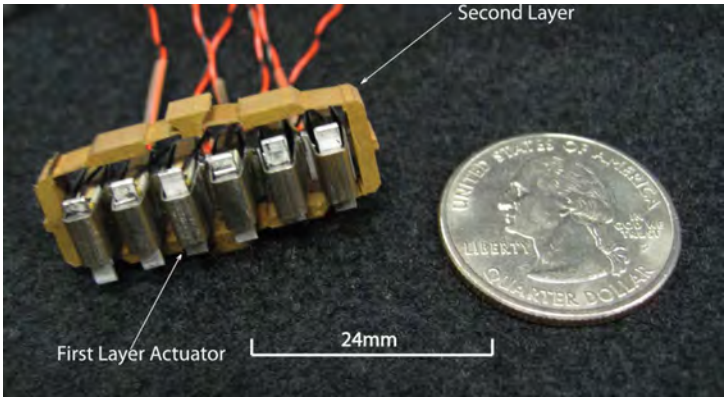

Figure 47: Two-layer cellular actuator

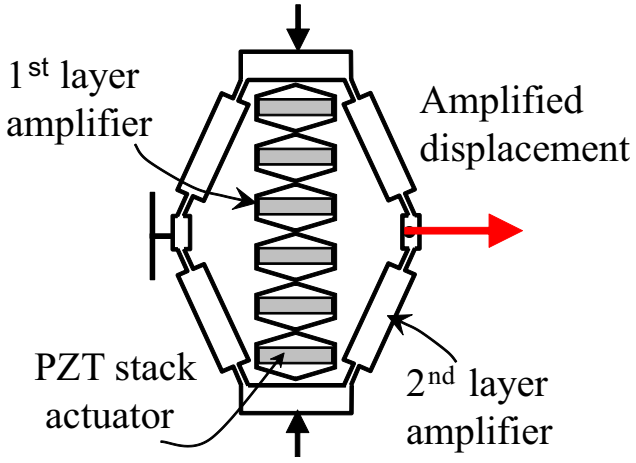

Figure 48: Cellular actuator schematic [95]

in traditional automation to insure the device can continue functioning if a single actuator fails.

This redundancy of actuation can be exploited to impose additional constraints on the system while achieving the desired control objective, e.g., position, force. Most notably, the redundancy of actuation can be used to limit vibration in the resonant modes of the actuator. Although the individual piezoelectric stacks are capable of receiving an analog command, it is desirable to restrict the command to each first layer actuator to be simply "on" or "off." The piezoelectric stacks possess hysteresis, which is problematic for positioning applications. On-off commands mitigate the hysteresis effect because the PZT stack only operates at the ends of the hysteresis loop [2]. Analog commands require transistors to operate in the linear region, which complicates the drive electronics and causes more heat to be dissipated, requiring larger transistor spacing and increasing package size. Restricting the control input to switching commands simplifies the firmware. This quantization limits the position resolution, but when many actuators are combined in series-parallel combinations, the position is indistinguishable from that of a continuously variable analog command.

The cellular actuator has two significant modes ($n = 2$) that need to be suppressed. Because one end of the cellular actuator is fixed to a rigid support, the other end will have a finite relative displacement as the actuator extends. The goal displacement is normalized and can take any natural number from 0 to 6. In order for (68) and (69) to be satisfied, there must be a total of $m = 2n + 1 = 5$ impulses. $m > 5$ can be chosen if some strategy is chosen for determining a solution for an underconstrained system of equations, however, the additional impulses reduce the likelihood of reaching a minimum switching solution. Since the first impulse occurs at $t = 0$, the phases ϕ_j of the remaining four impulses must be found. Because the number of first layer units on cannot exceed six, the amplitudes A_j must be chosen such that

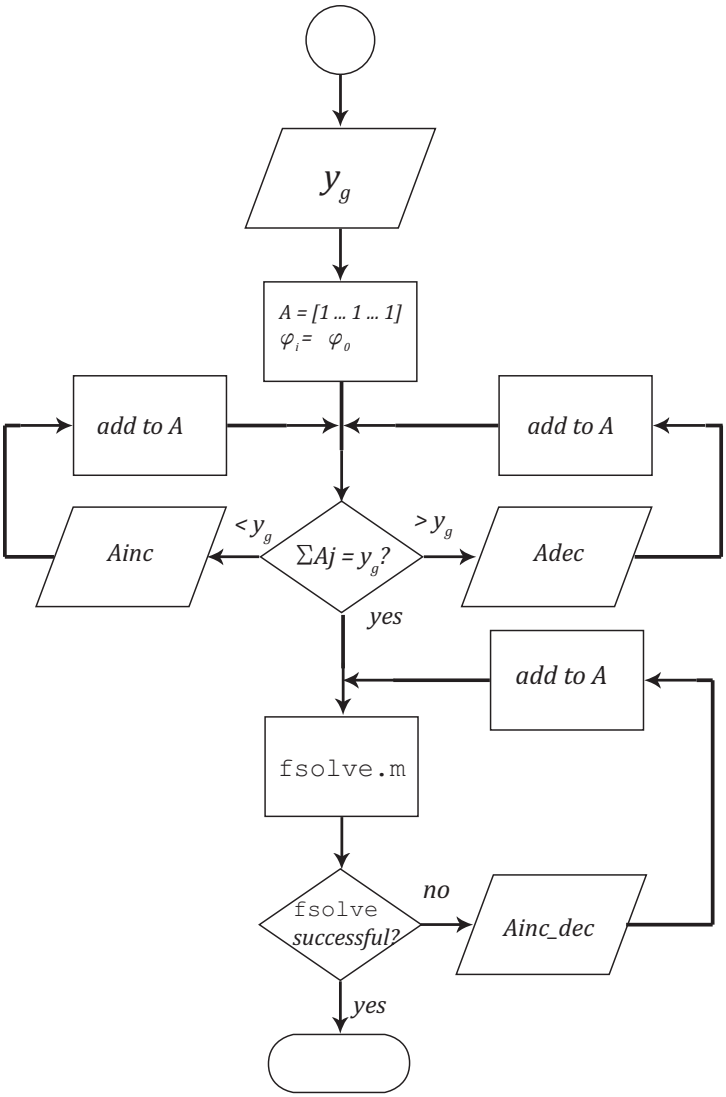

Figure 49: Flowchart depicting algorithm to determine switching pattern

$$\{\forall j \in [0,5] \subset \mathbb{Z}, A_j \mid 0 \leq \sum_{k=0}^{j} A_k \leq 6\} \tag{71}$$

6.4 Determination of switching pattern

6.4.1 General case

The determination of the switching pattern for a general MSDSVS move is illustrated in Figure 49 for the case where $m = 2n + 1$.

The algorithm breaks neatly into two parts: The first part determines a set of

impulse amplitudes that will reach the goal displacement with the minimum number of changes in state to the inputs. The second part determines the phases that result in a vector sum of zero, or zero residual oscillation. **A** is initially set to a vector of length m, where all elements are 1. The vector of phases, ϕ, is set to some convenient initial condition, such as evenly spaced angles between 0 and π. In general, the sum of all the elements of this initial **A** will not equal the goal displacement, y_g. To correct this, the elements of **A** are either incremented or decremented using the rules shown in Table 10. These rules ensure that no element of **A** will ever be zero, which would correspond to deleting an impulse. This would result in too few impulses to guarantee that (68) and (69) are satisfied. This results in a "stairstep" pattern (which contains, by inspection, the minimum number of switches) if $y_g >= m$. If $y_g < m$, this method produces one of several possible patterns with the minimum number of negative valued input transitions. Negative amplitudes correspond to inputs in the opposite direction of the desired displacement and represent wasted energy in one sense, however, they may be necessary to suppress all vibrational modes, especially for short moves. Once a "minimum switching" set of amplitudes is determined, the vector **A** is passed to a numerical solver which attempts to solve (68) by changing the phases ϕ_j. If the solver is successful, the set of amplitudes determined by the first part of the algorithm and the phases returned by the solver constitute the MDSDSVS command. If the solver is unable to determine a solution, **A** is modified using the final rule shown in Table 10. This modifies the individual impulse amplitudes while leaving their sum unchanged, moving to the configuration with the next fewest number of individual input transitions.

6.4.2 Application to the cellular actuator

To generate commands for the cellular actuator, the phases ϕ_j are found by a custom MatLab function, `arb_novib2f.m`, which uses MatLab's (R2009b) native `fsolve.m`

Table 10: Command selection algorithm rules

Name	Form	Note
inc	$[\ 0\ \cdots\ 0\ 1\ 0\ \cdots\ 0\ ]^T$	
Adec	$[\ 0\ \cdots\ 0\ -1\ 0\ \cdots\ 0\ ]^T$	-1 has the same index as some $A_j \neq 1$
Adec	$[\ 0\ \cdots\ 0\ -2\ 0\ \cdots\ 0\ 2\ 0\ \cdots\ 0\ ]^T$	-2 has the same index as some $A_j = 1$
Adec	$[\ 0\ \cdots\ 0\ -2\ 0\ \cdots\ 0\ 1\ 0\ \cdots\ 0\ 1\ 0\ \cdots\ 0\ ]^T$	-2 has the same index as some $A_j = 1$
Ainc_dec	some Ainc + Adec	nonzero elements of Ainc and Adec may not have the same index

function. `fsolve.m` employs an algorithm based on that proposed by Powell [96]. The cellular actuator has two significant resonant modes ($n = 2$), and 6 inputs, so 5 impulses are required for a minimum switching solution that achieves zero residual vibration. The algorithm begins with

$$\mathbf{A} = [A_0\ A_1\ \cdots\ A_5] = [1\ 1\ 1\ 1\ 1] \tag{72}$$

.

`arb_novib2f.m` then follows the procedure in the previous section to generate a sequence of impulses that results in a final position of y_g. *Ainc* is some permutation of the elements of $[\ 0\ 0\ 0\ 1\ 0]^T$, *Adec* is some permutation of the elements of $[\ 0\ -2\ 0\ 1\ 0]^T$. Once y_g is achieved, `fsolve.m` attempts to find ϕ_j that result in zero residual vibration. If it is unsuccessful, *Ainc_dec* of the form $[\ 0\ -2\ 1\ 1\ 0]^T$ is added and `fsolve.m` attempts to find a solution. If it is possible to achieve a vibration-free move with fewer than 5 impulses, `fsolve.m` may calculate two identical ϕ_j. In this case, the two impulses are removed and replaced by a single impulse whose amplitude is the sum of the two amplitudes. A hypothetical example illustrating this process is provided in Appendix E.

6.4.3 Existence and uniqueness considerations

If the first candidate set of amplitudes, $\mathbf{A}$ that satisfies (69) and (71) results in a successful set of ϕ_j that solves (68), for a given set of initial guesses, then it is a minimum switching solution. However, what if the `fsolve.m` fails to find a solution?

One could certainly choose another set of initial conditions and try again, but simply trying many sets of initial guesses may still miss a valid solution. Even if the solver returns a valid solution, might it converge to a different solution with the same number of switches given a different set of initial guesses? Since (68) is a system of nonlinear equations, no statements of existence, non-existence, or uniqueness can be made using classical mathematical methods. Solutions to systems of nonlinear equations are still an area of active research.

Under certain conditions, the Interval Newton Method [97] may be used to make an analytical statement about the existence or uniqueness of a solution for a given set of amplitudes. This depends on the ability to invert the Jacobian of (68), which is singular at every multiple of $\frac{\pi}{4}\frac{f_k}{f_1}$ radians, where f_k is the highest natural frequency, so its application will apply to a small local region rather than globally. Because a solution may be near a singularity, small changes in the natural frequencies of the system may mean that the new solution is not in the neighborhood of the old solution. In fact, a candidate set of amplitudes may produce a solution for a given set of natural frequencies, and fail to produce a solution for neighboring frequencies. For this reason, it is important to verify all MSDSVS patterns experimentally.

6.5 Experimental setup

The relevant resonant frequencies to be suppressed and the desired final position (0-6 first units actuators on) are provided to `arb_novib2f.m`, which returns a table with the number of units on after each switch in the sequence and the time that each switch occurs. An on-off sequence is determined for each individual input that is feasible (a unit that is already on cannot be turned on), and the aggregate of all first layer units at any given time must match the command returned by `arb_novib2f.m`. If the choice of sequence specifies that each input must change state an odd number of times, the pattern for the forward direction can be used to command a motion of the

length in the opposite direction, merely by inverting all input lines in the sequence. This is called a "reversible" pattern.

The DSVS command is implemented by a Silicon Laboratories C8051F120DK microcontroller development kit, running at 25.4 MHz. The command for each first layer unit is generated by each of the 6 Programmable Counter Array (PCA) modules, which toggles an output pin (CEX) state when a match occurs between a given module's internal register and the PCA clock, set to be the system clock/12. This allows implementation of a command which suppresses resonant frequencies as low as 32.3 Hz without rollover. The microcontroller is set to interrupt each time a PCA match occurs on any module, and the subsequent match times are loaded into the various PCA registers. If an output line is supposed to toggle at a given instant, the PCA compare register is loaded with the next transition time at each match interrupt. If it is supposed to maintain its value at the next switching time, the PCA compare register is loaded with the maximum time value, preventing a match from occurring on that module when the next switching time is reached. When the final impulse occurs, the PCA clock is stopped and all output lines are held at their current values until the next move command occurs. Move commands are invoked by a serial command from a PC over RS-232 using the microcontroller's UART and PuTTY open-source telnet software.

Each microcontroller output is wired to an Avago ASSR302-C solid state switching IC, which has two bridges per chip. This is a commercially available, easily procured, low cost component, easily scalable to devices using a large number of cellular actuators. The "low" side of the PZT stack actuator in each first layer unit is always connected to ground. When the upper bridge is activated, the "high" side of the PZT is connected to ground. When the lower bridge is activated, the "high" side of the PZT stack is connected to the source voltage, imposing a voltage across the PZT stack and inducing a displacement. A pair of bridges per stack is necessary because the

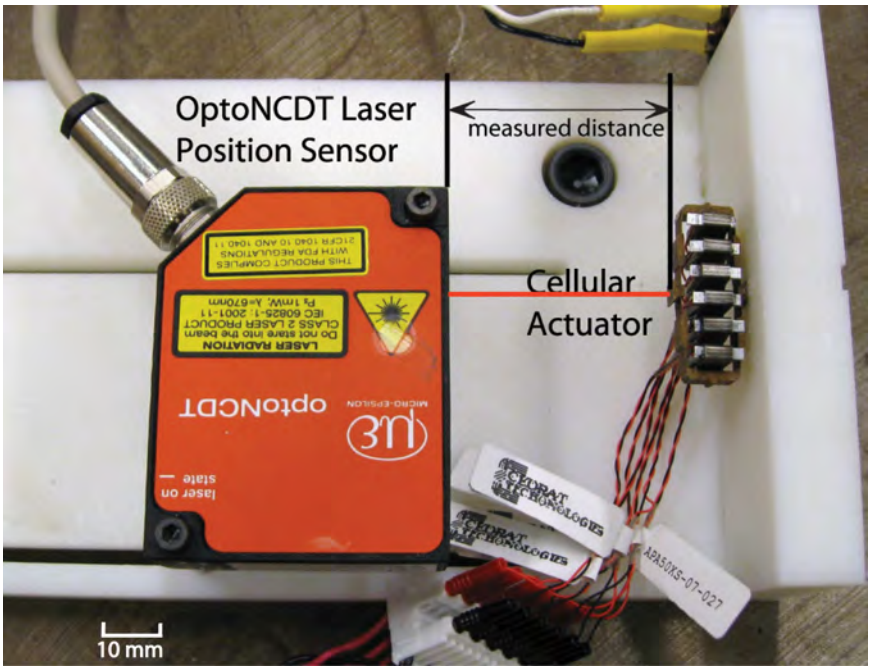

Figure 50: MSDSVS experimental setup

PZT stack actuators are capacitive; simply disconnecting a stack actuator from the source voltage will not cause it to return to its unforced length. It must be grounded so that it can discharge. The ASSR302-C has a delay of 70μs and an R_{dson} of 30 Ω (typical). The drive voltage is provided by an American Power Design A5 series 5 Watt high voltage DC/DC converter. It supplies 33.3 mA at 150V. A delay circuit with a time delay of 40μs prevents cross conduction.

One end of the cellular actuator is fixed to a rigid support. The position of the other end is measured by a Micro-Epsilon optoNCDT ILD 2200-20 laser position sensor with a sampling frequency of 10 kHz. For the verification of the MSDSVS algorithm on cellular actuator hardware, the signal from the laser position sensor was recorded with a LeCroy Waverunner 44MXi mixed signal digital oscilloscope. A photo of the experimental setup is shown in Figure 50.

Table 11: Parameters for experimental frequency response fit

Mode	K	$\omega, [rad/s]$	ζ
1	1.46E-3	478.61	0.0400
2	1.22E-3	2180.3	0.0175

6.6 Experimental results

The frequency response of the cellular actuator was obtained using an HP 3562a spectrum analyzer to generate a sinusoidal input and compare it with the output of the laser position sensor. For the purpose of obtaining the frequency response, the cellular actuator was driven through a Cédrat CA45 amplifier, which has an unloaded bandwidth of 10 kHz. A transfer function for a general vibratory system with two significant modes of vibration with time delay was fit to the data. The frequency response is shown in Figure 51. The mode shapes corresponding to the two resonant peaks are displayed in Appendix D.

Since the displacement generated by the actuator results from deformation only, and not from rigid body displacement, it can be represented as the sum of n lightly damped second order systems:

$$G(s) = \sum_{i=1}^{n} \frac{K_i}{s^2 + 2\zeta_i \omega_i s + \omega_i^2} \tag{73}$$

where for mode i, K_i is the residue, ω_i is the natural angular frequency, ζ is the damping ratio, and s is the LaPlace variable. The results from the experimental transfer function fit for the 2 most significant modes are in table 11. The time delay in the system was determined from the fit to be 3.9 ms.

The MSDSVS and all on/all off commands (command for $y_g = 6$ shown in Figure 52) were applied to the cellular actuator. Commands for the remaining values of y_g are shown in Appendix F. Note that a monotonically increasing command was not found for this particular set of natural frequencies. The response to a step (all

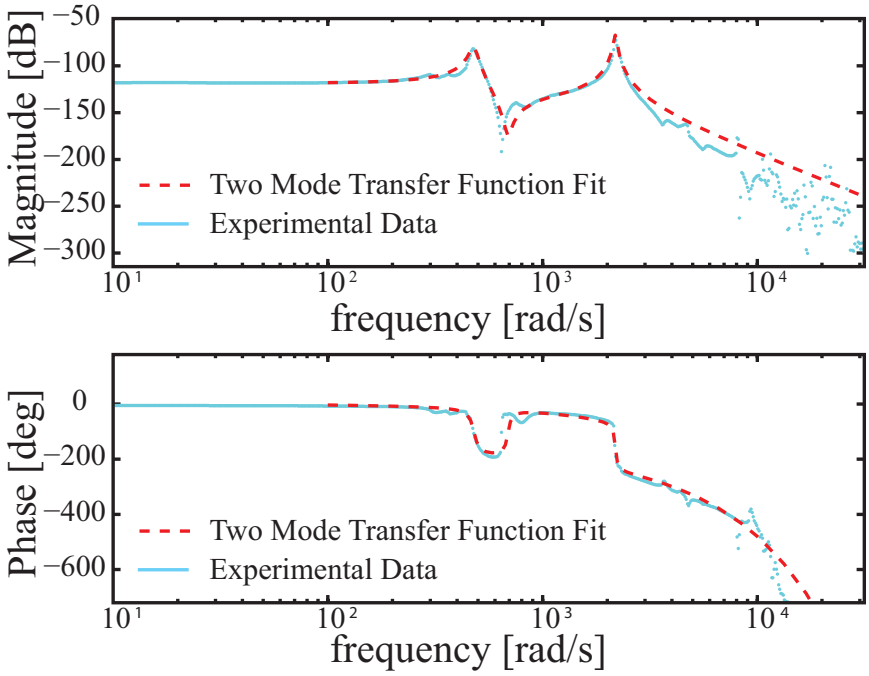

Figure 51: Frequency response of cellular actuator

6 actuators transitioned at the same time) and the response to both vibration suppression commands are shown in Figure 53. The step response shows considerable oscillation (>50% overshoot), due to the lightly damped nature of the system. The various commands are completed by 10 ms, so the remaining period of time shows the decay of any residual oscillation once the command is completed. Note that the response to All On All Off command has the largest transient during the command.

Despite the use of vibration suppression commands, there is still some discernible oscillation remaining in the response after such a command is completed. This is likely due to a combination of factors. Both All On All Off and MSDSVS methods are based on linear analysis, and they suppress oscillation in an actuator that is described accurately by a linear model. In actuality, some non-negligible nonlinear effects are present. The natural frequency of the cellular actuator changes slightly as it extends. The values in Table 11 are only exact for the intermediate position corresponding to the DC offset of the spectrum analyzer, +2V, during the test because the frequency

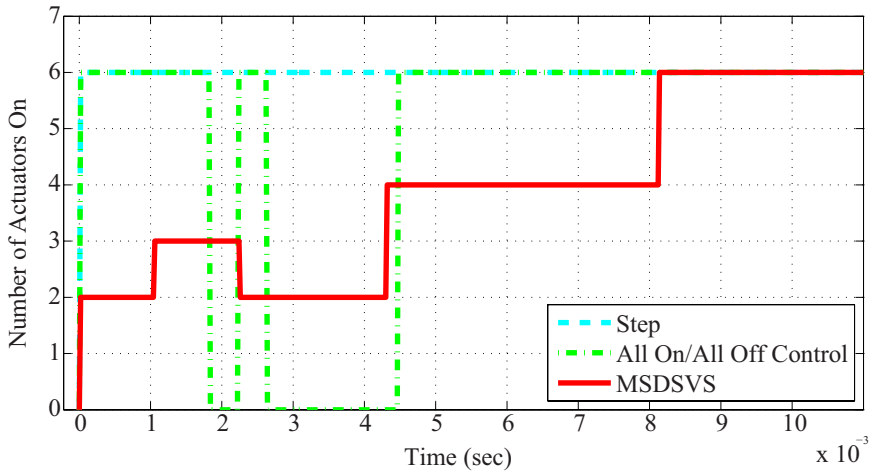

Figure 52: Step, All On/All Off and MSDS Commands to Cellular Actuator, $y_g = 6$

sweep with the spectrum analyzer caused oscillation about this intermediate position. The command was designed based on the frequency for this intermediate length, not the natural frequency of the actuator when it was extended. Most of this remaining oscillation could be removed by further empirical tuning if necessary. The second mode is particularly problematic because its frequency is high enough to where the dead time to prevent cross conduction and time delay in the system begins to become significant. The time constant of the PZT and switching circuit is beginning to become significant at the frequency of the second mode as well. For robotic devices using large numbers of cellular actuators, however, the dominant modes will not be high enough for this to be a concern. In addition, the assumption that an "on" command has the same force magnitude as an "off" command, may not be entirely accurate for the cellular actuator. If these properties are well known, adjustments can be made to compensate for them when generating the command. Finally, during the frequency response testing, it was observed that when the actuator was excited with a pure sinusoid at the frequency of the first resonant mode, the output was not a pure sinusoid. Instead, persistent oscillation at the frequency of the second mode was superimposed over the response at the excitation frequency, indicating a nonlinear dynamic effect which is not captured by the linear analysis.

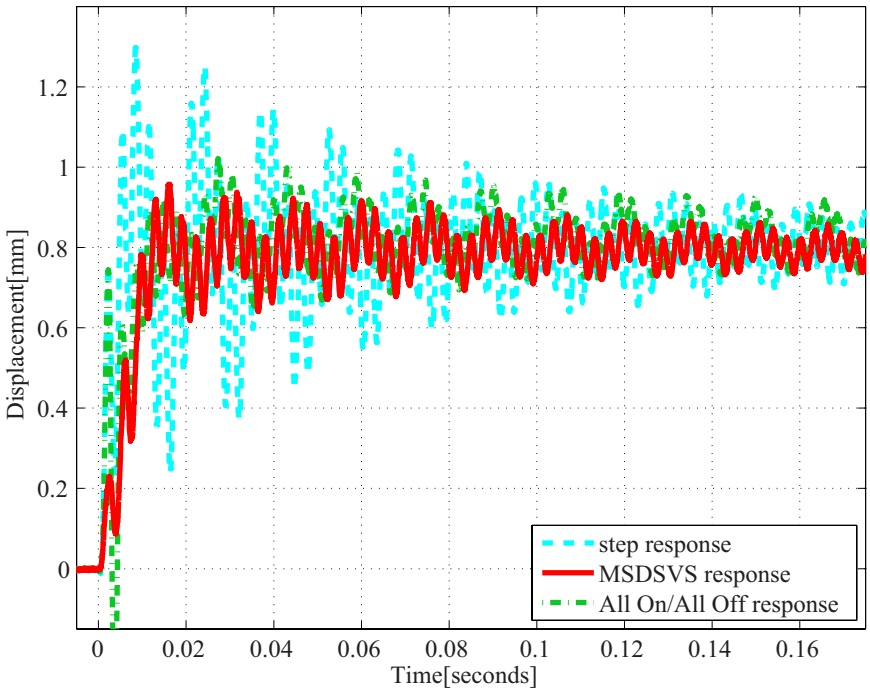

Figure 53: Dynamic Response of Step, All On/All Off and MSDSVS Commands, $y_g = 6$

When either MSDSVS or All On/All Off control is applied to the cellular actuator, the largest component of the FFT (Figure 54) and the RMS oscillation (Figure 55) are reduced by 50% or more in nearly all cases. In most cases, MSDSVS performed slightly better. For $y_g = 6$, the 2% settling time for a step command was measured to be 699 ms. For the all on all off command, the settling time was 477 ms. For MSDSVS, the settling time was 529 ms. With fine-tuning to compensate for all the non-ideal behaviors, it is expected that the settling time for the vibration suppressed commands can be reduced even further.

6.7 Discussion

If both MSDSVS and All On/All Off control both reduce oscillation, one may wonder whether there are any advantages in using one over the other. The advantage of All On/All Off control is that the command is nearly always shorter in duration,

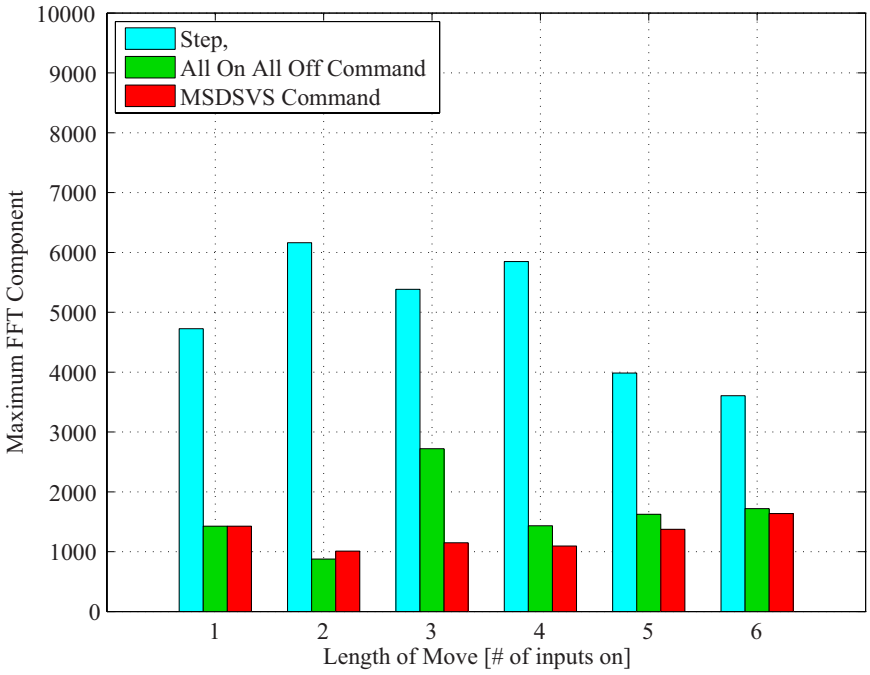

Figure 54: Magnitude of Largest FFT Component, Normalized by Move Distance

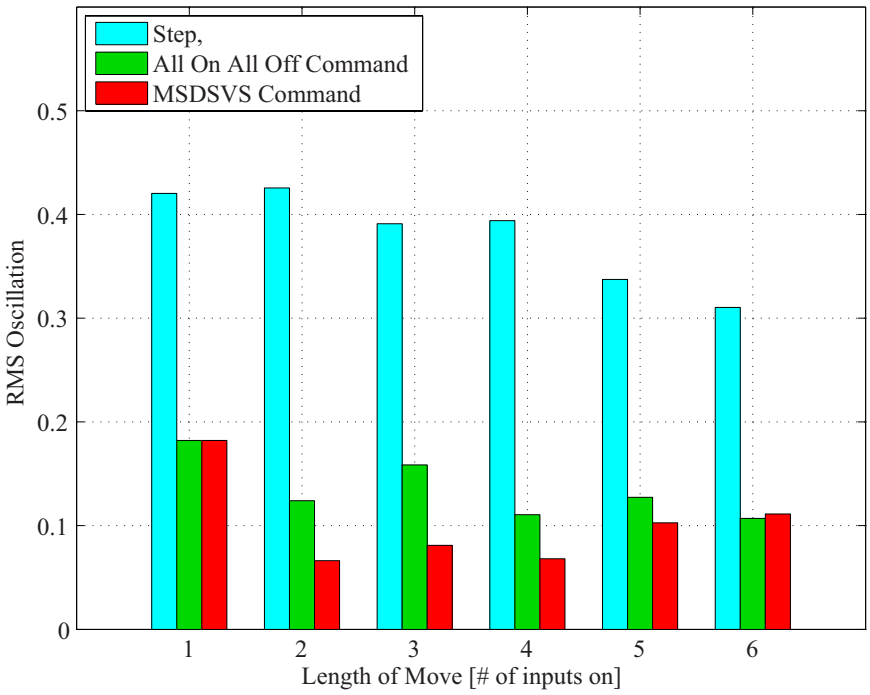

Figure 55: RMS oscillation, normalized by move distance

and thus, in theory, it can reach a vibration-free response sooner than MSDSVS. However, there are a number of advantages to MSDSVS. MSDSVS, since it has fewer transitions, uses less energy than the All On/All Off solution. This corresponds to a smaller control effort being used. In this particular application, there is a certain amount of Joule heating that occurs when the PZT is energized and discharged. This can be expressed as

$$E_J = \int_0^T i^2 R_{dson}\ dt \tag{74}$$

where E_J is the energy dissipated, and i is the current, and T is the charging/discharging time. In order to determine the amount of energy used for a move using a given command, the voltage supplied to the input of the DC/DC converter was measured using a LeCroy ADP305 differential probe. The current to the DC-DC converter was measured with a LeCroy AP015 current probe. After subtracting steady state leakage currents, the product of the two signals was integrated numerically over the time duration of the move. Figure 56 shows how the difference in energy dissipated grows quickly with an increase in the number of inputs. Table 12 shows the number of switches required to reach a given position, which directly correlates to the results shown in Figure 56. A "switch" corresponds to a transition of a single PZT stack, so, for instance, implementing an impulse of $A_j = 2$ would count as two "switches," since 2 stacks must be energized. Table 13 summarizes the information in Figures 54-56. The MSDSVS command reduces the RMS oscillation by 73% and the amplitude of the largest frequency component by 74%. All On/All Off control reduces oscillation by nearly the same amount, but the MSDSVS command uses 37% less energy than the All On All Off Command and shows better robustness properties.

Minimizing the number of cycles also has benefits for the life of the actuator. Piezoelectric bimorphs have been known to delaminate at 10^8 cycles [2].

MSDSVS also has advantages with regard to robustness. Robustness is often

Table 12: Number of switches required to reach y_g for each command

y_g	Step	All On All Off	MSDSVS
1	1	5	5
2	2	10	6
3	3	15	5
4	4	20	8
5	5	25	7
6	6	30	8

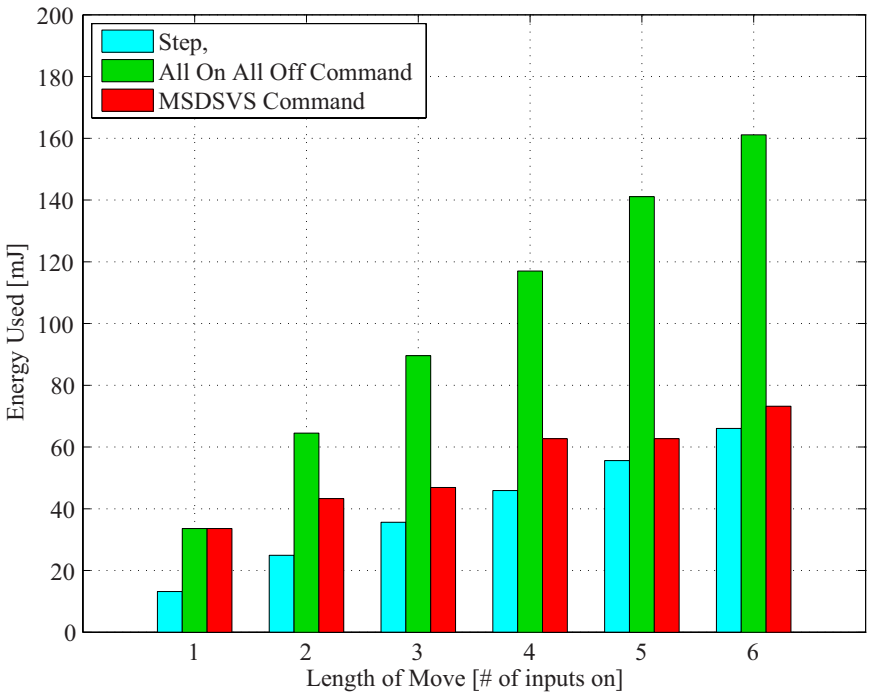

Figure 56: Energy consumption per move

Table 13: Overall performance comparison between commands (RMS and FFT are normalized)

Command	Avg RMS	Avg FFT	Avg Energy/Move Dist. [mJ]
Step	0.380	4950	11.9
All On All Off	0.135	1630	30.0
MSDSVS	0.102	1280	18.6

characterized in terms of the residual amplitude of oscillation, A_r, produced by a given All On All Off or MSDSVS command when an unmodeled or uncertain resonance of frequency ω is present.

$$A_r = \frac{|\sum_{k=0}^{m-1} A_k e^{\frac{j\omega\phi_k}{\omega_1}}|}{\sum_{k=0}^{m-1} A_k} \times 100\% \tag{75}$$

The sensitivity plot (A_r vs ω) of the MSDSVS command and the All On/All Off command is shown in Figure57. MSDSVS shows much less amplification, in general, if there is an unmodeled lightly damped mode. Because of the periodic nature of the vector diagram summation, both types of commands will suppress additional frequencies higher than those they are designed to suppress. The All On All Off command has two such frequencies near 590 Hz and 720 Hz, but across the board, MSDSVS performs better. Figure 58 shows the time response of the cellular actuator to an All On/All Off command and an MSDSVS command when both commands were designed with an assumed first mode natural frequency of 45.7 Hz, rather than the measured frequency of 76.1 Hz ($y_g = 6$). MSDSVS still exhibits fair vibration suppression properties, even when the frequency is off by 40%, whereas All On/All Off control exhibits almost no vibration suppression.

Figure 59 shows the response when two masses are added to the cellular actuator, but the commands are the same as shown in Figure 52, again producing a mismatch between the frequencies suppressed by the command and the natural frequency. The natural frequencies of the modified actuator are $f_1 = 56.8$ Hz and $f_2 = 341$ Hz. In this case, both All On All Off control and MSDSVS still provide some benefit. The amount of residual oscillation for the All On All off and MSDSVS methods are comparable, as predicted by Figure 57 when the first mode is lowered.

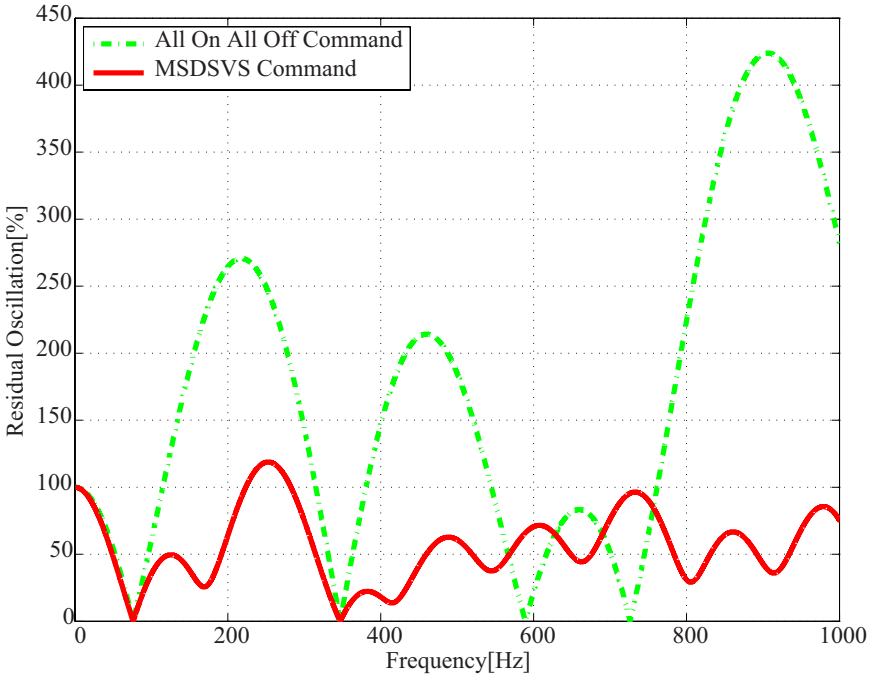

Figure 57: Sensitivity plot for All On/All Off control and MSDSVS

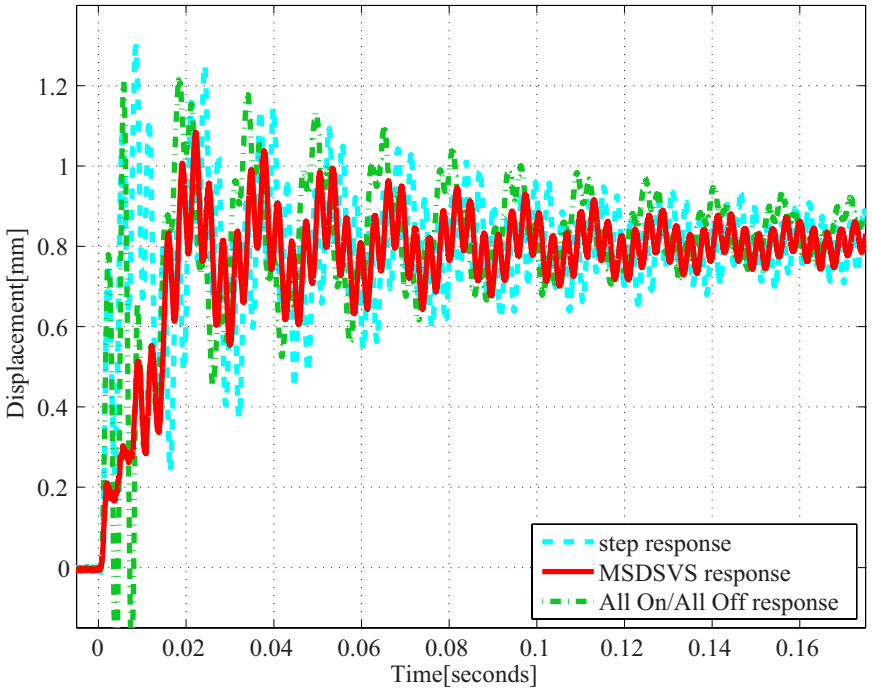

Figure 58: Cellular actuator response when command designed based on incorrect natural frequency

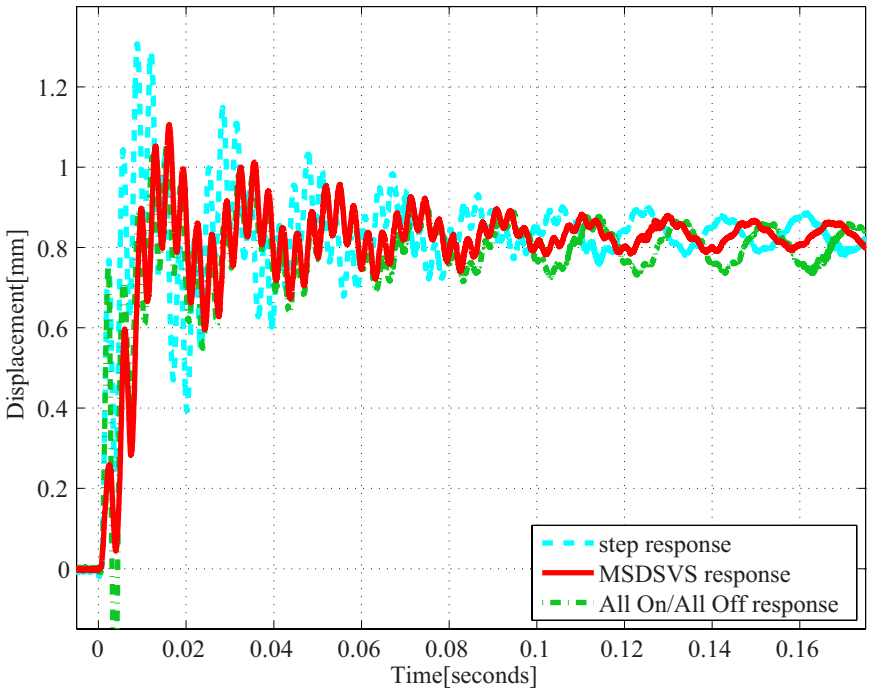

Figure 59: Cellular actuator response when the natural frequency is changed

6.8 Summary

This chapter presented the discrete switching vibration suppression (DSVS) method for flexible robotic systems with redundancy in actuation. This represents a greater class of vibration suppression commands then applying existing approaches identically to all inputs. DSVS successfully reduces the amplitude of oscillation when applied to the redundant, flexible cellular actuator. Choosing the DSVS command with the minimum number of total input transitions has specific benefits, namely, lower energy usage and increased robustness to modeling errors.

Although the example mechanism used had two modes of vibration, this method is sufficiently general to be used for systems with large numbers of vibrational modes, provided a numerical solution to the system of equations can be found. When there is only a single mode of vibration, the determination of appropriate switching times can be greatly simplified, and this will be discussed in Chapter 7.

CHAPTER VII

CONTROL OF THE BIOLOGICALLY INSPIRED CAMERA POSITIONER

7.1 Introduction

Chapter 6 presented Minimum Switching Discrete Switching Vibration Suppression (MSDSVS), a method for point to point motion with zero residual vibration for systems with highly discretized redundant actuation. The method was demonstrated on a 6 input actuator in a single-ended configuration with two significant modes of vibration.

This chapter applies this method to the camera positioning mechanism of Chapter 5, which has two cellular actuators in an antagonistic configuration with 16 inputs each. LabView firmware is developed that allows a user to complete any arbitrary sequence of moves using MSDSVS to suppress residual oscillation.

7.2 Natural vibrational modes of the camera positioner

The natural frequencies of oscillation of the camera positioner were determined using simple experiments. The 16 piezoelectric inputs on one side were excited by a swept sinusoidal signal, generated by an Agilent function generator, which was amplified by a Cédrat CA45 linear amplifier. The opposite side was not energized. The amplitude was read in the time domain during the sweep and the maximum amplitude was noted to be at 9.9 Hz. Since the natural frequencies were low, the residues and damping values are not required for MSDSVS, and the change in amplitude was distinct enough to resolve the resonant frequency to an accuracy of 0.1 Hz, this very simple experiment is sufficient for the purposes of the investigation conducted in this chapter.

Surprisingly, the amplitude of oscillation of any remaining modes was insignificant relative to the amplitude of vibration of the first mode. Therefore, for satisfactory operation of the camera positioning mechanism, it is only necessary to suppress a single mode, greatly simplifying the determination and implementation of appropriate MSDSVS commands. If higher modes prove to be troublesome on similar devices in the future, the methods of Chapter 6 can be used.

7.3 Determination of MSDSVS switching patterns

Since the plant has only one natural frequency that needs to be suppressed, vibration suppression can be achieved using only 3 impulses. Given a set of amplitudes, the timings can be calculated analytically using the following formulas, obtained by setting the sum of the effects of all impulses to be equal to zero in the complex plane. With a single mode, this results in:

$$\phi_1 = \arccos \frac{A_2^2 - A_0^2 - A_1^2}{2A_1A_0} \tag{76}$$

$$\phi_2 = \arcsin -\frac{A_1 \sin \phi_1}{A_2} \tag{77}$$

where $A_i \in \mathbf{D} \subset \mathbb{Z}$ are the integer amplitudes applied to the camera positioner and ϕ_i represent the phase delay of impulse i with respect to the resonant frequency. Requiring that

$$\frac{A_2^2 - A_0^2 - A_1^2}{2A_1A_0} \in [\ -1,\ 1\ ] \tag{78}$$

and

$$\frac{A_1 \sin \phi_1}{A_2} \in [\ -1,\ 1\ ] \tag{79}$$

(so that all $\phi_i \in \mathbb{R}$) defines the allowable set of amplitudes for which a vibration-free point-to-point move is possible.

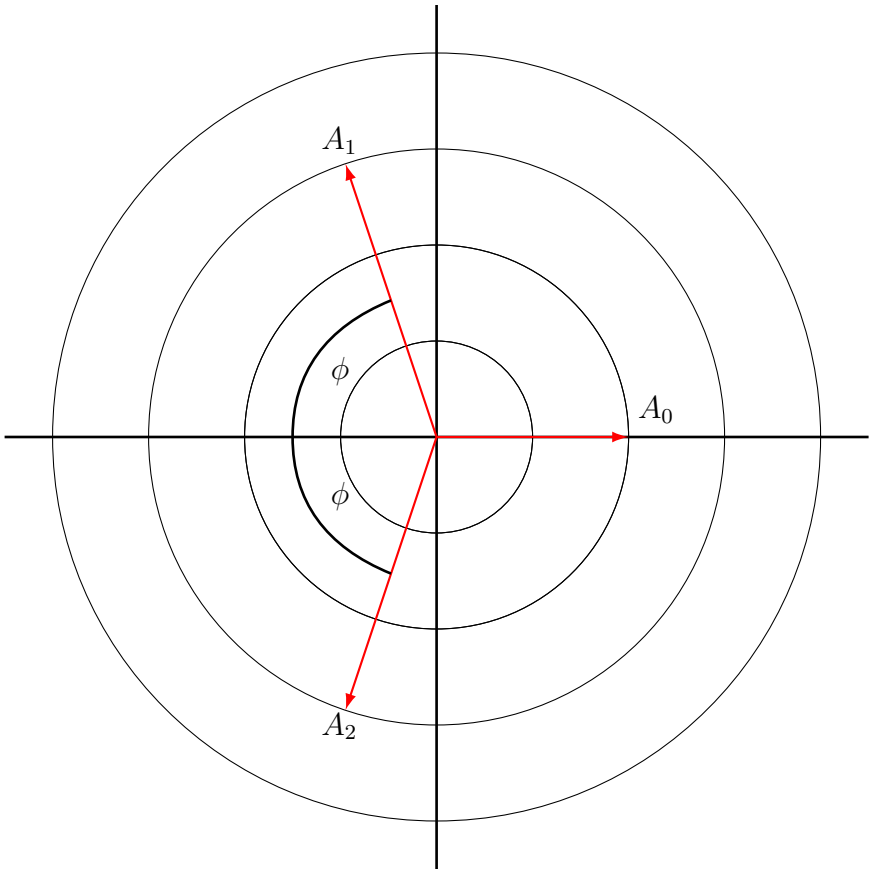

Figure 60: Representation of impulses in the complex plane for an odd number of impulses

Because (76,77) are analytical expressions, a solution is guaranteed, provided that the relative magnitudes of the impulses result in arguments in the domain of the inverse trigonometric functions. This means that a monotonic "staircase" solution is always possible for a single frequency for move distances greater than 1. However, it is simpler to compute the solution graphically than to use (76) and (77). Representing the impulses as vectors in $\mathbb{C}$, the first impulse corresponds to a vector directed along the positive real axis. For even numbered distances, a vibration free move can be computed that includes two impulses of equal amplitude, one along the positive real axis and the other along the negative real axis. This is equivalent to a ZV shaper [58] applied to a step input. For odd numbered move distances, the command can be computed as follows:

Table 14: MSDSVS patterns for the biologically inspired camera positioning mechanism

move distance	A_0	A_1	A_2	ϕ_1	ϕ_2
Units Activated				°	
1	1	-1	1	60	120
2	1	1	n/a	180	n/a
3	1	1	1	120	240
4	2	2	n/a	180	n/a
5	1	2	2	104.47	255.52
6	3	3	n/a	180	n/a
7	3	2	2	138.59	221.41
8	4	4	n/a	180	n/a
9	3	3	3	120	240
10	5	5	n/a	180	n/a
11	5	3	3	146.44	213.56
12	6	6	n/a	180	n/a
13	5	4	4	128.68	231.31
14	7	7	n/a	180	n/a
15	5	5	5	120	240
16	8	8	n/a	180	n/a

1. Decompose the move distance y_g into $y_g = q + p$, where q is even and p is odd. p and q must be chosen such that (78) and (79) are satisfied.

2. Set the first amplitude, $A_0 = p$. This lies along the positive real axis.

3. Set the two remaining amplitudes $A_1 = A_2 = q/2$.

4. A_1 and A_2 will be represented as vectors of equal magnitude in the complex plane, at an angle ϕ above and below the negative real axis.

5. Solve for the ϕ that gives a vector sum of zero.

Figure 60 illustrates the phasors in the complex plane for an odd-numbered move. The MSDSVS patterns computed using this method are listed in Table 14. When multiple solutions were found, the one that could be completed in minimum time was chosen. Phases can be converted to timings using the natural frequency of 9.9 Hz.

7.4 Experimental evaluation

The experimental setup consists of the camera positioner and drive circuit described in Chapter 5. Firmware is developed for the positioning and control of the mechanism on both the NI-Rio embedded processor and the FPGA backplane. The amplitude and timing values of the MSDSVS patterns for all destinations are stored in a text file stored in memory of the processor module. This file is read when the program begins and stored in RAM. The user can designate the destination position using the LabView front panel interface. When the user sets a new destination, the processor algorithm computes the move distance based on the current position and the destination and loads the appropriate pattern into the FPGA's memory. It then waits for the user to initiate the move. If the user changes the destination without initiating the move, the pattern is simply overwritten.

Once the user initiates the move, the FPGA executes the MSDS pattern, free from any supervision by the embedded processor. Any input from the user during the move will not be acted upon until the move completes. Timings are derived from the FPGA 40 MHz clock. The FPGA keeps track of which inputs are active and inactive during the move, i.e. available for use or not available for use. Further details about the firmware can be found in Appendix G.

The position is measured by a Midori Orange Pot CP-30H (hall effect variable resistor). This is so that the true angle of the camera can be recorded for experimental purposes. In applications such as autonomous vehicle navigation, the camera angle could be determined using salient features in the image, and once calibrated, the potentiometer could be removed.

7.5 Results

Figure 61 shows the step response of the camera positioner. It is evident that the device is lightly damped from the large overshoot, particularly for the longer moves.

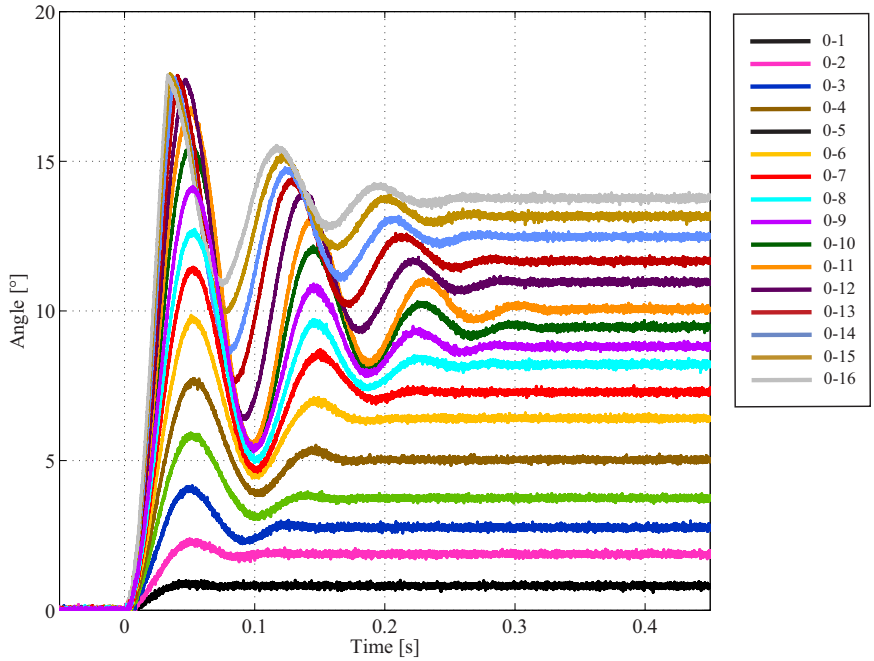

Figure 61: Step response of the biologically inspired camera positioner. Curves shown for a single direction, center to all 16 positions shown.

Locations 13-16 also show a saturation effect; most likely the overshoot causes the output flange to collide with the first layer units. This is further motivation to suppress oscillation in the device, as the quasistatic experiments in Chapter 4 showed that no such collisions occur in the steady state, even at maximum activation.

Figure 62 shows the response to the various MSDSVS patterns for each of the 16 discrete positions. The resulting responses have low overshoot, or none at all. The response reaches steady state within 0.14 s. Therefore this method is effective in suppressing vibration for saccades.

7.6 Discussion

Figure 61 shows that there are some nonlinearities in the camera positioner system dynamics. This is primarily due to variation in frequency with actuator length. However, despite these nonlinear effects, the MSDSVS commands based on the simple linear model of the system are effective for the range of motion of this device. For long serial chains of actuators such as these, some more advanced or heuristic methods

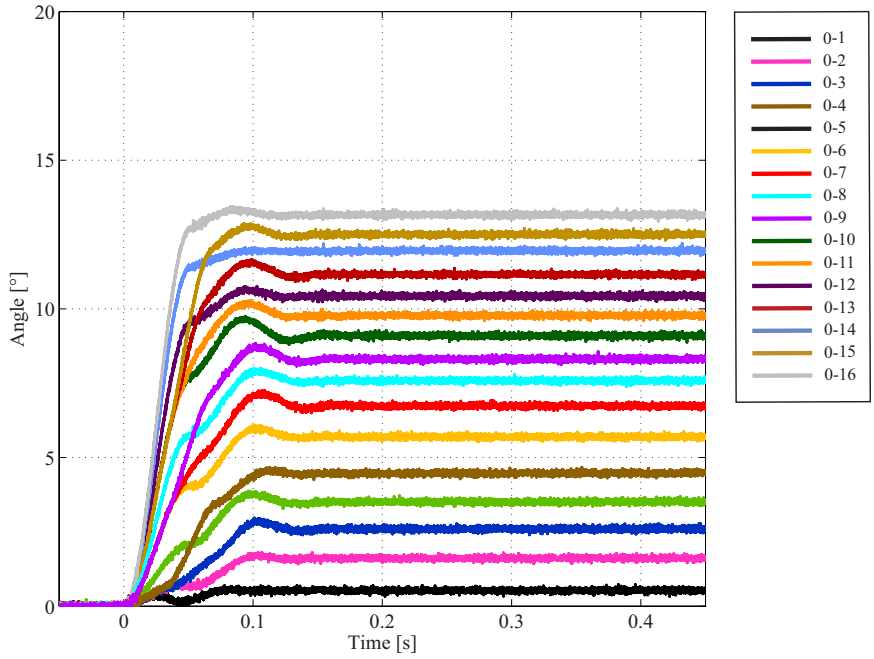

Figure 62: Minimum switching discrete switching vibration suppression response of the biologically inspired camera positioner. Curves shown for a single direction, center to all 16 positions shown.

may be necessary to mitigate the change in natural frequency with length.

7.7 Summary

This chapter has presented the use of MSDSVS on the biologically inspired camera positioner. This method is useful for fast, saccadic-like motions to rapidly reorient the camera. Experiments have shown that camera positioner has a single significant resonant mode, greatly simplifying the computation of MSDSVS commands. The response to the MSDSVS command shows a marked reduction in oscillation over naive step commands, particularly for longer moves. Chapter 8 will present some analysis and simulations on possible closed-loop control methods for smooth pursuit motions for systems with highly discretized inputs and lightly damped high frequency modes of vibration.

CHAPTER VIII

INTERSAMPLE DISCRETIZATION OF CONTROL INPUTS FOR FLEXIBLE SYSTEMS WITH QUANTIZED CELLULAR ACTUATION

The methods of Chapters 6 are useful for point-to-point motion, however they are limited, because they are unable to reduce oscillation emanating from disturbance inputs in the environment. Some form of feedback control is required in order to do reject disturbances.

However, if a feedback control system is designed, the control designer must confront the problem that the control input cannot take on a continuous range of values. This chapter discusses this quantization of the input and presents a method whereby high-precision switching between neighboring control input values can be used to reduce oscillation. The method is predicated on the assumption that the plant can be partitioned easily into a low frequency model with dynamics below the Nyquist frequency and some lightly damped modes above the Nyquist frequency. As discussed in Chapter 7, the camera positioner has only one mode that is visible in the response, and does not fit this paradigm. For this reason, the method is evaluated in simulation.

8.1 Concept

8.1.1 Physical considerations

In the case of a system driven by an array of cellular actuators the actuation is quantized significantly. Often times to achieve the desired displacement using cellular actuator technology, it is necessary to put several units in series. Units may also be connected in parallel to achieve a higher force. Each PZT stack in the entire

array can be considered to be an input. As in previous chapters, an actuator with multiple inputs for a given degree of freedom is referred to as having redundant actuation. This does not mean that the multiplicity of inputs is unnecessary, for in this case, the multiplicity of amplified PZT stacks are needed to produce the desired displacement or force. However, having multiple inputs per degree of freedom gives the ability to enforce additional dynamic constraints beyond simply specifying an output displacement or force.

Because of hysteresis present in the PZT material and the capacitive nature of PZT stack actuators, it is advantageous to restrict operation of an individual PZT stack to be simply "on" or "off". This simplifies the drive electronics by eliminating the need for linear drive transistors, and reduces the amount of energy dissipated as waste heat. This limitation represents a quantization of the actuation in the system. In order to be implemented on such an actuator array, any control input to the actuator must be mapped to energizing a certain number of actuators. Usually the total number of inputs represents a coarser precision than that imposed by typical A/D converters. Because the actuator is compliant, the actuator itself may have high frequency flexible modes. Therefore, the control must treat these flexible effects along with the quantization effects.

In this chapter a control architecture is proposed which simultaneously treats the quantization in actuation and dissipates energy in the flexible modes. This architecture is called *intersample discretization*. The cellular actuators have a fast response and therefore quantization in time can be neglected, so the actuator is capable of switching between the neighboring integer values near the nominal control input for the sample with high precision in time. These switches are chosen in such a way as to drive the actual state value to that predicted by a simpler model.

8.1.2 System modeling

Ignoring for the moment the quantization in actuation, and considering the system dynamics of the actuator itself (possibly driving some rigid robotic link), energizing some portion of the total input capability of the actuator array can be considered to be a single input to the system with quantization. The output of the system is some displacement at the end of the actuator or link, such as a joint angle. Assume that any deformations are linearly elastic, and the behavior is adequately described by simple lumped parameter models. Should any oscillation be induced in the system, it is assumed that such oscillations will continue unabated for an arbitrarily long period of time, and therefore damping can be neglected. A cellular actuator typically has very lightly damped flexible poles, on the order of $\zeta = 10^{-2}$. This is common practice for systems with very lightly damped flexible poles. Therefore, the system can be reasonably well represented by a single input, single output, linear, time–invariant model.

If the frequencies of oscillation of a flexible system are known, a continuous time linear model of the system can be generated using the assumed mode method. The frequencies of the modes with the most significant contribution can determined by finite element analysis, finite differences, or experiment.

It is likely that the frequency of several flexible modes, ω, will be above the Nyquist frequency, so it is not possible to suppress this oscillation by traditional discrete–time control techniques. However, oscillations at these frequencies will appear in the continuous–time output and degrade performance. This Chapter assumes that the state is known (or can be estimated) at every sample time kT where $k \in \mathbb{Z} > 0$. In addition, let there be a simplified reference model that includes only system behavior that can be controlled by conventional discrete–time techniques at sampling frequencies imposed by computational, communication, and sensor constraints. This would typically be some low order system with dominant damped conjugate poles

whose associated natural frequency is significantly below the sampling frequency.

8.1.3 Control design

A block diagram of the proposed control system is shown in Figure 63. $G(z)$ is a discrete–time controller designed to give the reference model the desired performance. The output of $G(z)$ is a continuously variable sampled data control input. It is followed by the *Intersample* block, which maps the output of $G(z)$, $\overline{u}$, to a quantized control input $u(t)$ that can be implemented by the actuator, that is piecewise constant but takes multiple values during the sample.

$$\begin{aligned} Intersample : \mathbb{R} &\rightarrow N \subset \mathbb{Z}^m \\ \overline{u} &\mapsto u(t) \end{aligned} \tag{80}$$

The goal of the *Intersample* block, given $\overline{u}$ and the state at time $t = kT$ is to choose a command $u(t)$,which consists of piecewise constant values $u_i \in N$, held from $t_i \in [\ 0,\ T\ ]$ to t_{i+1} such that when $u(t)$ is applied to the flexible system, the value of the state at the end of the sample $t = (k+1)T$ is as close as possible to the state of the reference model, augmented appropriately (e.g. padded with zeros) so that the state vectors of the reference model and the flexible system have the same dimension. Figure 64 illustrates this idea.

Defining the state error at the end of the sample as

$$\tilde{\mathbf{x}}((k+1)T) = \begin{bmatrix} \mathbf{x_r}((k+1)T) \\ \mathbf{w} \end{bmatrix} - \mathbf{x}((k+1)T), \tag{81}$$

where $\mathbf{w}$ is some vector chosen appropriately to augment the state so that the subtraction can be effected and the result makes physical sense. Since the system is linear and $u(t)$ is piecewise constant the state at the end of the sample can be predicted using:

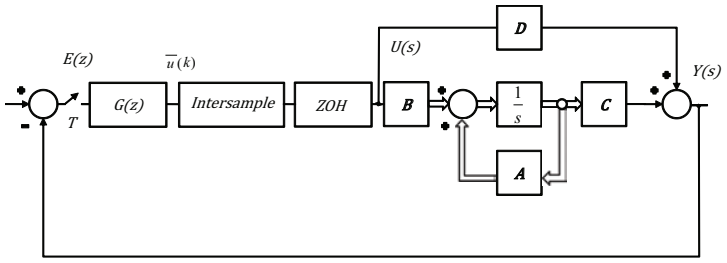

Figure 63: Block diagram of control system

$$\mathbf{x}((k+1)T) = \mathbf{e}^{\mathbf{A}T}\ \mathbf{x}(kT) + \sum_{i=1}^{p-1} u_i\ \mathbf{e}^{\mathbf{A}((k+1)T - t_{i+1})} \int_{t_i}^{t_{i+1}} \mathbf{e}^{\mathbf{A}(t_{i+1}-t)}\mathbf{B}\ dt. \tag{82}$$

A and **B** are the state and input matrices of the flexible system, respectively. $u_i \in N$ and $t_i \in [\ kT,\ (k+1)T\ ]$ can be chosen according to some rule to create some $u(t)$ that drives the state to that of the reference model. The minimization problem is then defined as

$$\min_{u_i, t_i}\ J, \quad J(u_i, t_i) = \tilde{\mathbf{x}}^T \mathbf{P} \tilde{\mathbf{x}},\ i = 1 \ldots m, \tag{83}$$

where **P** is a positive definite weighting matrix. Any such high frequency oscillations will be minimized as the system state is brought near to the augmented reference model state. This may require several samples, especially if N is small, limiting the control authority.

8.2 Illustrative example

8.2.1 Mathematical formulation

Consider as an example a system that consists of rigid body mode, and an undamped flexible second order system:

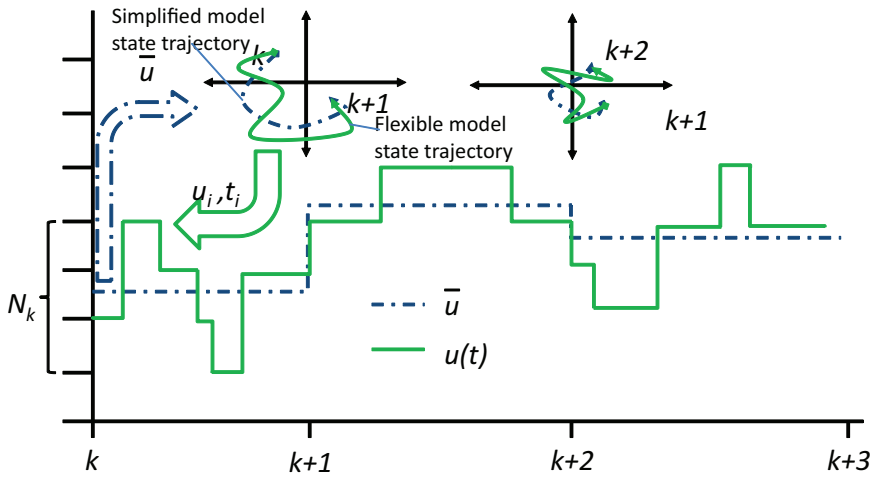

Figure 64: Determination of integer–valued command

$$
\begin{aligned}
\dot{\mathbf{x}} &= \mathbf{A}\mathbf{x} + \mathbf{B}u \\
y &= \mathbf{C}\mathbf{x} + \mathbf{D}u \\
\mathbf{A} &= \begin{bmatrix} 0 & 1 & 0 & 0 \\ -\omega^2 & 0 & \omega^2 & 0 \\ 0 & 0 & 0 & 1 \\ 0 & 0 & 0 & 0 \end{bmatrix} \\
\mathbf{B} &= \begin{bmatrix} 0 & 0 & 0 & \frac{1}{M} \end{bmatrix}^T \\
\mathbf{C} &= \begin{bmatrix} 1 & 0 & 0 & 0 \end{bmatrix} \\
\mathbf{D} &= 0.
\end{aligned} \tag{84}
$$

This model could represent a two mass system separated by a spring and is illustrated in the block diagram shown in Figure 65. The intermediate signal between the two blocks will be identical to the reference model output for the same input. To begin, choose a simple single rigid mass as the reference model, (along the lines of (85)), and then try to design an intersample discretization method that will remove oscillation present in the flexible mode. The model for a simple mass of total mass M is:

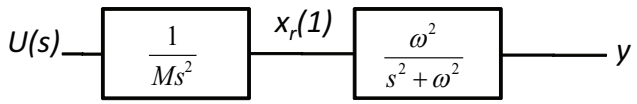

Figure 65: Block diagram of flexible plant

$$
\begin{aligned}
\dot{\mathbf{x}}_\mathbf{r} &= \mathbf{A_r x_r} + \mathbf{B_r} u \\
y &= \mathbf{C_r x_r} + \mathbf{D_r} u \\
\mathbf{A_r} &= \begin{bmatrix} 0 & 1 \\ 0 & 0 \end{bmatrix} \\
\mathbf{B_r} &= \begin{bmatrix} 0 & \frac{1}{M} \end{bmatrix}^T \\
\mathbf{C_r} &= \begin{bmatrix} 1 & 0 \end{bmatrix} \\
\mathbf{D_r} &= 0.
\end{aligned} \tag{85}
$$

For simplicity, let $M = 1$ kg and $T = 0.1$ s. Using well–known discrete time control design techniques, one can design a controller that will achieve a desired damping ratio $\zeta = 0.707$ and a rise time of 0.16 s:

$$G(z) = \frac{56.9(z - 0.735)}{z + 0.322}. \tag{86}$$

To design the intersample discretization, the method begins with a candidate function that is a pulse width modulated (PWM) version of $\overline{u}$, with m pulses that alternately take values of $\lfloor \overline{u} \rfloor$ ($floor(\overline{u})$) and $\lceil \overline{u} \rceil$ ($ceil(\overline{u})$). This enforces the constraint that

$$\int_0^T \overline{u}\ dt = \int_0^T u(t)\ dt. \tag{87}$$

This signal can be viewed as the sum of a naive floor quantization signal $\lfloor \overline{u} \rfloor$ and m pulses of amplitude 1 and duration t_{dc}, where t_{dc} is chosen such that (87) is satisfied.

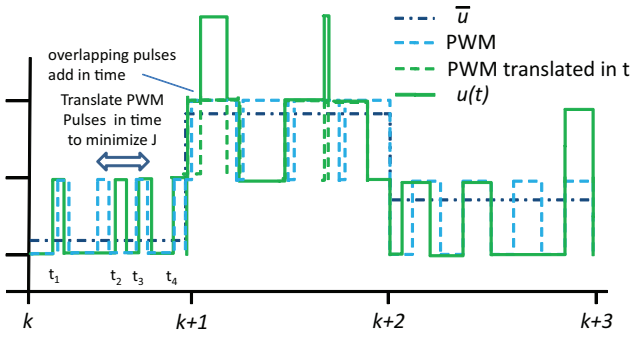

Figure 66: Discretization using a PWM candidate function.

Leaving t_{dc} constant, the times t_i when the pulse begins are varied such that J is minimized. Discretization starting from a PWM function is illustrated in Figure 66. For the above example described by (84), it makes sense to choose $\mathbf{w} = \mathbf{x_r}((k+1)T)$, so that $\tilde{\mathbf{x}}_\mathbf{3}, \tilde{\mathbf{x}}_\mathbf{4}$ represent the difference in the rigid body mode due to the fact that the true system receives the quantized input $u(t)$, rather than the discrete time control input $\overline{u}$. Since for any two pulses $\{\ t_i,\ t_j\ \}$, $t_j - t_i$ may be less than t_{dc}, some pulses may overlap, and due to their addition $u(t)$ may contain values other than $\lfloor \overline{u} \rfloor$ and $\lceil \overline{u} \rceil$. In fact, with this implementation,

$$N \equiv [\ \lfloor \overline{u} \rfloor,\ \lfloor \overline{u} \rfloor + m\ ]. \tag{88}$$

If $\mathbf{x}(kT)$ is known, $u(t)$ is piecewise constant and consists of a floor quantization and a series of pulses of amplitude 1, (82) reduces to:

$$\begin{aligned} \mathbf{x}((k+1)T) &= \mathbf{e}^{\mathbf{A}T}\ \mathbf{x}(kT) + \lfloor \overline{u} \rfloor \int_{kT}^{(k+1)T} \mathbf{e}^{\mathbf{A}((k+1)T-t)}\mathbf{B}\ dt \\ &+ \sum_{i=1}^{m} \mathbf{e}^{\mathbf{A}((k+1)T-(t_i+t_{dc}))} \int_{t_i}^{t_i+t_{dc}} \mathbf{e}^{\mathbf{A}(t_{dc}-t)}\mathbf{B}\ dt. \end{aligned} \tag{89}$$

Since these are considered to be linear, time–invariant systems, these results apply equally to any sample k. Therefore kT and $(k+1)T$ in the second and third terms can be replaced by 0 and T, respectively. Defining

$$\Phi = \mathbf{e}^{\mathbf{A}T}, \tag{90}$$

$$\Gamma_T = \int_0^T \mathbf{e}^{\mathbf{A}(T-t)}\mathbf{B}\ dt, \tag{91}$$

$$\Xi = \mathbf{e}^{\mathbf{A}t_{dc}}, \tag{92}$$

$$\Gamma = \int_0^{t_{dc}} \mathbf{e}^{\mathbf{A}(t_{dc}-\tau)}\mathbf{B}\ d\tau, \tag{93}$$

using a change of variable on every term in the series $\tau = t - t_i$ and using (90) - (93), (89) can be rewritten as:

$$\mathbf{x}((k+1)T) = \Phi\ \mathbf{x}(kT) + \lfloor \overline{u} \rfloor\ \Gamma_T + \Phi\ \Xi^{-1} \sum_{i=1}^{m} \mathbf{e}^{-\mathbf{A}t_i}\ \Gamma. \tag{94}$$

Φ and Γ_T only need to be evaluated once. Since t_{dc} is constant for a given sample k, Ξ and Γ will be evaluated once per sample, and not repeatedly during the optimization routine. Since $\mathbf{e}^{-\mathbf{A}t_i}$ will be evaluated as a truncated series expansion, and T is much larger than the period of the flexible modes, it is important to approximate $\mathbf{e}^{-\mathbf{A}t_i}$ over as short a time interval as possible. Any approximation of $\mathbf{e}^{-\mathbf{A}t_i}$, will be accurate for the earlier pulses, but not the later ones. Therefore, it is advantageous to express (94) in terms of $\mathbf{e}^{-\mathbf{A}(t_i - t_{i-1})}$. In this case, the algorithm will only be approximating the matrix of exponentials over a time period on the order of T/m, rather than T, if pulses are relatively evenly spaced. The global error will still increase for later pulses due to multiplication of inaccurate matrices, but the local error for each approximation should be smaller. Using well–known properties of the matrix of exponentials (94) can be written as:

$$\mathbf{x}((k+1)T) = \Phi\ \mathbf{x}(kT) + \lfloor \overline{u} \rfloor\ \Gamma_T + \Phi\ \Xi^{-1} \sum_{i=1}^{m} [\prod_{j=1}^{i} \mathbf{e}^{-\mathbf{A}(t_j - t_{j-1})}]\ \Gamma. \tag{95}$$

With a prediction of $\mathbf{x}((k+1)T)$ given by (95), the optimal switch timings t_i can be computed using any suitable optimization routine. Then $u(t)$ can be constructed for any sample k simply by adding all m pulses of width t_{dc} beginning at respective times t_i to $\lfloor \overline{u} \rfloor$. This results in an appropriately quantized input that can be implemented by the actuator.

8.2.2 Computer simulation results

In order to calculate the appropriate *Intersample* function, the state of the system at time $t = kT$ must be known. Once measurement and estimation is complete and $\overline{u}$ has been calculated, the command $u(t)$ can be defined deterministically for the entire sample. However, it is not possible to determine *Intersample* or $u(t)$ for subsequent samples because its calculation depends on the evolution of the state. In a real system, this would require some measurement(s) and estimation of remaining state variables. The system is simulated using a sample–by–sample approach. A value of $\mathbf{x}(kT)$ is returned by the previous iteration. $\mathbf{x}(0)$ can be chosen to be nonzero to simulate the response to some existing amount of initial oscillation or error. $G(z)$ is run for the current sample to compute $\overline{u}$. Transition timings for a PWM signal satisfying (87) are computed based on $\overline{u}$. These timings constitute the initial guess for the minimization routine. This evaluation used MatLab's `fmincon.m` optimization routine, which calls an objective function program that computes $\tilde{\mathbf{x}}^T \mathbf{P} \tilde{\mathbf{x}}$ using the method described in the previous section.

$$\mathbf{P} = \begin{bmatrix} \omega & 0 & 0 & 0 \\ 0 & 1 & 0 & 0 \\ 0 & 0 & 0 & 0 \\ 0 & 0 & 0 & 0 \end{bmatrix}.$$

was chosen as the weighting matrix, since the effect of the mean position and velocity error, as well as oscillation, are captured by the first two state values, two non–zero

entries in $\mathbf{P}$ are sufficient. `fmincon.m` returns the timings t_i that result in a minimum value of the objective function. Once this computation is complete, `lsim.m` can be used to determine the state history of the flexible system to the input $u(t)$ during the entire sample k. The value of the state at the end of the sample is passed to the subsequent iteration and the process is repeated until some specified number of samples has been completed.

Because the gain of $G(z)$ is relatively high, simply quantizing based on consecutive integers around $\overline{u}$ does not truly demonstrate the quantization effects inherent in a device such as an array of cellular actuators. To achieve a more drastic quantization effect, each time $\overline{u}$ is computed, it is divided by some integer value Q representing the true quantization effect relative to the physical range of the controller, then quantized to consecutive integers. The resulting command is then multiplied by Q to scale it back up before simulation.

In this implementation, the reference model used to calculate $\tilde{\mathbf{x}}$ and the flexible system are simulated independently, i.e. state feedback from the flexible system is not fed to the simulation of the reference model[1]. The reference model has no knowledge of disturbances or oscillation in the system. Because of this, the fictitious discrete time control input used to simulate the reference model may vary from $\overline{u}$. However, this is permissible, because the fictitious control input is not actually controlling the flexible system. The output of the reference model is only used to design the *Intersample* routine for that sample. The error that is used to calculate $\overline{u}$ is based on the actual flexible system's state feedback, and it is this controller that has the capacity to reject low-frequency disturbances.

Figures 67 and 68 shows the model reference control input, $\overline{u}(k)$, the PWM signal used to generate $u(t)$, and $u(t)$ with $\omega = 45$ rad/s, $Q = 32$, and $m = 5$. A non–zero initial condition, $\mathbf{x} = [\ 0.05\ 0\ 0\ 0\ ]^T$ is given to induce oscillation in the system and

[1]This can be thought of as two copies of $G(z)$

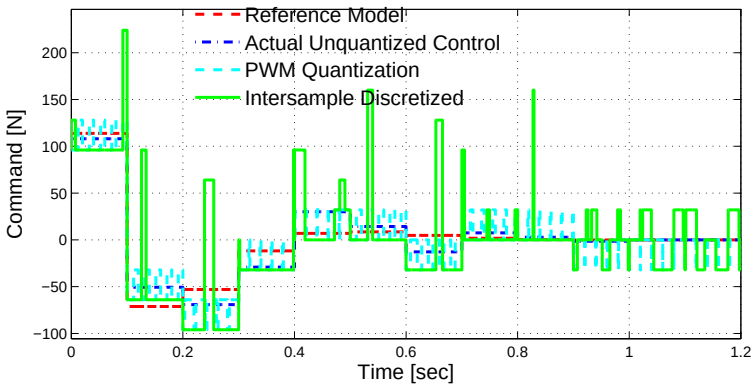

Figure 67: Control commands

represent the effect of a disturbance. Figure 69 a, b, and c show block diagram representations without quantization, PWM discretization, and intersample discretization based on a PWM candidate function, respectively. The response is shown in Figure 70 and the difference from the reference model is shown in Figure 71. This amplitude of oscillation, relative to travel distance, is on the order of that seen in a single cellular actuator when it is given a step input. The intersample discretization method is able to reduce this oscillation to near zero in 6 sample periods. Figures 67 - 71 used MatLab's `expm.m` command to compute the various state transition matrices. When the accuracy of the approximation is reduced, the response deteriorates. Figure 72 shows the response when only a quadratic approximation of $\mathbf{e}^{\mathbf{A}t}$ is used. in some cases, the response can be improved when a low order approximation is used by increasing the number of impulses.

Table 15 shows how the RMS error varies with the accuracy of the approximation of $\mathbf{e}^{\mathbf{A}t}$ and the number of impulses ($\omega = 45$ rad/s, $Q = 32$, $\mathbf{x} = [\ 0.05\ 0\ 0\ 0\ ]^T$ at $t = 0$). In general, a more accurate approximation and more pulses (or higher PWM frequency) gives superior performance, but there are exceptions. Increasing the order of the approximation by 1 or increasing m by 1 may not necessarily give superior performance.

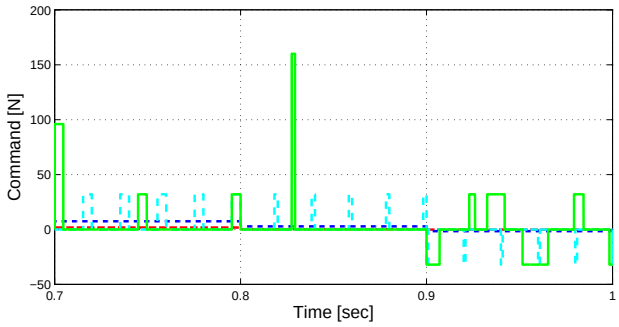

Figure 68: Close–up of control commands.

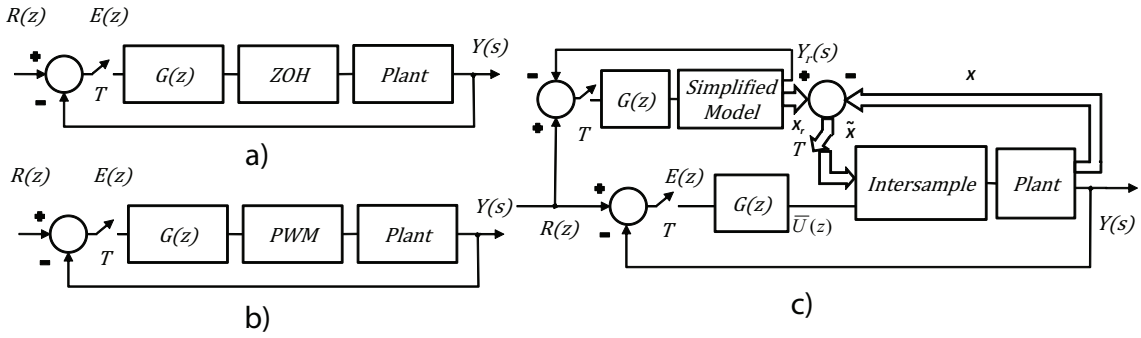

Figure 69: Block diagrams for various discretizations.

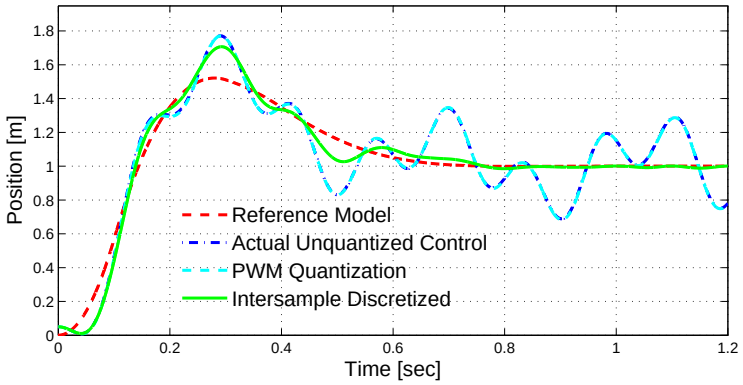

Figure 70: System response to control commands.

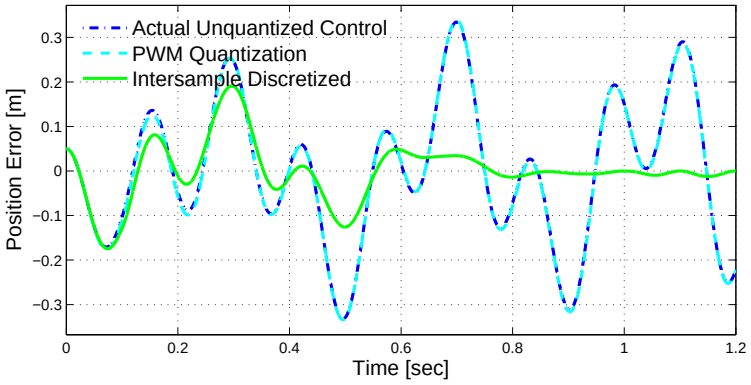

Figure 71: Position error w.r.t. reference model.

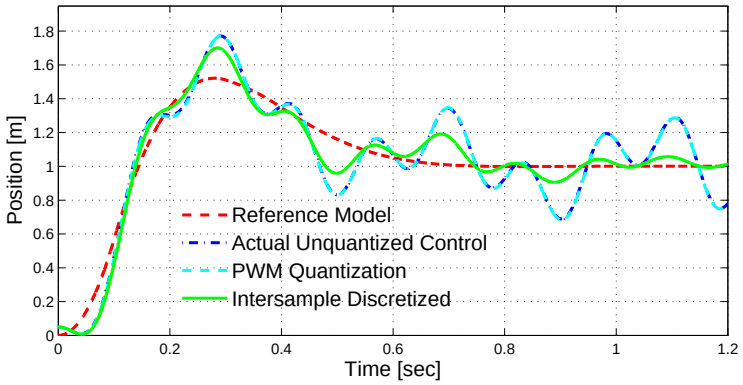

Figure 72: System response : quadratic approximation

Looking at Figure 67, it is obvious that for several samples, the optimization routine has driven all pulses to be coincident and $u(t)$ consists of one large pulse starting at some strategic time, and $u(t)$ for the remaining portion of the sample is merely $\lfloor \overline{u} \rfloor$. This occurs mainly when the state error is large; once convergence has been achieved, the pulses tend to spread out more. This makes intuitive sense; to stop the system from oscillating in a switching control system, the controller must apply a large impulse to the system when the velocity is highest. This has implications with regard to the quantization. If the amplitude of oscillation is high, a finer quantization does not allow the controller to apply as impulsive an input, and removing oscillation will take longer than if the quantization is coarse. For intersample discretization to achieve results in a reasonable amount of samples, the quantization has to result in

Table 15: RMS error for various approximations, m

$\mathbf{e}^{\mathbf{A}t}$ Appx.	Number of Pulses				
order	5	9	16	27	54
`expm.m`	0.0644	0.0567	0.0564	0.0572	0.0567
10	0.0654	0.0598	0.0598	0.0571	0.0577
4	0.0713	0.0940	0.0928	0.0638	0.1154
2	0.0888	0.0613	0.0605	0.0769	0.0667

step changes in $u(t)$ that are significant with respect to the size of changes in $\overline{u}$ and $\|\tilde{\mathbf{x}}(kT)\|$. Figure 73 shows the effect of increasing quantization on the convergence of J. Given plant and controller gains for this example, a $Q > 8$ is desired. This suggests that there may be some value in artificially making the quantization sensitivity coarser than that required by the physical realities of the actuator if $\|\tilde{\mathbf{x}}(kT)\|$ is large, and refining the quantization sensitivity toward the physical limit imposed by the actuator as the response converges. This is in some ways analogous to the "zooming" approach proposed in [82] with regard to quantized state feedback.

It should also be noted that given some non-zero initial condition, the amplitude of oscillation may not be reduced monotonically. The oscillation amplitude may "escape" somewhat for one or more samples, but the algorithm will subsequently reduce any increase in the size of the state, giving the appearance of a "pulsating effect" in the envelope.

As with any control system, there will always be a degree of uncertainty in the model used to design the controller. The ability of the intersample discretization to suppress oscillation deteriorates with uncertainty, but the algorithm would still be considered effective for a large range around the true natural frequency. Figures 74 and 75 show the response when the frequency used to design the discretization has been overestimated and underestimated by 15%, respectively. It can be seen that although the response deteriorates somewhat, the algorithm is still effective.

How well the intersample discretization algorithm performs depends greatly on

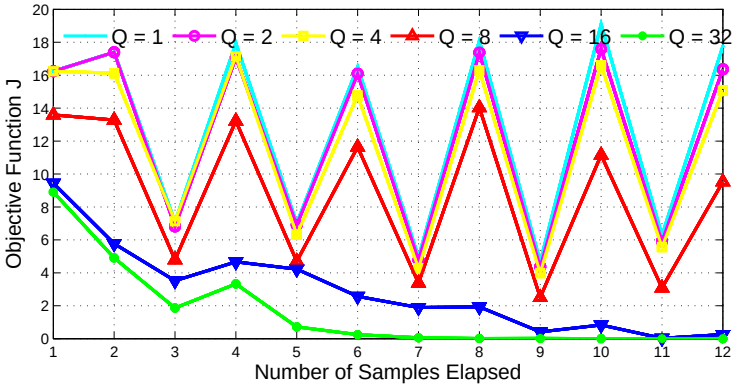

Figure 73: Objective function convergence

the frequency of oscillation. Figure 76 shows a case where the algorithm does not perform well, due to a problematic ω. In many cases, simply changing the number of pulses or changing the sampling frequency (either increasing or decreasing) allows the algorithm to find a better solution. In Figure 76, only the frequency was changed from the conditions in Figures 67 - 71; all other conditions were the same.

8.3 Intersample using an oscillatory mode as the reference model

The camera positioning mechanism, by virtue of the spring-like nature of the antagonistic pair of cellular actuators, does not posses a rigid body mode. In fact, the model described in Chapter 7 consists of a single lightly damped second order system with a relatively low natural frequency. Experiments show that the remaining vibrational modes do not contribute significantly to the response. However, it is not hard to imagine that design changes, such as adding additional degrees of freedom or adding additional cellular actuators in series to increase the travel angle could cause additional modes to become significant, and the methods of this chapter would come into play. This section therefore examines applying the method in section 8.2 to systems of this type. Intersample discretization will applied to the plant illustrated in Figure 77.

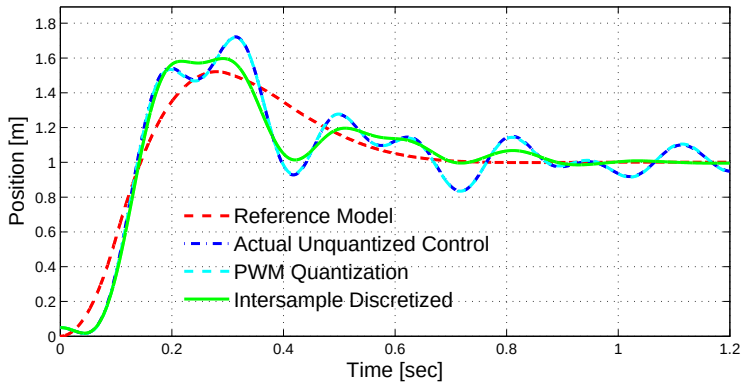

Figure 74: System response, ω 15% below modified value

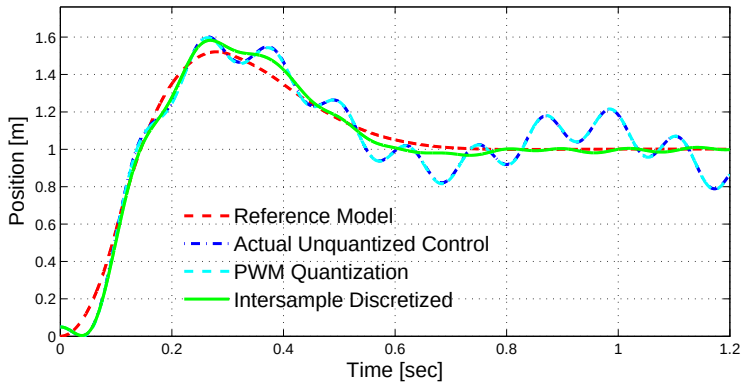

Figure 75: System response, ω 15% above modified value

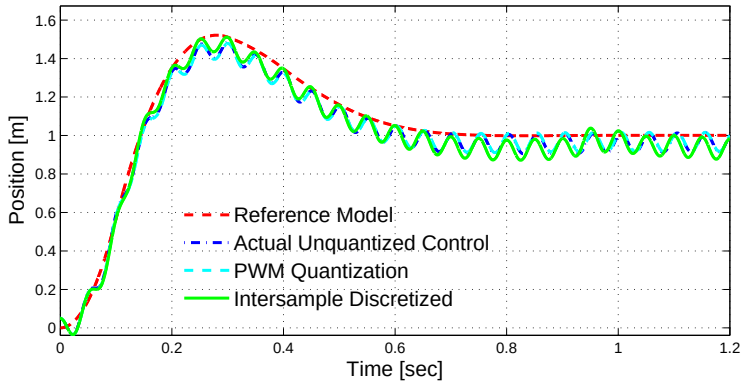

Figure 76: System response $\omega = 125$ rad/s

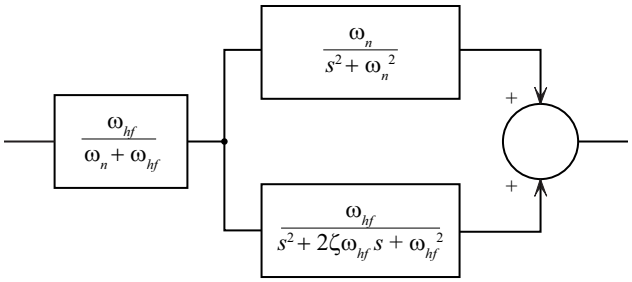

Figure 77: Hypothetical camera positioner dynamic model: single-mode reference model plus a high frequency lightly damped mode. The constant at the input is to make the DC gain of the full model equal to the reference model.

8.3.1 Plant model and discrete time controller

Take then as the reference model the undamped second order system:

$$G_r(s) = \frac{\omega_n}{s^2 + \omega_n^2} \tag{96}$$

with $\omega_n = 20\pi$ chosen for simplicity. With a little care, a discrete time compensator can be designed that gives the reference model a satisfactory response:

$$G(z) = 167\frac{z^2 - 1.7z + 0.86}{z^2 - 0.64z - 0.36}, \tag{97}$$

with a sampling time of 0.01 s. The development then proceeds similarly to that in section 8.2. Assume then that the physical system has a second lightly damped mode above the Nyquist frequency [2]. The natural frequency of this mode will be denoted ω_{hf}. For this example, $\omega_{hf} = 150\pi$ and $\zeta = 0.01$ will be chosen, which lies between Nyquist frequency and the sampling frequency.

The full plant model (expressed in controllable canonical form) is:

[2]There must be some damping, otherwise the full system with the discrete time controller will be unstable. If the damping assumed in this mode is insufficient, the gain of $G(z)$ can be reduced

$$
\begin{aligned}
\dot{\mathbf{x}} &= \mathbf{A}\mathbf{x} + \mathbf{B}u \\
y &= \mathbf{C}\mathbf{x} + \mathbf{D}u \\
\mathbf{A} &= \begin{bmatrix} 0 & 1 & 0 & 0 \\ 0 & 0 & 1 & 0 \\ 0 & 0 & 0 & 1 \\ -\omega_n^2\omega_{hf}^2 & -2\zeta\omega_n^2\omega_{hf} & -(\omega_n^2 + \omega_{hf}^2) & -2\zeta\omega_{hf} \end{bmatrix} \\
\mathbf{B} &= \begin{bmatrix} 0 & \omega_n + \omega_{hf} & -2\zeta\omega_{hf} & 4\zeta^2\omega_{hf}^2 - \omega_n^3 - \omega_{hf}^3 \end{bmatrix}^T \\
\mathbf{C} &= \begin{bmatrix} 1 & 0 & 0 & 0 \end{bmatrix} \\
\mathbf{D} &= 0.
\end{aligned} \tag{98}
$$

Expressing the plant in controllable canonical form allows the choice of $\mathbf{w} = \mathbf{0}$.

8.3.2 Intersample discretization applied to the two-mode system

A reference command of a unit step is applied to two-mode plant. Choosing $Q = 32$ makes the quantization of this example system roughly equivalent to the quantization in the camera positioner's actuation, assuming that the maximum control effort required for this move uses most or all of the active units. For this example

$$
\mathbf{P} = \begin{bmatrix} 1 & 0 & 0 & 0 \\ 0 & \omega_{hf} & 0 & 0 \\ 0 & 0 & \omega_{hf}^2 & 0 \\ 0 & 0 & 0 & \omega_{hf}^3 \end{bmatrix}.
$$

was used with $m = 9$ pulses/sample. The control command is shown in Figure 78, with a close-up of a few samples in Figure 79. The response is shown in Figure 80, and the position error evolution of intersample discretization is compared to PWM and the unquantized control applied to the full system in Figure 81. Once again,

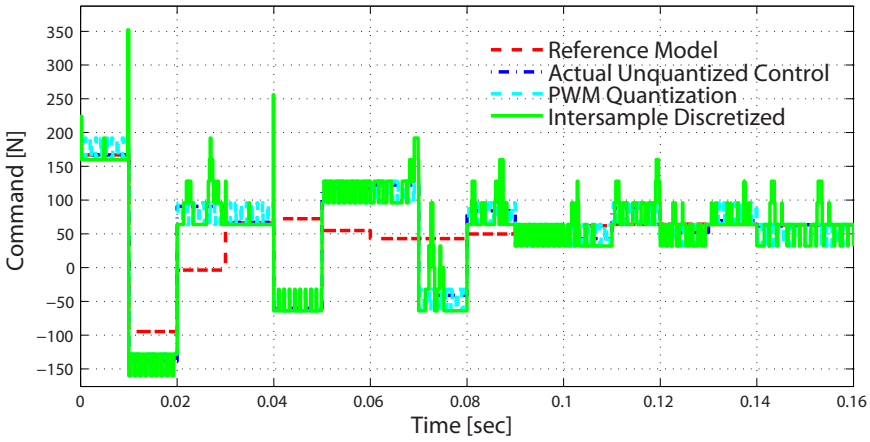

Figure 78: Control commands: two-mode system

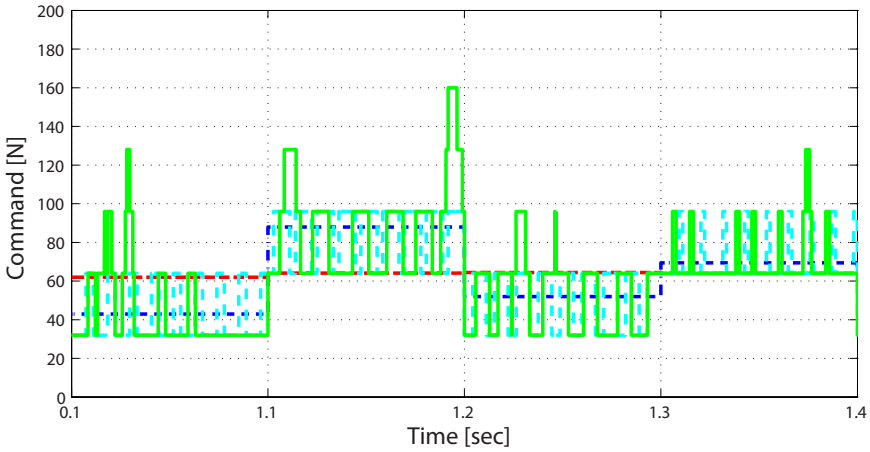

Figure 79: Close-up of control commands : two-mode system

the intersample discretization is able to reduce the amplitude of oscillation quite a bit within the settling time of the reference model. The PWM discretization does nothing to reduce oscillation. There is some residual oscillation in the intersample discretization response. The amplitude of this oscillation can be reduced by using a finer quantizer, but the response will in general take longer to converge.

8.4 Summary

This chapter has addressed a feedback control algorithm for cellular actuator driven devices, such as the biologically inspired camera positioner. The flexible nature of the actuation leads to a number of lightly damped high frequency resonances. The

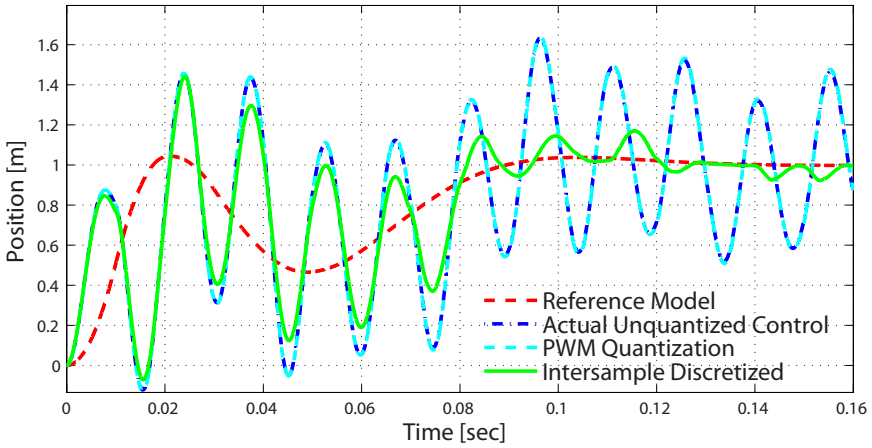

Figure 80: Two mode closed-loop step response

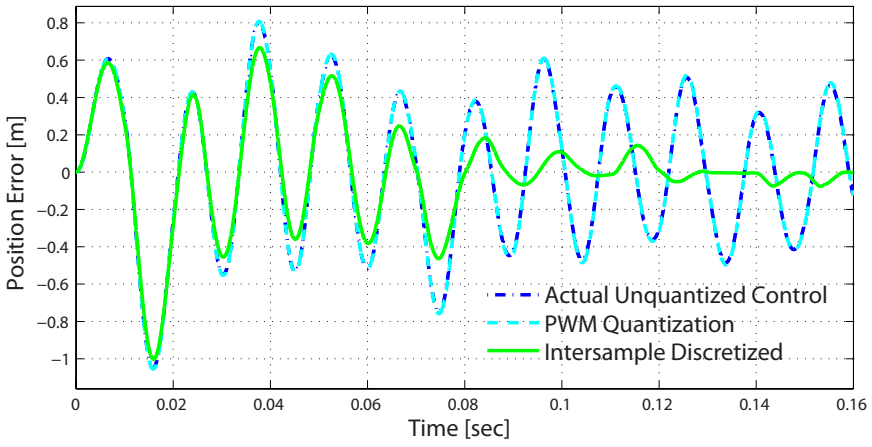

Figure 81: Position error

number of inputs are coarse enough that quantization effects in amplitude need to be considered. The control architecture designs a discrete time controller for a lower-order reference model and determines switching patterns among the near neighbors of the discrete control input so that the full system's response approaches that of the reference model under traditional discrete time control.

This chapter has proposed a control methodology that takes quantization effects into account and uses optimal switching times to actively damp oscillatory modes above the Nyquist frequency. By choosing a PWM signal as a candidate function and modifying the start times of each pulse, so that each individual pulse has some optimal, arbitrary switch timing, the algorithm can suppress oscillation generated by the natural response to the command itself, as well as disturbances from the environment. Simulations show that oscillation amplitude is substantially reduced within a few sampling periods.

CHAPTER IX

CONCLUSION AND SUGGESTIONS FOR FUTURE WORK

This chapter presents a conclusion to the work conducted in this thesis. First, the contributions to various areas are summarized. Finally, some suggestions are made regarding future directions of research related to this work.

9.1 Concluding remarks

Traditional robotic systems have a single actuator per degree of freedom, each with an analog input. This presents a stark contrast when compared to biological motion systems, which operate under a completely different paradigm. Biological systems inherit remarkable properties from their quantized, flexible actuation. Robotic systems that operate under this new paradigm promise to extend the biological advantages of adaptability and robustness to failure, greater simplicity in control interface, and better operation in unstructured environments to robots. To this end, researchers have proposed the idea of *cellular actuation*, namely compact, modular, flexible units that are *recruited*, or selectively activated in an on-off manner to produce motion. This thesis presents a mathematical understanding of these phenomena crucial to making robots that operate under this paradigm a reality, and demonstrates them through relevant simulation and experimental examples, most notably an antagonistically driven camera positioning mechanism.

Piezoelectric ceramic is a promising active material for actuators of this type, but the force-displacement performance point needs to be shifted in order to use this in a robotics context. Nested compliant hierarchical strain amplifiers can be used to shift

this performance point. Examples of nested hierarchical mechanisms have existed prior to the work conducted in this thesis, but this represents the first work presenting a systematic method of designing nested strain amplifiers and understanding their behavior. Chapters 3 and 4 reveal that analysis based on multiplicative amplification of idealized hinged rigid rhomboids is overly optimistic and a more adequate understanding including the compliance in nested rhomboidal hierarchies is presented. The two-port network circuit model with mechanical analogies is uses to describe the input-output behavior. In two-port network models, input-output behavior can be elegantly described by three immittance parameters.

Chapter 3 has presented a formulation that can be used to calculate the immittances of a given stage in a hierarchical mechanism. In this way, the two-port model can be calculated directly from the geometry, something that was not possible with previous lumped parameter models with no connection to physical characteristics. Chapter 4 has revealed interesting properties that emerge from the nested hierarchical structure. Paramount is that the stiffness of the actuator as perceived by the environment depends most heavily on the outermost layers. It also showed mathematically that for a nested mechanism to be successful, the outermost layer must be very compliant when compared to the layers before it.

Chapter 5 discussed the practical aspects involved in designing nested amplification mechanisms of this type and enumerated some archetypal constraints. It compares relative merits of two-layer and three-layer designs and finally demonstrated a systematic approach to set the various geometric properties of a three-layer actuator based on design specifications derived from the performance of the human oculomotor system. One important fact noted in Chapter 5 is that the immittance parameters for a given layer are coupled in the geometric parameters. Since the immittances cannot be set independently of one another for a given layer, this provides powerful motivation for the use of nested hierarchical mechanisms, namely that the immittances of

each stage in the hierarchy are largely independent from those of the rest.

Each level in the hierarchy of an actuator of this type will contain a series or parallel combination of the units below it. For this reason, each actuator will have a number of piezoelectric stacks. Chapters 6, 7 and 8 expound upon the quantized nature of the control when each piezoelectric stack is viewed as an on-off unit, in order to capture the benefits of the biological concepts of motor units and avoid the effects of hysteresis in piezoelectric materials. This thesis treats the plant as a system that can only accept integer-valued commands. Because of the compliance of the individual strain amplifying units, systems using actuators of this type will tend to have lightly damped resonant modes. Chapters 6, 7 and 8 provide several methods to improve the dynamic performance with appropriate recruitment strategies for activating the various inputs in time.

Chapter 6 presented a method for point-to-point motion with zero residual vibration. The commands produced make use of integer-valued control inputs only and thus can be implemented by quantized actuators of this type. This method can be used on a system with an arbitrary number of modes, provided that a solution to a system of nonlinear equations can be found. There are an infinite number of commands that can produce this result, but the command of most interest is the "minimum switching" command, which tends to be more robust to modeling errors, has smoother transients, and uses the least energy. The method is shown to reduce oscillation in both significant modes of a second order system.

Chapter 7 applied these concepts to the camera positioner designed in Chapter 5. It is determined that with only a single "cell" per side, the camera positioner has only a single significant mode and thus the calculation of switching commands is greatly simplified. Firmware is developed to implement arbitrary move sequences provided by a user

Although it was found not to be directly applicable to the camera positioner,

Chapter 8 presents a closed-loop technique that discretizes a continuously valued discrete time control command to its near neighboring integers during the sample in such a way that oscillation is minimized. Simulation results show that the trajectory converges within a few samples whereas PWM commands continue to oscillate.

9.2 Suggestions for future work

Although this thesis has laid a foundation for the study of muscle-like actuation, it has by no means exhausted all lines of inquiry in this area. In fact, many interesting questions emerge in light of the discoveries presented here. A few of the most prominent are listed here:

9.2.1 Nested compliant strain amplifying mechanisms

1. The camera positioning mechanism used strain amplifying mechanisms that had distributed compliance. It would be interesting to compare the relative merits of using distributed compliance and localized compliance. Given manufacturing constraints, one may perform better than the other.

2. This thesis used piezoelectric ceramic as the active material. Future work could examine the use of other materials such as electroactive polymers or shape memory alloy.

3. One key assumption in this analysis was that all active units were of the same size and produced the same force. This is not the case in muscle systems; motor units have different sizes and capabilities. The assumption of uniformity could be relaxed and the analysis extended. The two-port formalism will still be useful in this case, however, internal coupling between the units will need to be considered to a greater degree.

4. The immittance matrices derived in this thesis are for the static case. Dynamic two port models could be derived with transfer functions for each immittance

parameter. It is not immediately clear whether the theorems presented in Chapter 4 would hold in more general metric spaces composed of transfer function elements. Convenient assumptions regarding mass distribution will be critical to any analysis of this type.

9.2.2 Control of systems with quantized actuation

1. The method of Chapter 6 is focused on finding the point to point command that uses the smallest number of switches. If this stipulation is relaxed, using additional impulses it is possible to add constraints on robustness to variations in frequency (enforcing that $\partial A_r/\partial\omega = 0$) or constraints on the transient such as was performed in [61] for continuously variable inputs.

2. In this thesis, the plant is expressed in terms of modal coordinates. As these devices scale in complexity, if closed loop control is to be applied, the sensing and estimation problem will become very important. Naturally the most attractive idea is that of "self-sensing," where the piezoelectric stacks themselves are used to reconstruct the system state. Some preliminary steps have been taken in this regard, but are complicated by nonlinearity in the model [98]. Most existing works on self-sensing are static and involve integration of the current [99–101]. There are even fewer works on sensing for nested mechanisms; the few that exist are very recent [99, 102]. Even once good sensing technology is achieved, the estimation problem for nested compliant mechanisms is both non-trivial and interesting.

3. Since the camera positioning mechanism presented in this thesis has only a single "cell" per side, the higher modes do not have a significant contribution. However, for larger displacement mechanisms with longer chains of cells, higher frequency modes will have greater prominence. Some of these may not be observable from the output. Applying the methods of Chapter 8 may help to

reduce the amplitude of vibration in these systems.

APPENDIX A

TWO-PORT NETWORK CIRCUIT MODELS

Fig. 82 illustrates a two-port network with variable voltage and current at each port. Of the four input-output quantities of interest, V_1, V_2, I_1, I_2, any two, (e.g. both currents) can be designated as inputs, making the other two quantities (e.g. both voltages) outputs. The input-output relationship is then described by a 2×2 *immittance* matrix. If the four elements of the immittance matrix are known for a single choice of inputs, the immittance matrices for all remaining input-output relationships can be expressed as functions of the elements of this first immittance matrix.

For example, if the currents, I_1 and I_2 are chosen as inputs, then the voltages, V_1 and V_2, are outputs, then the immittance matrix elements are impedances, and the relationship is as follows:

$$\begin{bmatrix} V_1 \\ V_2 \end{bmatrix} = \begin{bmatrix} Z_{11} & Z_{12} \\ Z_{21} & Z_{22} \end{bmatrix} \begin{bmatrix} I_1 \\ I_2 \end{bmatrix} \tag{99}$$

If $Z_{21} = Z_{12}$, then the network is termed a *reciprocal* two-port network [28, 30]. If

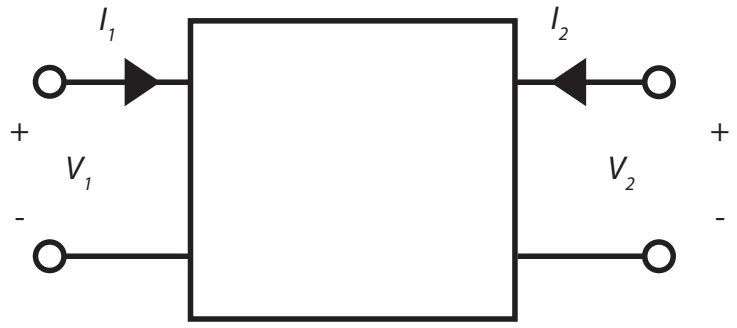

Figure 82: Two-port electrical network model

$Z_{21} \neq 0$ and $Z_{12} \neq 0$, the network is termed a *bilateral* two-port, that is, changes in port 2 affect port 1, and vice versa [30]. Various relationships for interconnections of two-port networks have derived, which can be found in [28], greatly facilitating the analysis of complicated interconnected networks. For this reason, two-port networks have found great utility in the field of telemanipulation [30, 31].

APPENDIX B

TWO PORT EXPRESSIONS FOR A GENERAL OCTAGONAL COMPLIANT MECHANISM WITH A SINGLE THICKNESS

The various C_{ij} derived by solving the force-displacement relations using Castigliano's theorem are as follows:

$$
\begin{aligned}
C_{11} = -\csc^2\left(\frac{\theta}{2}\right)\sec^4\left(\frac{\theta}{2}\right)\big(&96d^4\cos(\theta) - 64d^4\cos(2\theta) \\
&+ 32d^4\cos(3\theta) - 64d^4 - 64d^3h\sin(\theta) \\
&- 64d^3h\sin(3\theta) - 64d^3w\sin(\theta) - 64d^3w\sin(3\theta) \\
&+ 64d^2t^2\cos(2\theta) - 54.144d^2t^2\cos(3\theta) \\
&+ 11.072d^2t^2\cos(4\theta) + 16d^2\cos(\theta)\left(3.384t^2 + 3w^2\right) \\
&- 75.072d^2t^2 - 48d^2w^2\cos(3\theta) - 86dht^2\sin(\theta) \\
&+ 11.072dht^2\sin(2\theta) + 34dht^2\sin(3\theta) - 5.536dht^2\sin(4\theta) \\
&- 6dht^2\sin(5\theta) + 2dht^2\sin(7\theta) - 129.216dt^2w\sin(\theta) \\
&+ 11.072dt^2w\sin(2\theta) + 43.072dt^2w\sin(3\theta) \\
&- 5.536dt^2w\sin(4\theta) - 48dw^3\sin(\theta) + 16dw^3\sin(3\theta) \\
&- 5h^2t^2\cos(\theta) + 14h^2t^2\cos(2\theta) + 5h^2t^2\cos(3\theta) \\
&- 4h^2t^2\cos(4\theta) - h^2t^2\cos(5\theta) + 2h^2t^2\cos(6\theta) \\
&+ h^2t^2\cos(7\theta) - 12h^2t^2 - hw\cos(\theta)\left(18.536t^2 + 8w^2\right) \\
&+ 2hw\cos(2\theta)\left(20.536t^2 + 8w^2\right) + 18.536ht^2w\cos(3\theta) \\
&- 4ht^2w\cos(4\theta) - ht^2w\cos(5\theta) + 2ht^2w\cos(6\theta) \\
&+ ht^2w\cos(7\theta) - 39.072ht^2w + 8hw^3\cos(3\theta) - 16hw^3 \\
&- 2w^2\cos(\theta)\left(6.768t^2 + w^2\right) + 4w^2\cos(2\theta)\left(6.768t^2 + w^2\right) \\
&+ 13.536t^2w^2\cos(3\theta) - 27.072t^2w^2 + 2w^4\cos(3\theta) - 4w^4\big)
\end{aligned}
\tag{100}
$$

$$
\begin{aligned}
C_{21} = C_{12} = 2\big(&128d^4\csc^3(\theta) - 128d^4\csc(\theta) \\
&+ 384d^4\cot^2(\theta)\csc(\theta) - 512d^4\cot(\theta)\csc^2(\theta) \\
&+ 384d^3h\cot^2(\theta) + 1152d^3h\csc^2(\theta) \\
&- 512d^3(2h-w)\cot(\theta)\csc(\theta) - 1152d^3h - 12d^2h^2\cos^2(\theta) \\
&- 24d^2h^2\cos(\theta) + 9d^2h^2\cos(2\theta) \\
&+ 120d^2h^2\cot^2(\theta) + 258d^2h^2\csc^2(\theta) + 6d^2h^2\cos^2(\theta)\cot^2(\theta) \\
&- 24d^2h^2\cos(\theta)\cot^2(\theta) - 360d^2h^2\cot(\theta)\csc(\theta) \\
&- 249d^2h^2 - 541.44d^2t^2\sin(\theta) - 866.304d^2t^2\cot(\theta) \\
&+ 324.864d^2t^2\cos(\theta)\cot(\theta) + 64d^2\csc(\theta)\left(8.46t^2 - 6w^2\right) \\
&+ 64dht^2\cos^4(\theta) - 128dht^2\cos^3(\theta) + 128dht^2\cos^2(\theta) \\
&+ 32dht^2\cos(2\theta) + 56dht^2\cos(4\theta) + 384dht^2\sin^2(\theta)\cos(\theta) \\
&- 128dt^2(4.384h + 3.384w)\cos(\theta) - 24dht^2 - 384dhw^2 \\
&- 96h^2w^2 - 128ht^2(h+w)\sin(\theta)\cos^3(\theta) \\
&+128ht^2(h+w)\sin^3(\theta)\cos(\theta)\big) \quad (101)
\end{aligned}
$$

$$
\begin{aligned}
C_{22} = 2\Big(&512d^4\csc^2(\theta) - 2048d^4\cot(\theta)\csc(\theta) \\
&- 3072d^3h\cot(\theta) + 1024d^3(h+w)\csc(\theta) + \\
&192d^2h^2\sin(\theta) - 1440d^2h^2\cot(\theta) + 576d^2h^2\csc(\theta) \\
&+ 192d^2h^2\cos(\theta)\cot(\theta) + 1536d^2hw - 386.304d^2t^2\cos(\theta) \\
&+ 256d^2t^2\cot^2(\theta) + 768d^2t^2\csc^2(\theta) \\
&- 32d^2t^2\cos(\theta)\cot^2(\theta) - 992d^2t^2\cot(\theta)\csc(\theta) \\
&+ 98.304d^2t^2 + 85dh^3\sin(\theta) + dh^3\sin(3\theta) \\
&- 2d\cot(\theta)\left(115h^3 + 322.58ht^2 + 256t^2w\right) \\
&+ 4d\csc(\theta)\left(43h^3 + 120.756ht^2 + 112t^2w\right) \\
&+ 16d\cos(\theta)\cot(\theta)\left(5h^3 + 12.46ht^2 + 4t^2w\right) \\
&- dh\left(h^2 + 1.692t^2\right)\cos^4(\theta)\cot(\theta) \\
&+ 2dh\left(h^2 - 126.308t^2\right)\sin(\theta)\cos^3(\theta) \\
&+ 4dh\left(h^2 + 1.692t^2\right)\cos^3(\theta)\cot(\theta) \\
&- dh\cos^2(\theta)\cot(\theta)\left(96dh + 25\left(h^2 + 1.692t^2\right)\right) \\
&+ dh\left(3h^2 + 261.076t^2\right)\sin^3(\theta)\cos(\theta) \\
&- dh\sin(\theta)\cos(\theta)\left(96dh + 29h^2 + 305.068t^2\right) \\
&+ 768dh^2w + 416.972dht^2\sin(\theta) + 33.692dht^2\sin(3\theta) \\
&+ 384dht^2\sin(\theta)\cos^2(\theta) + 241.152dt^2w\sin(\theta) \\
&+ 32h^4 + 128h^3w + 16h^2t^2\cos(2\theta) - 28h^2t^2\cos(4\theta) \\
&+ 260.576h^2t^2 - 32ht^2(h+w)\cos^4(\theta) + 16ht^2w\cos(2\theta) \\
&-28ht^2w\cos(4\theta) + 388.576ht^2w + 128t^2w^2\Big) \quad (102)
\end{aligned}
$$

the denominator common to all terms is:

$$D_M = 6144\ E\ I\ \ (h + w - 2d(\cot\theta - \csc\theta))\,. \tag{103}$$

The immittances in stiffness matrix form (which is most useful for data sheets and the like) are obtained as follows:

$$s_1 = \frac{C_{11} D_M}{C_{11} C_{22} - C_{21}^2} \tag{104}$$

$$s_2 = \frac{C_{22} D_M}{C_{11} C_{22} - C_{21}^2} \tag{105}$$

$$s_3 = \frac{-C_{21} D_M}{C_{11} C_{22} - C_{21}^2} \tag{106}$$

APPENDIX C

DISCRETE SWITCHING PIEZOELECTRIC DRIVE CIRCUIT

The piezoelectric stacks at the heart of the Cédrat APA50XS actuators require a drive voltage of 150V. The circuit shown in Figure 83 supplies 150V to the piezoelectric stack when the pin labeled "Digital Input" is high. The exact circuit shown in the figure was used to drive the single-ended 6 input actuator in Chapter 6.

This circuit will drive only one piezoelectric stack, so a single instance must be provided for each stack. High voltage switching is accomplished by the Avago ASSR302C solid state relay, which has a much faster response time that mechanical relays. The circuit includes "break before make" delay protection so that the 150V rail will never be connected directly to ground through the ASSR302C bridge, as this condition will destroy the IC.

The full schematic for the discrete PZT switching drive board used in the biologically inspired camera positioner is in the following pages[1]. Each board can drive 4

[1]R7-10 were later changed to 4.7K accommodate a lower current capability of the NI 9041 switching module. Schematics show boards as they arrived from the manufacturer.

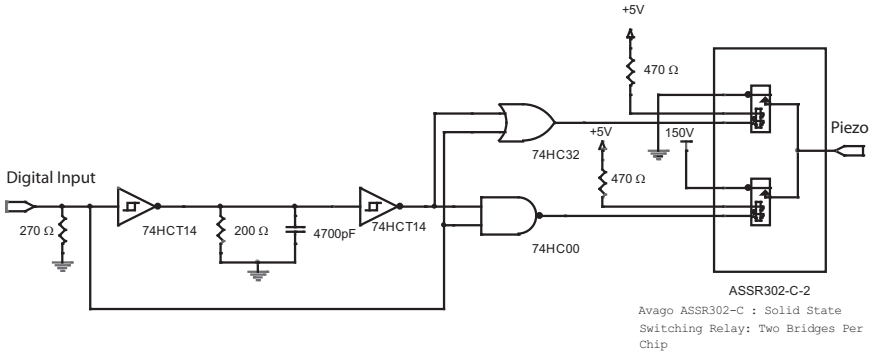

Figure 83: Piezoelectric dual-bridge switching drive circuit

piezoelectric stacks, so 8 boards were used in total to drive the camera positioner. Schematic capture and board layout design were performed using Novarm DipTrace software. PCB fabrication and board population were performed by Advanced Circuits, Aurora, CO. The version of the drive circuit shown in the schematic includes status LEDs for signal visualization and debugging purposes.

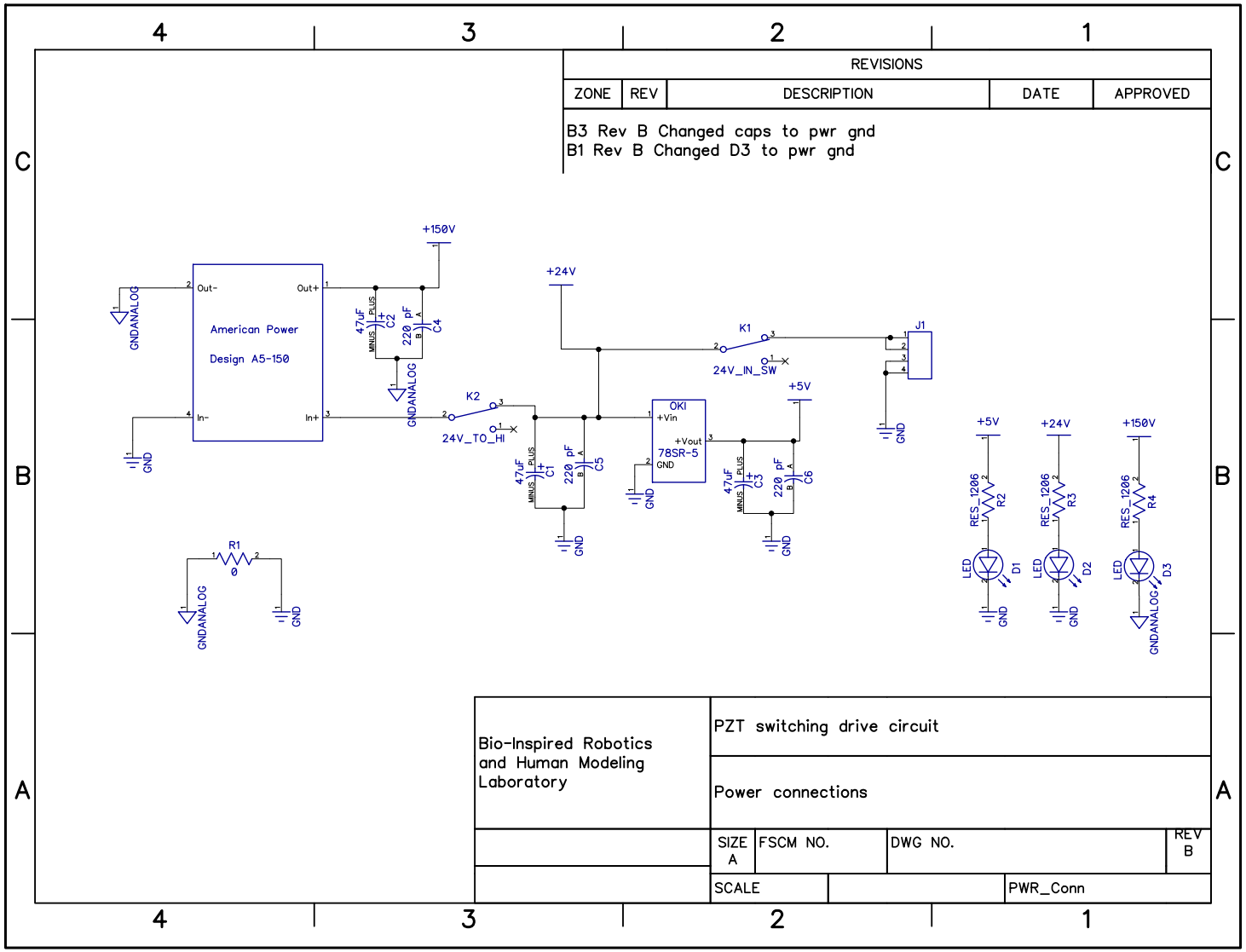
4
3
2
1
C
B
A
REVISIONS
ZONE
REV
DESCRIPTION
DATE
APPROVED
B3 Rev B Changed caps to pwr gnd
B1 Rev B Changed D3 to pwr gnd
+150V
+24V
+5V
American Power
Design A5-150
Out-
Out+
In-
In+
GNDANALOG
GND
47uF
220 pF
C2
C4
K1
K2
24V_IN_SW
24V_TO_HI
J1
OKI
+Vin
+Vout
78SR-5
C1
C3
C5
C6
R1
0
RES_1206
R2
R3
R4
LED
D1
D2
D3
Bio-Inspired Robotics and Human Modeling Laboratory
PZT switching drive circuit
Power connections
SIZE
A
FSCM NO.
DWG NO.
REV
B
SCALE
PWR_Conn

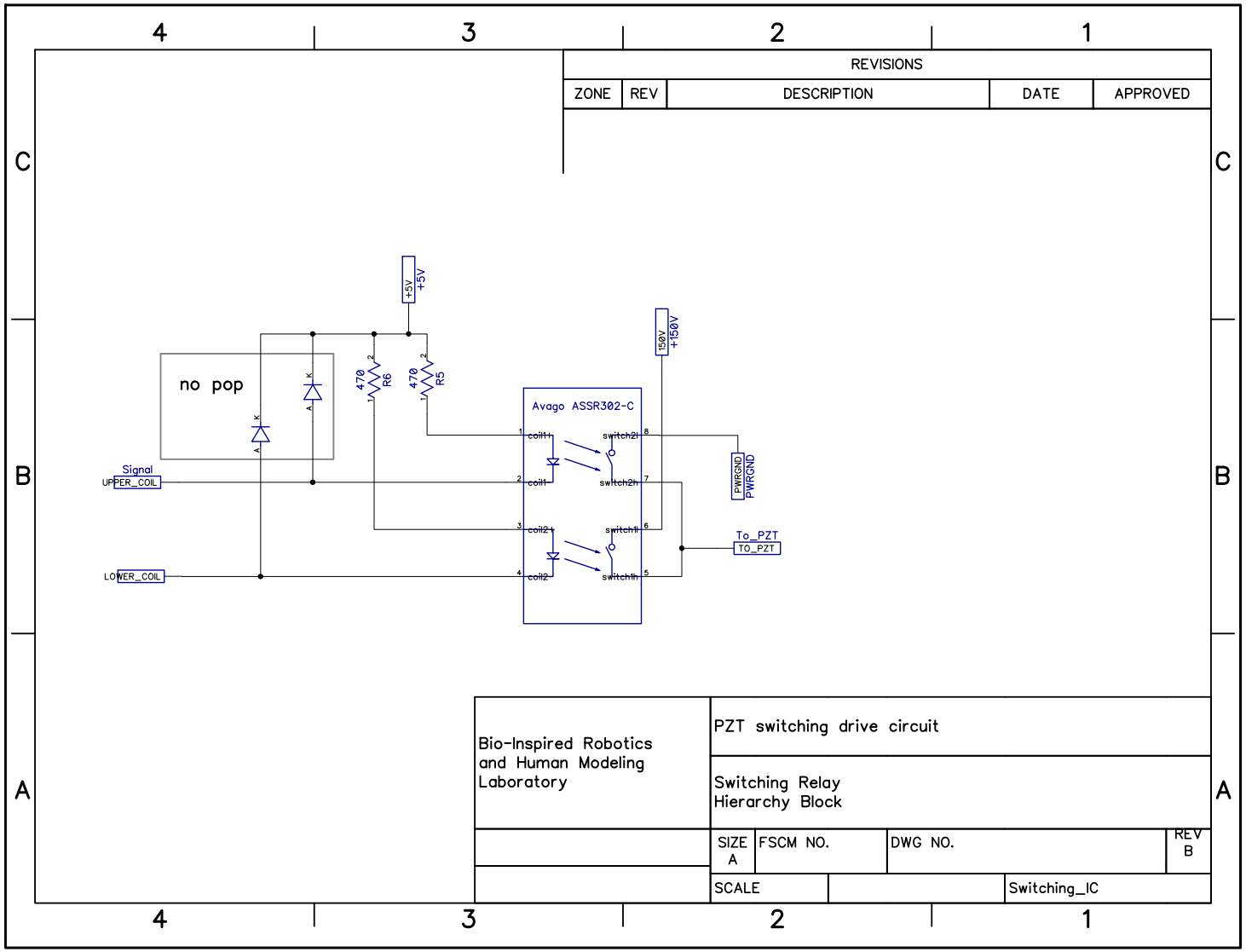
4
3
2
1
C
B
A
REVISIONS
ZONE
REV
DESCRIPTION
DATE
APPROVED
+5V
+5V
470
R6
470
R5
no pop
150V
+150V
Avago ASSR302-C
coil1+
coil1-
coil2+
coil2-
switch2l
switch2h
switch1l
switch1h
Signal
UPPER_COIL
LOWER_COIL
PWRGND
PWRGND
To_PZT
TO_PZT
Bio-Inspired Robotics and Human Modeling Laboratory
PZT switching drive circuit
Switching Relay Hierarchy Block
SIZE A
FSCM NO.
DWG NO.
REV B
SCALE
Switching_IC

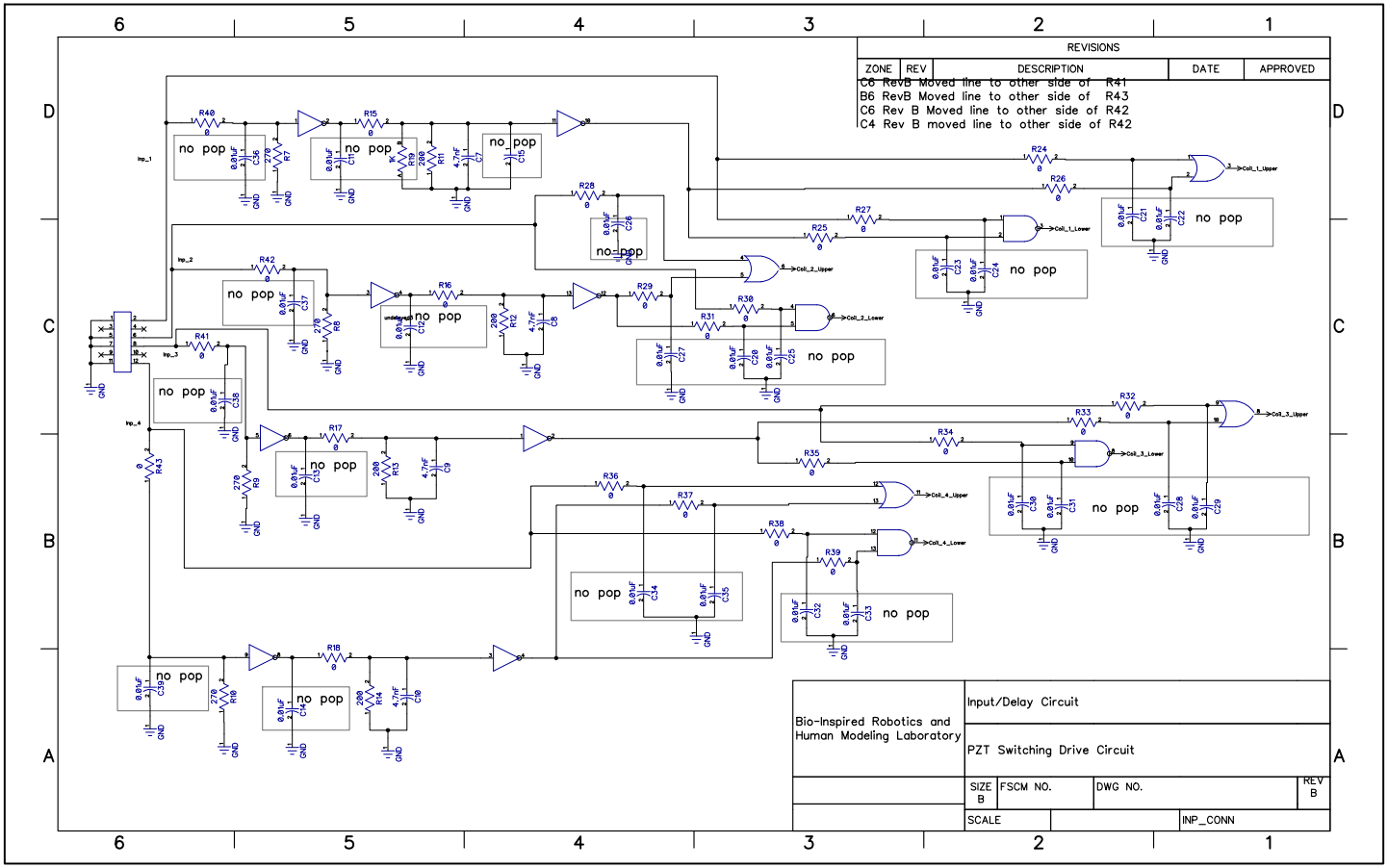
REVISIONS
ZONE | REV | DESCRIPTION | DATE | APPROVED
C6 RevB Moved line to other side of R41
B6 RevB Moved line to other side of R43
C6 Rev B Moved line to other side of R42
C4 Rev B moved line to other side of R42
no pop
Bio-Inspired Robotics and Human Modeling Laboratory
Input/Delay Circuit
PZT Switching Drive Circuit
SIZE B
FSCM NO.
DWG NO.
REV B
SCALE
INP_CONN

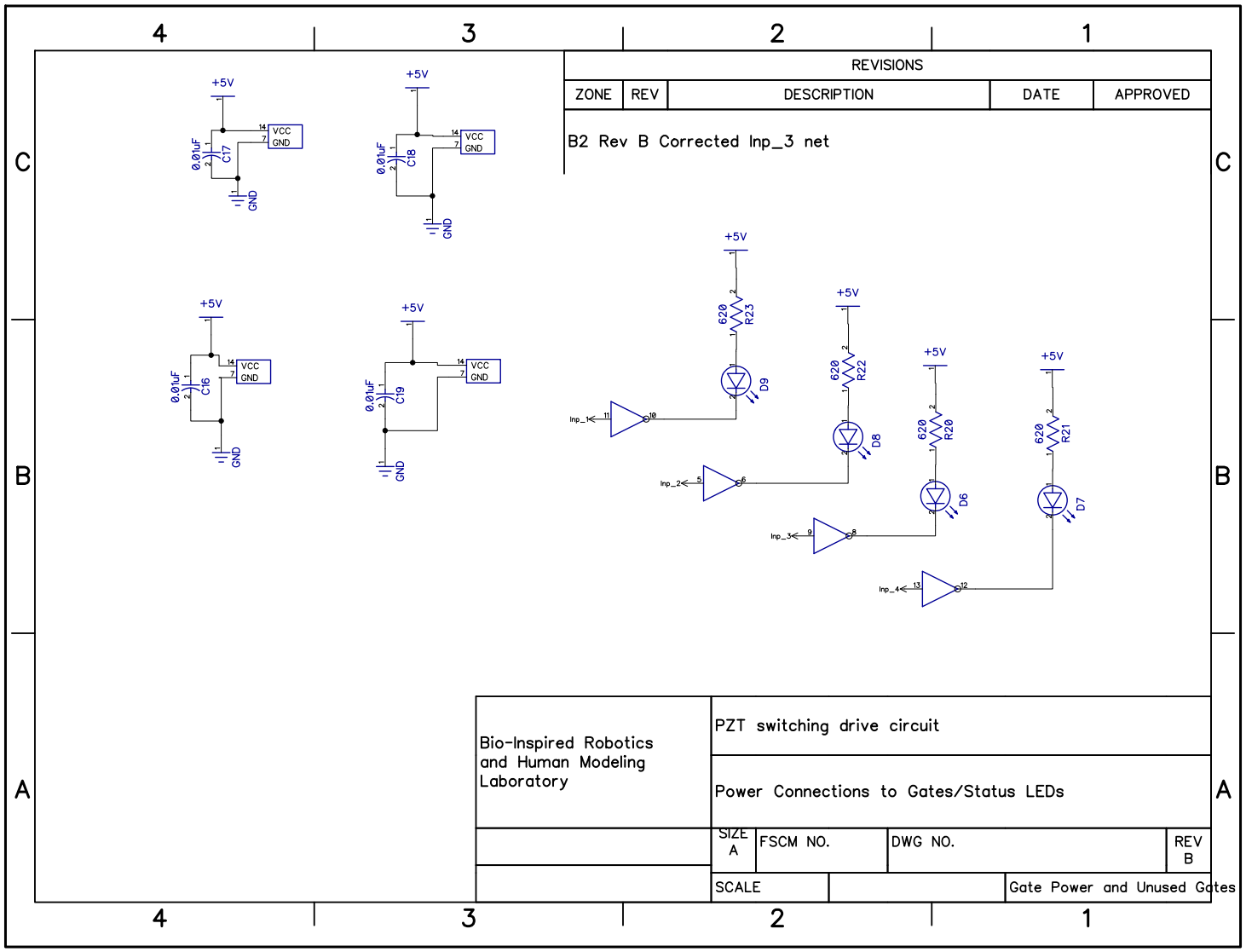
4
3
2
1
C
B
A
REVISIONS
ZONE
REV
DESCRIPTION
DATE
APPROVED
B2 Rev B Corrected Inp_3 net
+5V
VCC
GND
0.01uF
C17
C18
C16
C19
620
R23
R22
R20
R21
D9
D8
D6
D7
Inp_1
Inp_2
Inp_3
Inp_4
Bio-Inspired Robotics and Human Modeling Laboratory
PZT switching drive circuit
Power Connections to Gates/Status LEDs
SIZE
A
FSCM NO.
DWG NO.
REV
B
SCALE
Gate Power and Unused Gates

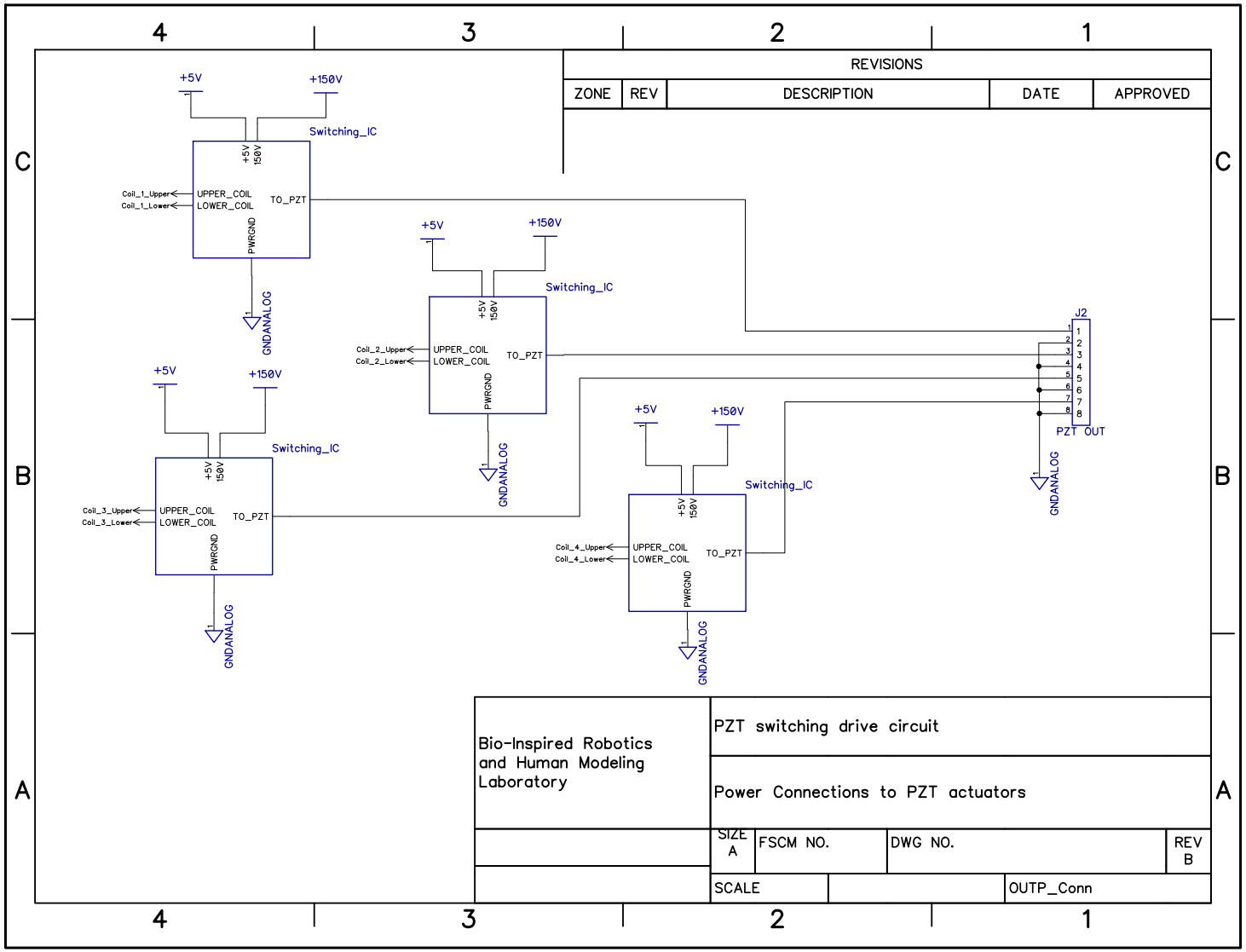
4
3
2
1
C
B
A
REVISIONS
ZONE
REV
DESCRIPTION
DATE
APPROVED
+5V
+150V
Switching_IC
+5V
150V
Coil_1_Upper
Coil_1_Lower
UPPER_COIL
LOWER_COIL
TO_PZT
PWRGND
GNDANALOG
Coil_2_Upper
Coil_2_Lower
Coil_3_Upper
Coil_3_Lower
Coil_4_Upper
Coil_4_Lower
J2
PZT OUT
Bio-Inspired Robotics and Human Modeling Laboratory
PZT switching drive circuit
Power Connections to PZT actuators
SIZE
A
FSCM NO.
DWG NO.
REV
B
SCALE
OUTP_Conn

APPENDIX D

MODE SHAPES FOR THE SINGLE-ENDED 6 INPUT ACTUATOR

Dassault Systems' COSMOSWORKS finite element software was used to analyze the vibrational modes of the 6 input, two layer cellular actuator with one end fixed and predict its natural frequencies and mode shapes. The mode shapes are shown here.

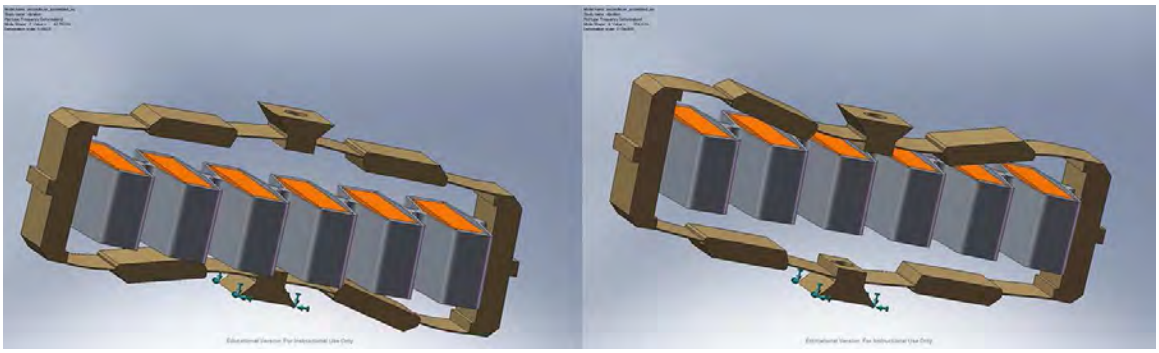

left: mode 1, right: mode 2

Figure 84: Principal vibrational modes of a cellular actuator

APPENDIX E

EXAMPLE SWITCHING ALGORITHM CALCULATION

Fig. 85 shows an example of the process conducted by `arb_novib_2f.m`. In this case, $y_g = 6$. The initial $\mathbf{A} = [\ 1\ 1\ 1\ 1\ 1\ ]$ results in a final position $\sum_{j=0}^{4} A_j$ of 5, not 6, so the pattern must be modified. Firstly, to satisfy (69), the vector $[\ 0\ 0\ 0\ 1\ 0\ ]$ is added to $\mathbf{A}$, causing the second to last impulse to have an amplitude of 2, which satisfies the desired y_g with a monotonically increasing command, so it is guaranteed to have the minimum number of switches. Next, `fsolve.m` attempts to find ϕ_j that satisfy (68). For purposes of illustration, say that in this case, `fsolve.m` does not return a valid solution. `fsolve.m` does not enforce $\phi_j < \phi_{j+1}$, so it is not strictly mathematically necessary to try different permutations of $\mathbf{A}$. However, from a numerical perspective, the presence of local minima and singularities may affect the reachability of a solution from a given set of initial conditions. Since the monotonic solution was not successful, one must introduce an amplitude of -1. This example, adds $[\ 1\ 0\ -2\ 0\ 1\ ]$ to $\mathbf{A}$. `fsolve.m` then attempts to find a solution. Say that it unsuccessful this time as well. The algorithm then has the choice of introducing an additional negative impulse by repeating the previous step, or increasing the absolute value of an existing negative impulse. In this example, suppose it chooses the latter, and adds $[\ 0\ 1\ -1\ 0\ 0\ ]$. Suppose that this time `fsolve.m` returns a solution. This must be checked to make sure that it does not violate (71). When the A_j are arranged in order of ascending ϕ_j, this is determined to be the case. This is then designated as the minimum switching command.

To implement this command, at $t = 0$ two PZTs would be turned on, then two of those remaining off are turned on at $t = \frac{\phi_1}{\omega_1}$. At $t = \frac{\phi_2}{\omega_1}$ two of the four turned on at

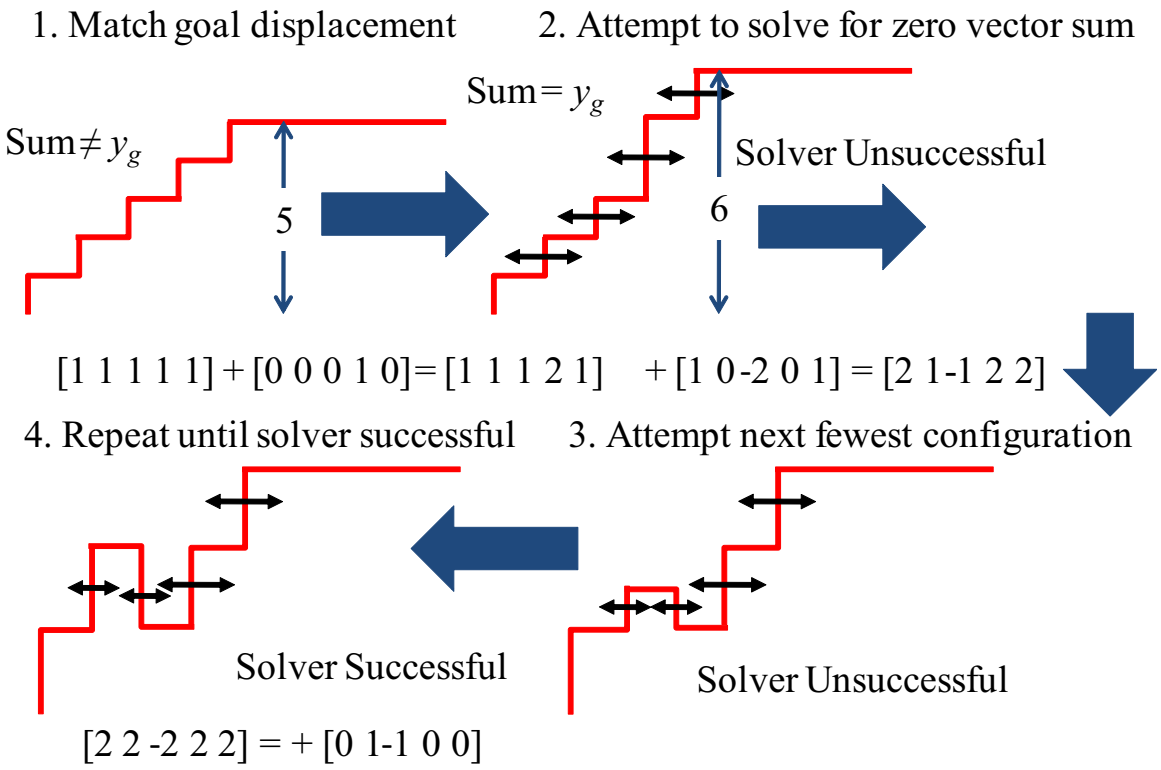

Figure 85: Illustration of `arb_novib_2f.m` operation

previous timings would be turned off. At this point there are two PZTs on and four off. Two of those off are turned on, and the remaining two turned on at the timings corresponding to ϕ_3 and ϕ_4 to complete the command. This results in a total of 10 "switches."

APPENDIX F

MSDSVS COMMANDS FOR ADDITIONAL MOVE LENGTHS FOR THE 6 INPUT CELLULAR ACTUATOR

In addition to the full stroke $y_g = 6$, commands for the 5 intermediate positions of the 6 input cellular actuator were developed. All On All Off control and MSDSVS are identical for $y_g = 1$. They are shown here.

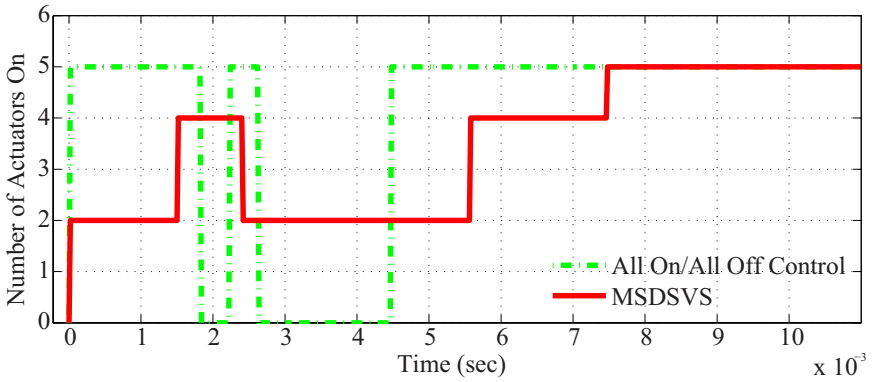

Figure 86: MSDSVS command: $y_g = 5$

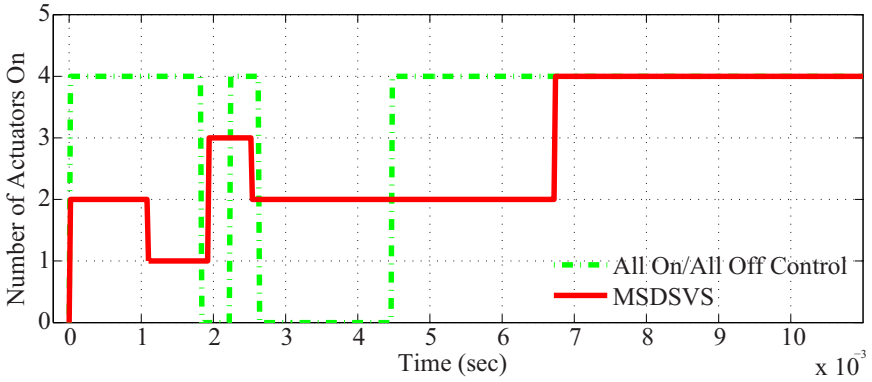

Figure 87: MSDSVS command: $y_g = 4$

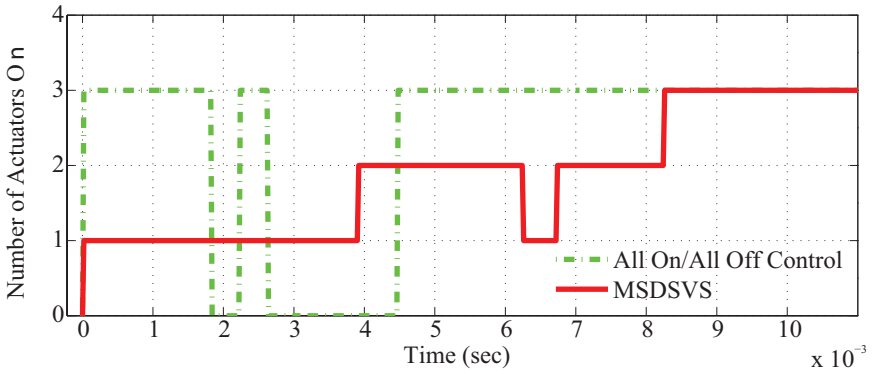

Figure 88: MSDSVS command: $y_g = 3$

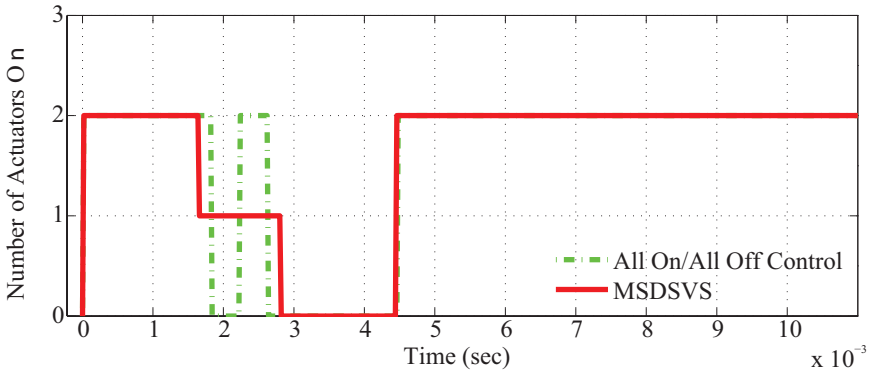

Figure 89: MSDSVS command: $y_g = 2$

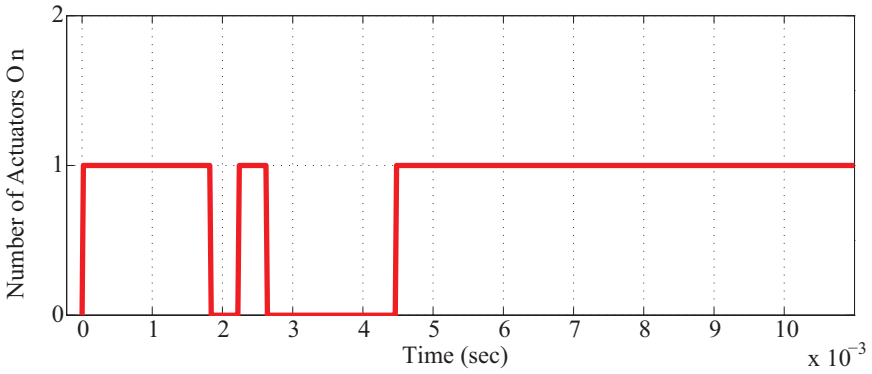

Figure 90: MSDSVS command: $y_g = 1$

APPENDIX G

CAMERA POSITIONER FIRMWARE

G.1 Architecture

The code implementing Minimum Switching Discrete Switching Vibration Suppression (MSDSVS) for the cellular actuator camera positioning mechanism consists of two main LabView VIs. One VI, `MSDSVS Realtime.vi` runs on the embedded processor of the cRIO-9118 module. `MSDSVS Realtime.vi` calls the subVi `Read MSDSVS Realtime.vi`. The other, `MSDSVS_FPGA_w_write.vi`, is converted to silicon and runs on the Field Programmable Gate Array (FPGA) backplane. The embedded processor code takes care of the user interface and identification of the appropriate MSDSVS pattern for a user-initiated move based on current and desired location, as well as some error checking. The algorithm for the embedded processor code uses the state machine architecture depicted in Figure 91.

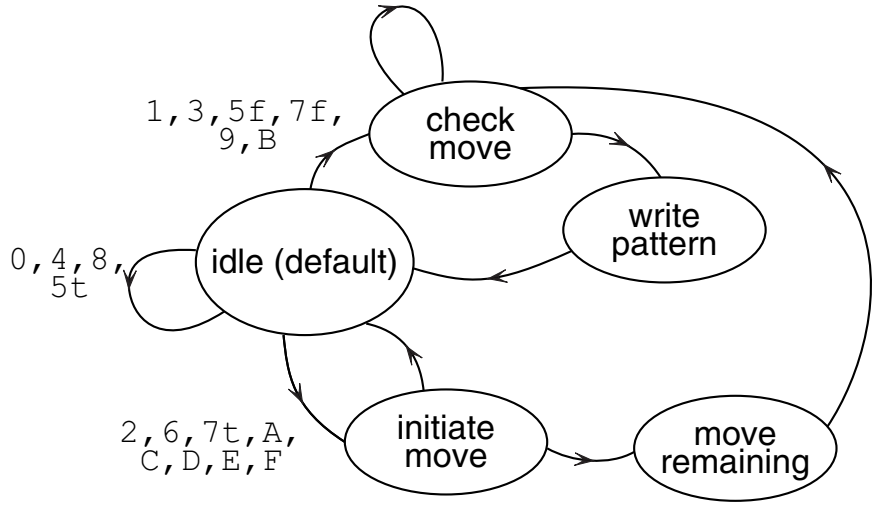

Figure 91: State diagram representation of embedded processor code for selecting MSDSVS Patterns

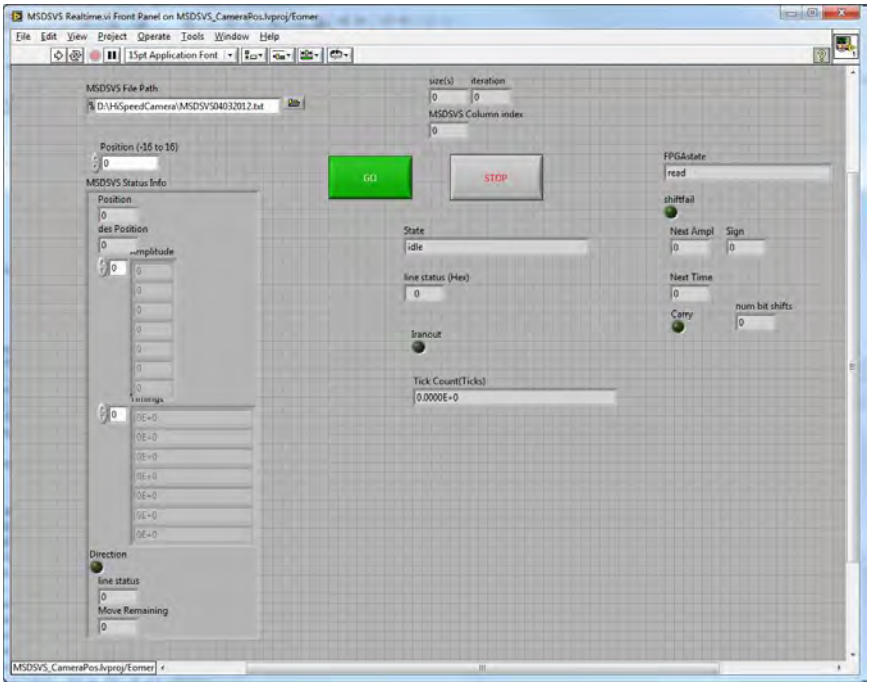

Figure 92: LabView front panel user interface

The MSDSVS pattern selected is written to FPGA memory. The FPGA then executes the command free from any supervisory control from the embedded processor. The FPGA uses the CompactRio onboard 40 MHz clock for precise timing.

G.2 User interface

The user can enter the desired location using the front panel interface shown in Figure 92 in the numeric control labeled "Position (0-16)." At this point the appropriate pattern is loaded to the FPGA to move to that location, but the move is not initiated. The user may change the destination any number of times without initiating the move. Once the user is sure of the destination, he or she can push the "Go" button to start the move. Any input during the move will have no effect. MSDSVS patterns are loaded from the text file in the box labeled "MSDSVS File Path." This master file may not be changed at runtime. Current position and MSDSVS pattern for the next intended move are displayed in the (cluster indicator) box labeled "MSDSVS Status Info." Remaining boxes are for debugging purposes only.

REFERENCES

[1] Jun Ueda, Thomas Secord, and Harry Asada. Large effective-strain piezoelectric actuators using nested cellular architecture with exponential strain amplification mechanisms. *IEEE/ASME Transactions on Mechatronics*, 15:770–782, 2010.

[2] Kenji Uchino. *Piezoelectric Actuators and Ultrasonic Motors*. Electronic Materials: Science and Technology. Kluwer Academic Publishers, 1997.

[3] Yingchun Zhang, Guangjun Liu, and J. Hesselbach. On development of a rotary – linear actuator using piezoelectric translators. *Mechatronics, IEEE/ASME Transactions on*, 11(5):647 –650, oct. 2006.

[4] Mary Frecker. Recent advances in optimization of smart structures and actuators. *Journal of Intelligent Material Systems and Structures*, 14:207–216, April-May 2003. "Structure-Actuator" section.

[5] S. Kota, K.-J. Lu, Z. Kreiner, B. Trease, J. Arenas, and J. Geiger. Design and application of compliant mechanisms for surgical tools. *ASME Journal of Biomedical Engineering*, 127:981–989, November 2005.

[6] Mostafa Abdalla, Mary Frecker, Zafer Gürdal, Terrence Johnson, and Douglas K Lindner. Design of a piezoelectric actuator and compliant mechanism combination for maximum energy efficiency. *Institute of Physics Smart Materials and Structures*, 14:1421–1430, November 2005.

[7] Shyh-Chour Huang and Wei-Liang Chen. Design of topologically optimal microgripper. In *IEEE International Conference on Systems, Man and Cybernetics*, 2008.

[8] M. Grossard, C. Rotinat-Libersa, N. Chaillet, and M. Boukallel. Mechanical and control-oriented design of a monolithic piezoelectric microgripper using a new topological optimization method. *Mechatronics, IEEE/ASME Transactions on*, 14(1):32 –45, feb. 2009.

[9] http://www.cedrat-technologies.com. web site, last accessed May 24, 2012.

[10] http://www.dynamic-structures.com/. web site, last accessed May 24, 2012.

[11] J.M. Paros and L. Weisbord. How to design flexure hinges. *Machine Design*, 37(27):151–156, November 1965.

[12] Nicolae Lobontiu, Jeffrey S. N. Paine, Ephrahim Garcia, and Michael Goldfarb. Corner-filleted flexure hinges. *Journal of Mechanical Design*, 123(3):346–352, 2001.

[13] Nicolae Lobontiu and Ephrahim Garcia. Analytical model of displacement amplification and stiffness optimization for a class of flexure-based compliant mechanisms. *Computers & Structures*, 81(32):2797–2810, 2003.

[14] Patrick Mottard and Yves St-Amant. Analysis of flexural hinge orientation for amplified piezo-driven actuators. *Smart Materials and Structures*, 18, 3 2009.

[15] Y. Tian, Bijan Shirinzadeh, D. Zhang, and Y. Zhong. Three flexure hinges for compliant mechanism designs based on dimensionless graph analysis. *Precision Engineering*, 34:92–100, 2010.

[16] Y. Tian, Bijan Shirinzadeh, D. Zhang, and Y. Zhong. Closed-form compliance equations of filleted v-shaped flexure hinges for compliant mechanism design. *Precision Engineering*, 34:408–418, 2010.

[17] Smita Bharti and Mary Frecker. Compliant mechanical amplifier design using multiple optimally placed actuators. *Journal of Intelligent Material Systems and Structures*, 18:209–217, March 2007.

[18] R.E. Newnham, A. Dogan, Q.C. Xu, K. Onitsuka, J. Tressler, and S. Yoshikawa. Flextensional "moonie" actuators. In *Ultrasonics Symposium*, pages 509–513. IEEE, 1993.

[19] Nicholas J Conway, Zachary J Traina, and Sang-Gook Kim. A strain amplifying piezoelectric mems actuator. *Institute of Physics Journal of Micromechanics and Microengineering*, 17:781–787, 2007.

[20] Jun Ueda, Thomas Secord, and H. Harry Asada. Design of pzt cellular actuators with power-law strain amplification. In *Proceedings of the IEEE/RSJ International Conference on Intelligent Robots and Systems*, pages 1160–1165, San Diego, CA USA, October 2007.

[21] Roger M. Enoka. *Neuromechanics of Human Movement*. Human Kinetics, fourth edition, 2008.

[22] Thomas W. Secord and H. Harry Asada. A variable stiffness actuator with tunable resonance for cyclic motion tasks. In *IEEE International Conference on Robotics and Automation*, page 176181, Kobe, Japan, May 2009.

[23] T.W. Secord and H.H. Asada. A variable stiffness pzt actuator having tunable resonant frequencies. *Robotics, IEEE Transactions on*, 26(6):993 –1005, 2010.

[24] Jun Hyung Kim, Soo Hyun Kim, and Yoon Keun Kwak. Development of a piezoelectric actuator using a three-dimensional bridge-type hinge mechanism. *American Institute of Physics Review of Scientific Instruments*, 74(5):2918–2924, May 2003.

[25] Erik Edward Steltz. *Redesign of the Micromechanical Flying Insect in a Power Density Context*. PhD thesis, University of California, Berkeley, May 2008.

[26] Neville Hogan. *Multiple Muscle Systems*. Springer-Verlag, 1990.

[27] Dean C. Karnopp, Donald R. Margolis, and Ronald C. Rosenberg. *System Dynamics Modelling and Simulation of Mechatronic Systems*. John Wiley and Sons, third edition, 2000.

[28] John Choma, Jr. *Electrical Networks: Theory and Analysis*. John Wiley and Sons, Inc., New York, 1985.

[29] José L. Pons. *Emerging Actuator Technologies, A Micromechatronic Approach*. John Wiley and Sons, 2005.

[30] G.J. Raju, G.C. Verghese, and T.B. Sheridan. Design issues in 2-port network models of bilateral remote manipulation. In *Robotics and Automation, 1989. Proceedings., 1989 IEEE International Conference on*, pages 1316 –1321 vol.3, May 1989.

[31] M. Zareinejad, S.M. Rezaei, A. Abdullah, and S. Shiry Ghidary. Development of a piezo-actuated micro-teleoperation system for cell manipulation. *The International Journal of Medical Robotics and Computer Assisted Surgery*, 5:66–76, January 2009.

[32] http://www.cameraturret.com/pan-tilt.htm.

[33] Albert J. Wavering, John C. Fiala, Karen J. Roberts, and Ronald Lumia. Triclops: A high-performance trinocular active vision system. In *Proceedings of the IEEE International Conference on Robotics and Automation*, volume 3, pages 410–417, 1993.

[34] Ricardo Beira, Manual Lopes, Miguel Praça, José Santos-Victor, Alexandre Bernardino, Giorigo metta, Francisco Becchi, and Roque Saltarén. Design of the robot-cub (icub) head. In *IEEE Conference on Robotics and Automation*, Orlando, May 2006. IEEE.

[35] Clément Gosselin and Jean-François Hamel. The agile eye: A high performance three-degree-of-freedom camera-orienting device. In *Proceedings of the IEEE International Conference on Robotics and Automation*, 1994.

[36] Clément Gosselin, Eric S. Pierre, and Martin Gagné. On the development of the agile eye. *IEEE Robotics and Automation Society Magazine*, 17(3):29–37, 1996.

[37] Clément Gosselin, Jaouad Sefrioui, and Marc J. Richard. On the direct kinematics of spherical three-degree-of-freedom parallel manipulators with a coplanar platform. *ASME Journal of Mechanical Design*, 116:587–593, 1994.

[38] Clément Gosselin, Jaouad Sefrioui, and Marc J. Richard. On the direct kinematics of spherical three-degree-of-freedom parallel manipulators of general architecture. *ASME Journal of Mechanical Design*, 116:594–598, 1994.

[39] Jaouad Sefrioui and Clément Gosselin. Étude et représentation des liex de singularité des manipulateurs paralleles sphériques à trois degrés de liberté avec actionneurs prismatiques. *Mechanism and Machine Theory*, 29(4):559–579, June 1994.

[40] Benjamin Bederson, Richard S. Wallace, and Eric L. Schwartz. Two miniature pan-tilt devices. In *IEEE Conference on Robotics and Automation*, 1992.

[41] Harley Truong, Samer Abdallah, Sebastien Rougeaux, and Alexander Zelinsky. A novel mechanism for stereo active vision. In *Proceedings of the Australian Conference on Robotics and Automation*. Australian Robotics and Automation Association, 2000.

[42] Benjamin Bederson, Richard S. Wallace, and Eric L. Schwartz. A miniature pan-tilt actuator: The spherical pointing motor. *IEEE Transactions on Robotics and Automation*, 10(3):298–308, June 1994.

[43] Gregory S. Chirikjian and David Stein. Kinematic design and commutation of a spherical stepper motor. *IEEE/ASME Transactions on Mechatronics*, 4(4):342–353, December 1999.

[44] Thomas Villgrattner and Heinz Ulbrich. Design and control of a compact high-dynamic camera-orientation system. *IEEE/ASME Transactions on Mechatronics*, to appear, 2010.

[45] J.D. Crawford, J.C. Martinez-Trujillo, and E.M. Klier. Neural control of three-dimensional eye and head movements. *Current Opinion in Neurobiology*, 13:655–662, 2003.

[46] Giorgio Cannata and Marco Maggiali. Models for the design of bioinspired robot eyes. *IEEE Transactions on Robotics*, 24(1):27–44, February 2008.

[47] Jong ung Choi, Brandon L. Rutter, Daniel A. Kingsley, Roy E. Ritzmann, and Roger D. Quinn. A robot with cockroach inspired actuation and control. In *Proceedings of the IEEE/ASME International Conference on Advanced Intelligent Mechatronics*, Monterey, CA, July 2005.

[48] Elaine N. Marieb. *Human Anatomy and Physiology*. Benjamin Cummings, 2001.

[49] Dr. C.G. Theod. Ruete. Ocular physiology. *Strabismus*, 7(1):43–60, January 1999.

[50] W. Haustein. Considerations on listing's law and the primary position by means of a matrix description of eye position control. *Biological Cybernetics*, 60(6):411–420, 1989.

[51] Qi Wei, Shinjiro Sueda, and Dinesh K. Pai. Biomechanical simulation of human eye movement. In *Biomedical Simulation*, volume 5958 of *Lecture Notes in Computer Science*, pages 108–118, Heidelberg, 2010. Springer Berlin.

[52] Douglas Tweed and Tutis Vilis. Implications of rotational kinematics for the ocularmotor system in three dimensions. *Journal of Neurophysiology*, 58(4):832–849, October 1987.

[53] S.B. Choi, C.C. Cheong, and H.C. Shin. Sliding mode control of vibration in a single-link flexible arm with parameter variations. *Journal of Sound and Vibration*, 179(5):737–748, 1995.

[54] A. De Luca and G. Di Giovanni. Rest-to rest motion of a two-link robot with a flexible forearm. In *Proceedings of ASME/IEEE International Conference on Advanced Intelligent Mechatronics*, volume 2, pages 929–935, 2001.

[55] Wayne Book. Controlled motion in an elastic world. *Transaction of the ASME Journal of Dynamic Systems, Measurement, and Control*, 115:252–261, 1993.

[56] Dragomir N. Nenchev, Kazuya Yoshida, Prasert Vichitkulsawat, and Masaru Uchiyama. Reaction null-space control of flexible structure mounted manipulator systems. *IEEE Transactions on Robotics and Automation*, 15(6):1011–1023, December 1999.

[57] Hwee Choo Liaw and B. Shirinzadeh. Neural network motion tracking control of piezo-actuated flexure-based mechanisms for micro-/nanomanipulation. *Mechatronics, IEEE/ASME Transactions on*, 14(5):517 –527, oct. 2009.

[58] Neil C. Singer and Warren P. Seering. Preshaping command inputs to reduce system vibration. *ASME Journal of Dynamic Systems, Measurement, and Control*, 112:76–82, 1990.

[59] I. M. Díaz, E. Pereira, V. Feliu, and J. J. L Cela. Concurrent design of multimode input shapers and link dynamics for flexible manipulators. *Mechatronics, IEEE/ASME Transactions on*, PP(99):1 –6, 2009.

[60] Lucy Y. Pao. Input shaping design for flexible systems with multiple actuators. In *Proceedings of the 13th World Congress of the International Federation of Automatic Control*, San Francisco, July 1996.

[61] Sungung Lim, Homer Stevens, and Jonathan P. How. Input shaping for multi-input flexible systems. *ASME Journal of Dynamic Systems, Measurement, and Control*, 121:443–447, September 1999.

[62] J. Fiene and G. Niemeyer. Toward switching motor control. *Mechatronics, IEEE/ASME Transactions on*, 11(1):27 – 34, feb. 2006.

[63] Eric J. Barth and Michael Goldfarb. A control design method for switching systems with application to pneumatic servo systems. In *2002 ASME International Mechanical Engineering Congress and Exposition (IMECE)*, page 33424, New Orleans, LA, November 2002. ASME, ASME.

[64] William Singhose, Neil Singer, and Warren Seering. Residual vibration reduction using vector diagrams to generate shaped inputs. *Transactions of the ASME Journal of Mechanical Design*, 116:654–659, June 1994.

[65] K.L. Sorensen, K. Hekman, and W.E. Singhose. Finite-state input shaping. *Control Systems Technology, IEEE Transactions on*, 18(3):664 –672, May 2010.

[66] William E. Singhose, Bart W. Mills, and Warren P. Seering. Closed form methods for generating on-off commands for undamped flexible spacecraft. *Journal of Guidance, Control, and Dynamics*, 22(2):378–382, 1998.

[67] William Singhose, Erica Biediger, Hideto Okada, and Saburo Matunaga. Experimental verification of real-time control for flexible systems with on-off actuators. *ASME Journal of Dynamic Systems, Measurement, and Control*, 128:287–296, June 2006.

[68] Jinjun Shan, Dong Sun, and Dun Liu. Design for robust component synthesis vibration suppression of flexible structures with on-off actuators. *IEEE Transactions on Robotics and Automation*, 20(3):512–525, June 2004.

[69] Gangbing Song, Nick V. Buck, and Brij N. Agrawal. Spacecraft vibration reduction using pulse-width pulse-frequency modulated input shaper. In *AIAA Guidance, Navigation and Control Conference*, Baltimore, MD, 1998. AIAA.

[70] Antonio Bicchi and Giovanni Tonietti. Fast and "soft-arm" tactics. *IEEE Robotics and Automation Magazine*, 11(2):22–33, June 2004.

[71] James M. Wakeling, Benno M. Nigg, and Antra I. Rozitiis. Muscle activity damps the soft tissue resonance that occurs in response to pulsed and continuous vibrations. *Journal of Applied Physiology*, 93:1093–1103, May 2002.

[72] Junjiro Onoda, Takao Endo, Hidehiko Tamaoki, and Naoyuki Watanabe. Vibration suppression by variable-stiffness members. *American Institute of Aeronautics and Astronautics Journal*, 29(6):977–983, June 1991.

[73] L.R. Corr and W. W. Clark. A novel semi-active multi-modal vibration control law for a piezoceramic actuator. *Transactions of the ASME Journal of Vibration and Acoustics*, 125:214–222, 2003.

[74] Hiroshi Fujimoto and Yoichi Hori. Vibration suppression and optimal repetitive disturbance rejection control in semi-nyquist frequency region using multirate sampling control. In *Proceedings of the 39th IEEE Conference on Decision and Control*, pages 3745–3750, Sydney, Australia, December 2000. IEEE.

[75] D.F. Delchamps. Stabilizing a linear system with quantized state feedback. *IEEE Transactions on Automatic Control*, 35(8):916–924, August 1990.

[76] N. Elia and S.K. Mitter. Quantization of linear systems. volume 4, pages 3428 –3433 vol.4, 1999.

[77] D.F. Coutinho, Minyue Fu, and C.E. de Souza. Input and output quantized feedback linear systems. *Automatic Control, IEEE Transactions on*, 55(3):761 –766, mar. 2010.

[78] Minyue Fu and Lihua Xie. The sector bound approach to quantized feedback control. *Automatic Control, IEEE Transactions on*, 50(11):1698 – 1711, nov. 2005.

[79] H. Richter, E.A. Misawa, and B.D. O'Dell. Stability analysis of discrete linear systems with quantized input. volume 4, pages 2991 – 2996 vol.4, 2002.

[80] H. Richter and E.A. Misawa. Stability analysis of discrete linear systems with quantized input and state measurements. volume 3, pages 2392 – 2397 vol.3, 2002.

[81] H. Richter and E.A. Misawa. Stability of discrete-time systems with quantized input and state measurements. *Automatic Control, IEEE Transactions on*, 48(8):1453 – 1458, aug. 2003.

[82] R.W. Brockett and D. Liberzon. Quantized feedback stabilization of linear systems. *IEEE Transactions on Automatic Control*, 45(7):1279 –1289, jul 2000.

[83] Shun-ichi Azuma and Toshiharu Sugie. Optimal dynamic quantizers for discrete-valued input control. *Automatica*, 44(2):396 – 406, 2008.

[84] S.-I. Azuma and T. Sugie. An analytical solution to dynamic quantization problem of nonlinear control systems. In *Decision and Control, 2009 held jointly with the 2009 28th Chinese Control Conference. CDC/CCC 2009. Proceedings of the 48th IEEE Conference on*, pages 3914 –3919, 2009.

[85] Robert C. Juvinall and Kurt M. Marshek. *Fundamentals of Machine Component Design*. John Wiley and Sons, 3 edition, 2000.

[86] Larry Howell. *Compliant Mechanisms*. John Wiley and Sons, New York, 1 edition, 2001.

[87] Nicolae Lobontiu and Jeffrey S. N. Paine. Design of circular cross-section corner-filleted flexure hinges for three-dimensional compliant mechanisms. *ASME Journal of Mechanical Design*, 124:479–484, September 2002.

[88] Huy-Hoang Pham and I-Ming Chen. Stiffness modeling of flexure parallel mechanism. *Precision Engineering*, 29:467–478, 2005.

[89] Guo Ye, Wei Li, Yu qiao Wang, Xue feng Yang, and Ling Yu. Kinematics analysis of bridge-type micro-displacement mechanism based on flexure hinge. In *Proceedings of the 2010 IEEE international conference on information and automation*, pages 66–70, June 2010.

[90] William B. Jones and W.J Thron. *Continued Fractions: Analytic Theory and Applications*, volume 11 of *Encyclopedia of Mathematics and its Applications*. Addison-Wesley, 1980.

[91] Andrew M. Rockett and Peter Szüz. *Continued Fractions:*. World Scientific, 1992.

[92] Elias Zakon. *Mathematical Analysis I*. The Trilla Group, 1975.

[93] D. A. Robinson. The mechanics of human saccadic eye movement. *the Journal of Physiology*, 174:245–264, 1964.

[94] Jun Ueda, Thomas Secord, and Harry Asada. Piezoelectric cellular actuators using nested rhombus multilayer mechanisms. In *1st Annual Dynamic Systems and Control Conference (DSCC 2008)*, Ann Arbor, MI, USA, October 2008.

[95] J. Schultz and J. Ueda. Experimental verification of discrete switching vibration suppression. *Mechatronics, IEEE/ASME Transactions on*, 17(2):298 –308, April 2012.

[96] M.J.D. Powell. *Numerical Methods for Nonlinear Algebraic Equations*, chapter 7, pages 115–161. Gordon and Breach Science Publishers, 1970.

[97] Götz Alefeld and Jürgen Hertzberger. *Introduction to Interval Computations*. Academic Press, New York, 1983.

[98] M. Goldfarb and N Celanovic. A lumped parameter electromechanical model for describing the nonlinear behavior of piezoelectric actuators. *ASME Journal of Dynamic Systems, Measurement, and Control*, 119:478–485, September 1997.

[99] Timothy McPherson and Jun Ueda. Piezoelectric self-sensing technique for tweezer style end-effector. In *Proceedings of the IEEE/RSJ International Conference on Intelligent Robots and Systems*, pages 1940–1945, San Francisco, CA, September 2011.

[100] Ioan Alexandru Ivan, Micky Rakotondrabe, Philippe Lutz, and Nicolas Chaillet. Current integration force and displacement self-sensing method for cantilevered piezoelectric actuators. *AIP Review of Scientific Instruments*, 80, 2009.

[101] Adrien Badel, Jinhao Qiu, and Tetsuaki Nakano. Self-sensing force control of a piezoelectric actuator. *IEEE Transactions on Ultrasonics, Ferroelectrics and Frequency Control*, 55(12):2571–2581, December 2008.

[102] Yuichi Kurita, Fuyuki Sugihara, Jun Ueda, and Tsukasa Ogasawara. Piezoelectric tweezer-type end effector with force-and displacement-sensing capability. *IEEE/ASME Transactions on Mechatronics*, PP:1–10, 2011.

VITA

Joshua Schultz was born in Connecticut and lived on 3 continents before spending his teen years in Eastern Massachusetts. He graduated in 2002 with a Bachelor's degree in Mechanical Engineering, Cum Laude from Tufts University in Medford, Massachusetts. He graduated in 2004 with a Master's degree in Mechanical Engineering from Vanderbilt University in Nashville, Tennessee and earned his doctoral degree in 2012 from the Georgia Insitute of Technology. He was awarded the ARCS scholarship and was President of the Mechanical Engineering Graduate Association (MEGA) in 2011. From 2004 to 2008, he was a member of the motion control and power systems group, product services and solutions division of Lexmark International in Lexington, KY. His interests are in biologically inspired and medical robotics. He will join the Istituto Italiano di Tecnologia as a postdoctoral fellow after graduation.